

©2014

Mahsa Sina

ALL RIGHTS RESERVED

STRUCTURAL CHANGES OF CONVERSION METAL FLUORIDE CATHODES IN  
LITHIUM ION BATTERIES

by

MAHSA SINA

A dissertation submitted to the  
Graduate School-New Brunswick  
Rutgers, The State University of New Jersey

In Partial fulfillment of the requirements

For the degree of

Doctor of Philosophy

Graduate Program in Materials Science and Engineering

Written under the direction of

Professor Frederic Cosandey

And approved by

---

---

---

---

New Brunswick, New Jersey

October, 2014

## **ABSTRACT OF THE DISSERTATION**

Structural changes of Conversion Metal Fluoride Cathodes in Lithium Ion Batteries

by MAHSA SINA

Dissertation Director:

Professor Frederic Cosandey

Currently, cathode materials for Li-ion batteries are based on intercalation processes where, during charge and discharge processes, Li intercalates into the crystal lattice while maintaining the host crystal structure. More recently, new cathode materials have been introduced based on conversion reactions involving phase transformation and complete reduction of the host transition metal. In addition, conversion reactions involve two or more Li ions with a resulting much higher capacity than obtainable for intercalation materials. However, mechanism of phase transformation and cycling reversibility are at present still poorly understood. In this study transmission electron microscopy (TEM) techniques including selected area electron diffraction (SAED) pattern, annular dark field (ADF) STEM image, and electron energy loss spectroscopy (EELS) with nanoscale spatial resolution were used to study the phase evolution and structural changes of iron fluorides ( $\text{FeFe}_2$ ,  $\text{FeO}_{0.7}\text{F}_{1.3}$ ,  $\text{FeF}_3$ ) after various discharge/charge cycles. Additionally, the changes of the Fe valence states upon cycling were determined using EELS by measuring the  $L_3/L_2$  intensity ratio of Fe-L edge.

The structural transformations of  $\text{FeO}_{0.7}\text{F}_{1.3}$  during the first lithiation show that lithiation contains two regions. The first region, lithiation is an intercalation reaction

with reduction of  $\text{Fe}^{3+}$  to  $\text{Fe}^{2+}$ . The second region of lithiation involves a conversion reaction, with the formation of metallic Fe, LiF, and  $\text{Li}_{0.7}\text{Fe}^{2+}_{0.5}\text{O}_{0.7}\text{F}_{0.3}$  (rocksalt type) phases. The first delithiation process follows a different conversion reaction path compared to the first lithiation reaction involving the formation an amorphous rutile-type phase along with with the rocksalt-type phase. Interestingly, upon full recharge (delithiated electrode), the measured average Fe valence state returns back to its initial value of  $\text{Fe}^{2.7+}$ .

The growth of a solid electrolyte interphase (SEI) layer formation at the electrode/electrolyte interface is observed for the iron fluoride compounds ( $\text{FeF}_2$ ,  $\text{FeF}_3$ , and  $\text{FeOF}$ ) after cycling. The evolution of the SEI layer formation after cycling has been studied for the  $\text{FeF}_2$  samples in details by EELS and XPS. We observed the growth of SEI layer with cycle number, which mainly contained LiF and  $\text{Li}_2\text{CO}_3$  compounds. Two degradation mechanisms are identified. First, the increase in the decomposition product layer after cycling inhibits complete reconversion process. Second, dissolution of Fe into the SEI layer after cycling which leads to the loss of active material.

## **Acknowledgements**

To complete a research project like this requires the support and contribution of a lot of people. First, I must thank my advisor, Prof. Frederic Cosandey who initially provided me with the encouragement and support to start on a path of research. He has been approachable and happily discussed and explained about research and concepts. Prof. Cosandey has rigorously reviewed all the work presented in this thesis and taught me to develop my ideas. My accomplishments in this work would not have been possible without his insights and suggestions.

I would like to express my sincerest gratitude to my thesis committee members, Prof. Glenn Amatucci, Prof. Philip Batson, and Prof. Robert Bartynski. Thank you for all your helpful guidance and feedback throughout the process.

I would like to thank Dr. Nathalie Periera for providing cycled samples. Also, I would like to acknowledge Dr. Sylvie Rangan and Ryan Thorpe for their helpful guidance in XPS experiments. In particular, I would like to thank Dr. Rangan for her great advice and suggestions in this work.

Many friends were made along the way, helping me with invaluable inputs and insights. I would like to thank Dr. Maureen Lagos, Dr. Andrew Gmitter, Dr. Ben Groth, Dr. Stuart Deutsch, Jonathan Ko, Anthony Ferrer, Josh Epstein, Dr. Ying Ma, Paul Kim, Dr. Jafar Al-Sharab, Dr. Fabio Nicodemi.

I would like to thank my family. I am enormously grateful to my wonderful parent for their unconditional support and encouragement. I owe a great debt of thanks to them

because of their priceless advice and insights. Also, I would like to extend my thanks to my great husband for his continuously support and love.

I would like to thank an Energy Frontier Research Center funded by the U.S. Department of Energy, Office of Science, Basic Energy Sciences, under Award number DE-SC0001294, for their financial support.

All the work presented in chapter 2 was published as “Structural phase transformation and Fe valence evolution in  $\text{FeO}_x\text{F}_{2-x}/\text{C}$  nanocomposite electrodes during lithiation and de-lithiation processes” M. Sina, K.W. Nam, D. Su, N. Pereira, X.-Q. Yang, G.G. Amatucci, and F. Cosandey. *J. Mater. Chem. A*, 2013, 1, 11629.

## Table of Contents

<b>ABSTRACT OF THE DISSERTATION .....</b>	<b>ii</b>
<b>Acknowledgements .....</b>	<b>iv</b>
<b>Table of Contents .....</b>	<b>vi</b>
<b>List of Figures.....</b>	<b>x</b>
<b>List of Tables .....</b>	<b>xviii</b>
<b>1. Background and Scope of Study.....</b>	<b>1</b>
1.1. Introduction.....	1
1.2. Background.....	3
1.2.1. Rechargeable Li-ion batteries .....	3
1.2.2. Transmission Electron Microscopy (TEM) .....	14
1.3. Thesis objectives .....	24
<b>2. Structural phase transformation and Fe valence evolution in FeO<sub>x</sub>F<sub>2</sub>-</b>	
<b>    x/C nanocomposite electrodes during lithiation and de-lithiation</b>	
<b>    processes .....</b>	<b>26</b>
2.1. Abstract.....	26
2.2. Introduction.....	26
2.3. Experimental procedure: .....	30
2.3.1. Material synthesis and electrode fabrication.....	30
2.3.2. Electrochemistry .....	31
2.3.3. Transmission Electron microscopy.....	31
2.3.4. In-situ X-ray Absorption Spectroscopy (XAS).....	32
2.4. Results.....	33
2.4.1. Initial microstructure.....	33

2.4.2.	Electrochemistry .....	34
2.4.3.	Electron Diffraction and STEM/EELS results.....	37
2.5.	Discussion .....	55
2.6.	Conclusion .....	58
<b>3.</b>	<b>Amorphous phase formation, electron beam induced crystallization</b>	
	<b>and stability upon cycling in delithiated FeOF nanocomposites .....</b>	<b>59</b>
3.1.	Abstract .....	59
3.2.	Introduction.....	59
3.3.	Experimental .....	63
3.3.1.	Materials synthesis.....	63
3.3.2.	Electrochemistry .....	63
3.3.3.	TEM analysis .....	64
3.4.	Results.....	64
3.4.1.	Phase transformation during lithiation and delithiation of FeO <sub>0.7</sub> F <sub>1.3</sub> /C .....	64
3.4.2.	Effect of electron beam irradiation .....	68
3.4.3.	Effect of cycling on phase transformation and stability .....	73
3.5.	Discussion .....	76
3.6.	Conclusion: .....	81
<b>4.</b>	<b>On the role of cycling rate on phase formation in conversion FeF<sub>3</sub>/C</b>	
	<b>cathode materials .....</b>	<b>82</b>
4.1.	Abstract .....	82
4.2.	Introduction.....	83
4.3.	Experimental .....	87



4.3.1.	Nanocomposite synthesis.....	87
4.3.2.	Electrochemistry .....	87
4.3.3.	Transmission electron microscopy .....	88
4.4.	Results.....	89
4.4.1.	Initial FeF <sub>3</sub> microstructure .....	89
4.4.2.	Electrochemistry .....	90
4.4.3.	Electron diffraction and STEM/EELS results.....	92
4.5.	Discussion .....	105
4.6.	Conclusions.....	109
<b>5.</b>	<b>Investigation of the SEI Layer Formation in Conversion Iron Fluoride</b>	
	<b>Cathodes by Combined STEM/EELS and XPS.....</b>	<b>111</b>
5.1.	Abstract .....	111
5.2.	Introduction.....	111
5.3.	Experimental .....	114
5.3.1.	Material synthesis and electrode fabrication.....	114
5.3.2.	Electrochemistry .....	114
5.3.3.	TEM .....	115
5.3.4.	Helium Microscopy .....	115
5.3.5.	X-ray Photoelectron Spectroscopy (XPS) .....	116
5.4.	Results and Discussion .....	117
5.4.1.	Electrochemical performance of the FeF <sub>2</sub> /C cathode material and sampling choice.....	117
5.4.2.	Surface Morphology .....	118
5.4.3.	TEM/STEM characterization.....	118
5.4.4.	XPS characterization.....	128
5.5.	Conclusion .....	135

<b>6.</b>	<b>Future work.....</b>	<b>137</b>
<b>7.</b>	<b>Bibliography .....</b>	<b>139</b>

## List of Figures

Figure 1-1 Schematic showing charge/discharge process in a Li-ion battery cell [17].	4
Figure 1-2 Schematic showing the discharge reaction mechanisms of the intercalation, conversion, and displacement cathodes [5].	6
Figure 1-3 Schematic illustration of the formation of a nanocomposite carbon metal fluoride [5].	7
Figure 1-4(a) Bright-Field TEM image of the initial $\text{FeF}_2$ , and (b) its color elemental map indicating C (blue) and $\text{FeF}_2$ (yellow), (c) BF TEM image of the fully lithiated $\text{FeF}_2$ , and (d) its false color elemental map showing Fe (green) and LiF (red) [6].	8
Figure 1-5 (a) SAED pattern of the fully lithiated $\text{FeF}_2$ , showing the existence of LiF and Fe, and (b) Li-K and Fe-M edges taken from the fully lithiated $\text{FeF}_2$ .	9
Figure 1-6(a) ADF-STEM image of the initial $\text{CuF}_2/\text{C}$ sample, (b) BF- TEM image of fully lithiated $\text{CuF}_2/\text{C}$ , and (c) false color composite image of fully lithiated $\text{CuF}_2/\text{C}$ showing LiF (red) and Cu (green) phases, and (d) HAADF atomic image from a Cu particle [6].	10
Figure 1-7 XRD patterns of lithiated $\text{FeF}_3/\text{C}$ samples [21].	11
Figure 1-8 XRD patterns of delithiated $\text{FeF}_3/\text{C}$ samples [21].	12
Figure 1-9 XRD patterns of $\text{FeOF}/\text{C}$ nanocomposite at various discharged voltages. Cells were cycled at 50 mA/g at 60°C [14].	12
Figure 1-10 Specific capacity of $\text{FeO}_x\text{F}_{2-x}$ nanocomposite with different oxygen content as a function of cycle number. Cells cycled at 50 mA/g between 1.5 and 4.5 V at 60°C [14].	13
Figure 1-11 (a) The collected 2D SAED pattern. (b) The correspondin 1D distribution obtained from it. [24].	15
Figure 1-12 Typical energy loss spectrum of an iron fluoride film: (a) low-loss spectrum, and (b) high-loss spectrum [29].	16
Figure 1-13 All range of ionization edges in the energy-loss spectrum [28].	17

Figure 1-14 (a) Ideal triangular inner edge, (b) The idealized sawtooth sis sitting on the background, (c) The electron loss near edge structure (ELNES), (d) The extended energy loss fine structure (EXELFS), (e) Increasing plural scattering because of thickness provides another edge to post-edge structure [28]. .....	18
Figure 1-15 Correlation between the energy diagram and the density of empty and filled. ....	19
Figure 1-16 Diagram of the empty density of state and ELNES in the fine structure [28]. ....	20
Figure 1-17 Ionization edge energies change in different elements, and white lines reflects the existence of unfilled d-band [28].....	21
Figure 1-18 Li K-edge near-edge fine structure is taken from different lithium compounds, $\text{Li}_2\text{O}$ , $\text{Li}_2\text{CO}_3$ , $\text{LiF}$ , SEI, and lithiated $\text{FeO}_{0.7}\text{F}_{1.3}$ with 1.68 Li. ....	23
Figure 1-19 Second derivative (solid green) of $\text{FeOF/C}$ spectrum. ....	24
Figure 2-1 (a) High resolution TEM image (b) dark Field TEM image and (c) SAED pattern of as synthesized $\text{FeO}_{0.7}\text{F}_{1.3}/\text{C}$ nanocomposite. The diffraction rings are expressed in nm with the corresponding (hkl) rutile reflections.....	34
Figure 2-2 (a) First discharge-charge voltage profile of $\text{FeO}_{0.7}\text{F}_{1.3}/\text{C}$ and $\text{FeO}_{0.5}\text{F}_{1.5}/\text{C}$ nanocomposite used for ex-situ TEM experiment marked by circles. (Cycling rate of 50 mA/g at 60°C) (b) First discharge-charge voltage profile of $\text{FeO}_{0.7}\text{F}_{1.3}/\text{C}$ nanocomposite during in situ XAS experiment. The scan numbers marked on the curves indicate where the in situ XAS spectra were taken for further analysis (Cycling rate of 24 mA/g at 50°C).....	36
Figure 2-3 SAED pattern of $\text{FeO}_{0.7}\text{F}_{1.3}/\text{C}$ after discharge to a) 2.12 V (0.6 Li) and b) 1.5 V (1.68 Li). The diffraction rings are expressed in nm with the corresponding (hkl) reflections for rutile in (a) and superposition of rocksalt (RS) and bcc Fe in (b) .....	37
Figure 2-4 (a) SAED intensity profile of $\text{FeO}_{0.7}\text{F}_{1.3}/\text{C}$ as a function of Li content. For 0.8 Li, the microstructure is highly in-homogeneous and the intensity profiles from three different areas marked A,B,C are depicted in the graph. Also shown in the graph are the positions of the reflections for rutile, rocksalt and Fe phases with (hkl) indices of	

the most intense reflections. The corresponding annular dark field STEM images of $\text{FeO}_{0.7}\text{F}_{1.3}/\text{C}$ lithiated with (b) 0.7 Li, and (c) 0.8 Li. ....	39
Figure 2-5 (a) SAED intensity profile of $\text{FeO}_{0.5}\text{F}_{1.5}/\text{C}$ as a function of Li content. Also shown in the graph are the positions of the reflections for rutile, rocksalt and Fe phases with (hkl) indices of the most intense reflections. The corresponding annular dark field STEM images of $\text{FeO}_{0.5}\text{F}_{1.5}/\text{C}$ lithiated with (b) 0.6 Li, and (c) 0.75 Li. .	41
Figure 2-6 Typical EELS spectra showing (a) F-K edge of standard LiF with characteristic post peak at 700 eV marked by an arrow, and F-K and Fe- $\text{L}_{3,2}$ edges of (b) initial $\text{FeO}_{0.7}\text{F}_{1.3}$ , (c) lithiated with 0.6 Li, (d) lithiated with 1.0 Li (e) lithiated with 1.68 Li (f) lithiated with 2.2 Li. Also shown are the F-K and Fe- $\text{L}_{3,2}$ edges for (g) initial $\text{FeF}_2$ and (h) lithiated $\text{FeF}_2$ .....	42
Figure 2-7 (a) ADF-STEM image of $\text{FeO}_{0.7}\text{F}_{1.3}$ lithiated with 1.68 Li and corresponding concentration maps in at% for (b) O-K, (c) F-K, (d) Fe-L and (e) O-K/F-K atomic ratio with in (f) the Fe valence map expressed as Fe $\text{L}_3/\text{L}_2$ intensity ratio. ....	43
Figure 2-8 SAED patterns of delithiated $\text{FeO}_{0.7}\text{F}_{1.3}/\text{C}$ with a) 1.42 Li and b) 0.18 Li with corresponding patterns c) 1.4 Li and d) 0.18 Li after irradiation with an electron dose of 780 C/cm <sup>2</sup> . The diffraction rings are expressed in nm with the corresponding (hkl) reflections corresponding to the superposition of rocksalt (RS) and bcc Fe in (a) and (c), rocksalt (RS) with amorphous ring in (b) and rutile in (d). Electron beam induced crystallization from rocksalt-amorphous to crystalline rutile is occurring in the de-lithiated electrode. ....	45
Figure 2-9 (a) SAED intensity profiles during delithiation of $\text{FeO}_{0.7}\text{F}_{1.3}/\text{C}$ . Also shown in the graph are the positions of the reflections for rutile, rocksalt and Fe phases with (hkl) indices of the most intense reflections. ....	46
Figure 2-10 Evolution of $I_1/I_2$ diffracted peak intensity ratio as a function of Li content obtained during first recharge cycle for $\text{FeO}_{0.7}\text{F}_{1.3}/\text{C}$ and $\text{FeO}_{0.5}\text{F}_{1.5}/\text{C}$ electrode compositions. ....	47
Figure 2-11 ADF- STEM images of (a) $\text{FeO}_{0.7}\text{F}_{1.3}/\text{C}$ delithiated with 1.02 Li, (b) $\text{FeO}_{0.7}\text{F}_{1.3}/\text{C}$ delithiated with 0.69 Li, (c) $\text{FeO}_{0.5}\text{F}_{1.5}/\text{C}$ delithiated with 0.9 Li, and (d) $\text{FeO}_{0.5}\text{F}_{1.5}/\text{C}$ delithiated with 0.54 Li. ....	48

Figure 2-12 Average Fe valence state calculated from Fe L <sub>3</sub> over L <sub>2</sub> intensity ratio as a function of Li content x for discharge (round symbols) and recharge (square symbols) samples. For 0.8 and higher Li content, the data scatter increases due to the presence of two distinct Fe valence states. In addition to the average Fe valence value, the data also show the valence value for the oxygen rich phase. ....	50
Figure 2-13 In situ Fe-K edge XANES spectra of FeO <sub>0.7</sub> F <sub>1.3</sub> /C nanocomposite during 1 <sup>st</sup> discharge and 1 <sup>st</sup> recharge. Graph (a) and (b) correspond to regions 1 and 2 marked in Figure 2-2(b) during 1 <sup>st</sup> discharge while graph (c) and (d) correspond to regions 3 and 4 marked in Figure 2-2(b) during 1 <sup>st</sup> recharge. ....	53
Figure 2-14 Quantitative fit analysis of the Fe-K edge XANES spectra of FeO <sub>0.7</sub> F <sub>1.3</sub> /C nanocomposite discharge to 1.5V corresponding to lowest discharged state in this study (Curve S75). The best fit is obtained with superposition of metallic Fe <sup>0</sup> , with Fe <sup>2+</sup> O and Fe <sup>2+</sup> F <sub>2</sub> in molar fraction corresponding to 50.4%, 25.6% and 24% .....	54
Figure 3-1 Schematic diagram of free energy differences between amorphous and crystalline states. The electron beam increases the free energy of the amorphous phase to overcome the energy barrier. ....	62
Figure 3-2 SAED pattern of FeO <sub>0.7</sub> F <sub>1.3</sub> /C as a function of Li content with a) initial FeO <sub>0.7</sub> F <sub>1.3</sub> /C, b) FeO <sub>0.7</sub> F <sub>1.3</sub> /C lithiated with 1.6 Li, c) delithiated FeO <sub>0.7</sub> F <sub>1.3</sub> /C with 1.42 Li, b) fully delithiated FeO <sub>0.7</sub> F <sub>1.3</sub> /C with 0.18 Li. ....	66
Figure 3-3 SAED intensity profiles of delithiated FeO <sub>0.7</sub> F <sub>1.3</sub> /C electrode as a function of Li content. The reflections marked I <sub>1</sub> , I <sub>2</sub> and I <sub>3</sub> correspond to the cubic rutile phase with also metallic Fe below 0.69 Li while reflections marked I <sub>R</sub> and I <sub>S</sub> correspond to amorphous type structure .....	67
Figure 3-4 (a,b) SAED patterns of delithiated FeO <sub>0.7</sub> F <sub>1.3</sub> /C electrode after electron irradiation with an electron dose of 780 C/cm <sup>2</sup> with (a) 1.4 Li and (b) fully delithiated (0.18 Li) revealing a transformation to crystalline rutile for the fully delithiated electrode. (c) HRTEM image of recrystallized delithiated sample with (d) corresponding Fourier transform (FFT). ....	69
Figure 3-5 SAED intensity profiles of delithiated FeO <sub>0.7</sub> F <sub>1.3</sub> /C electrode for various Li content after an electron dose 780 C/cm <sup>2</sup> . Electron irradiation induced amorphous to crystalline transition occurs for Li content below 0.69 Li. ....	70

Figure 3-6-S Changes in SAED intensity profiles of $\text{FeO}_{0.7}\text{F}_{1.3}/\text{C}$ recharged with (a) 1.42 Li, b) 0.69 Li, and (c) 0.18 Li as a function of electron beam dose corresponding to (1) $20 \text{ C/cm}^2$ , (2) $270 \text{ C/cm}^2$ , (3) $550 \text{ C/cm}^2$ and (4) $780 \text{ C/cm}^2$ .....	71
Figure 3-7 F-K over Fe-L EELS intensity ratio ( $I_F/I_O$ ) as a function of electron dose for delithiated $\text{FeO}_{0.7}\text{F}_{1.3}/\text{C}$ with 1.08 Li and 0.18 Li. ....	73
Figure 3-8 Discharged capacity as a function of cycle number for $\text{FeO}_{0.7}\text{F}_{1.3}/\text{C}$ cathode cycled at a rate of $50 \text{ mA/g}$ at $60^\circ\text{C}$ . ....	73
Figure 3-9 SAED pattern of delithiated $\text{FeO}_{0.7}\text{F}_{1.3}/\text{C}$ after (b) 3 cycles, and (d) 60 cycles. ....	74
Figure 3-10 SAED intensity profiles of cycled delithiated $\text{FeO}_{0.7}\text{F}_{1.3}/\text{C}$ as a function of number of cycles (a) before and (b) after electron irradiation with an electron dose of $780 \text{ C/cm}^2$ .....	75
Figure 3-11 (a,b) Rocksalt crystal unit cell and (c,d) Rutile crystal structure, showing the octahedral arrangements ( $\text{Fe}(\text{OF})_6$ ) in rocksalt and rutile unit cells .....	79
Figure 3-12 Schematic diagram depicting the diffusionless transformation and relation between FCC and BCT structures. Such a transformation can be occurring between rocksalt to rutile as the Fe sub-lattice from the rocksalt and rutile structures form FCC and BCT lattices respectively. ....	80
Figure 4-1 Initial $\text{FeF}_3/\text{C}$ nanocomposite(a) SAED reveal the presence of R-3m $\text{FeF}_3$ (b) HRTEM image showing the morphology of the crystalline $\text{FeF}_3$ with average particle size of about $15 \text{ nm}$ . ....	89
Figure 4-2 (a) Discharge voltage profile curves for the first cycle of the $\text{FeF}_3/\text{C}$ nanocomposite electrode under $58.8 \text{ mA/g}$ , $23.5 \text{ mA/g}$ , and $8.8 \text{ mA/g}$ , (b) Voltage profiles for the first discharge-charge cycle under different currents of $58.8 \text{ mA/g}$ and $8.8 \text{ mA/g}$ .....	91
Figure 4-3 SAED intensity profiles of the possible phases (Fe, LiF, $\text{FeF}_3$ , and tetragonal $\text{Li}_{1/4}\text{Fe}_{5/4}\text{Fe}_3$ ( $\text{P42/mnm}$ )), lithiated $\text{FeF}_3/\text{C}$ under a constant current of $58.8 \text{ mA/g}$ , from different areas A, area C respectively, and initial $\text{FeF}_3/\text{C}$ .....	94

Figure 4-4 SAED patterns of the lithiated $\text{FeF}_3/\text{C}$ nanocomposite electrode under a constant current of 58.8 mA/g, (a) representing the presence of the $\text{Li}_{1/4}\text{Fe}_{5/4}\text{Fe}_3$ (P42/mnm) phase, and (b) superposition LiF and Fe phases. ....	94
Figure 4-5 Lithiated $\text{FeF}_3/\text{C}$ nanocomposite electrode under a constant current of 58.8 mA/g (a) ADF-STEM corresponding to area A of the sample, and (b) ADF-STEM corresponding to area B. ....	95
Figure 4-6 STEM-EELS spectra of the lithiated $\text{FeF}_3/\text{C}$ nanocomposite electrode under a constant current of 58.8 mA/g, (a) Fe-M and Li-K edges (b) Fe- $\text{L}_{2,3}$ and F-K edges. ....	96
Figure 4-7 SAED intensity profiles of the possible phases (Fe, LiF, $\text{FeF}_3$ , and tetragonal $\text{Li}_{1/4}\text{Fe}_{5/4}\text{Fe}_3$ (P42/mnm)), and the lithiated $\text{FeF}_3/\text{C}$ nanocomposite electrode under a constant current of 23.5 mA/g from different areas A, B. ....	97
Figure 4-8 SAED intensity profile of the lithiated $\text{FeF}_3/\text{C}$ nanocomposite electrode under a constant current of 8.8 mA/g. ....	98
Figure 4-9 Lithiated $\text{FeF}_3/\text{C}$ nanocomposite electrode lithiated under a constant current of 8.8mA/g, (a) ADF-STEM image, (b) HRTEM image. ....	99
Figure 4-10 STEM-EELS spectra of the lithiated $\text{FeF}_3/\text{C}$ nanocomposite electrode under ....	99
Figure 4-11 SAED intensity profiles of the possible phases ( $\text{FeF}_3$ , and tetragonal (P4 <sub>2</sub> /mnm) $\text{Li}_{1/4}\text{Fe}_{5/4}\text{Fe}_3$ ), and delithiated $\text{FeF}_3/\text{C}$ at 4.5 V nanocomposite electrode cycled at 58.8 mA/g. ....	100
Figure 4-12 SAED intensity patterns of the possible phases ( $\text{FeF}_2$ , and tetragonal (P42/mnm) $\text{Li}_{1/4}\text{Fe}_{5/4}\text{Fe}_3$ ), and delithiated $\text{FeF}_3/\text{C}$ nanocomposite electrode under a constant current of 8.8 mA/g, from different areas A, B, and C. ....	101
Figure 4-13 STEM-EELS spectra of the delithiated $\text{FeF}_3/\text{C}$ nanocomposite under constant current of 8.8 mA/g (a) Fe-M and Li-K edges (b) Fe- $\text{L}_{2,3}$ and F-K edges. ....	102
Figure 4-14 Discharge capacity vs. cycle number of the $\text{FeF}_3/\text{C}$ nanocomposite cycle at 8.8 mAh/g. ....	103



Figure 4-15 SAED intensity profiles of the lithiated $\text{FeF}_3/\text{C}$ nanocomposite electrode under a constant current of 8.8 mA/g after different cycle number and the possible phases ( $\text{FeF}_3$ , $\text{LiF}$ , $\text{Fe}$ , and tetragonal ( $\text{P4}_2/\text{mnm}$ ) $\text{Li}_{1/4}\text{Fe}_{5/4}\text{Fe}_3$ ).....	104
Figure 4-16 SAED intensity profiles of the delithiated $\text{FeF}_3/\text{C}$ nanocomposite electrode under a constant current of 8.8 mA/g after different cycle number and the possible phases ( $\text{FeF}_3$ , $\text{LiF}$ , $\text{Fe}$ , and tetragonal ( $\text{P4}_2/\text{mnm}$ ) $\text{Li}_{1/4}\text{Fe}_{5/4}\text{Fe}_3$ ).....	105
Figure 4-17 Simulated SAED intensity profiles for possible trirutile phases.....	109
Figure 5-1 Discharge capacity vs. cycle number of the $\text{FeF}_2/\text{C}$ nanocomposite electrode cycled at 50 mA/g, at 60°C. ....	117
Figure 5-2 Helium ion microscope image of the lithiated $\text{FeF}_2/\text{C}$ material after 1 (a), and after 20 cycles (b,c).....	118
Figure 5-3 SAED pattern and ADF images of the delithiated sample (a,b) after 1 cycle, (c,d) after 20 cycles. ....	119
Figure 5-4 SAED pattern and ADF images of the delithiated sample (a,b) after 1 cycle, (c,d) after 20 cycles. ....	121
Figure 5-5 Schematic illustration showing the evolution of the fully charged $\text{FeF}_2$ samples after (a) 1 cycle, (b) 10 cycles, (d) 20 cycles as seen using TEM. The surface SEI (blue) is represented surrounding each $\text{FeF}_2$ particles.....	122
Figure 5-6 EELS spectra of the delithiated sample after various cycle number (a) Li K- and Fe M-edges, (b) O K-, F K-, and Fe L2,3 edges. ....	123
Figure 5-7 (a) ADF-STEM image of the lithiated $\text{FeF}_2$ after 20 cycles, (b) the corresponding spliced EELS spectrum. ....	124
Figure 5-8 The comparison of the lithiated $\text{FeF}_2$ after 20 cycles SEI layer to the reference compounds ( $\text{LiF}$ , $\text{Li}_2\text{CO}_3$ , and PVDF) (a) Li K-edge, (b) C K-edge, (c) O K-edge, (d) F K-edge. ....	126
Figure 5-9 Subtracted EELS spectrum of SEI layer from $\text{LiF}$ (SEI is from the same area in Figure 5-5). The subtracted spectrum shows the presence of Fe L2,3 edges. ....	127

Figure 5-10 XPS spectra of a delithiated $\text{FeF}_2$ electrode after 1 cycle at different sputter depths. The Fe 2p peak is fit very well by a single $\text{FeF}_2$ component, indicating that the active cathode material has fully reconverted during delithiation. SEI composition is discussed in the text. ....	129
Figure 5-11 XPS sputter depth profile of a delithiated $\text{FeF}_2$ electrode after 10 cycles. The lineshape of the Fe 2p peak is indicative of $\text{FeF}_2$ , $\text{Fe}^0$ , and a third component (possibly $\text{Li}_{1-x}\text{Fe}_x\text{F}$ ). The composition of the SEI is consistent with that of the 1 cycle sample, although this SEI is substantially thicker. ....	132
Figure 5-12 XPS sputter depth profile of a lithiated $\text{FeF}_2$ electrode after 10 cycles. ....	134

## **List of Tables**

Table 4-1 Structural phase evolution after discharge and charge for cycled $\text{FeF}_3/\text{C}$ obtained from different investigators .....	85
Table 5-1 Summary of XPS results for lithiated and delithiated samples: the SEI thickness as estimated by the amount of sputtering necessary to reach a stable Fe 2p intensity and percentage of the total F 1s signal attributed to LiF.....	135

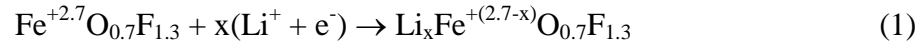
## 1. Background and Scope of Study

### 1.1. Introduction

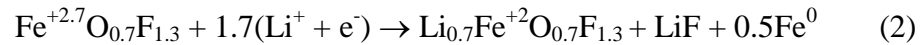
One of the most important energy storage technologies is lithium ion battery. Lithium ion batteries are widely used for various portable electronic and automotive applications. Despite decades of effort and research, the performance of the battery cells is limited by the amount of lithium, which can be stored in positive and negative electrodes. Currently, the positive electrode is used in lithium ion batteries has layered structures, which maintain their crystal structure during cycling such as  $\text{LiCoO}_2$ .  $\text{LiCoO}_2$  has a high cycle life and potential, but low specific capacity of about 150 mAh/g. In this material only 0.55  $\text{Li}^+$  per Co metal can transfer due to the limited possible oxidation states [1-4]. As opposed to intercalation materials, reversible conversion materials demonstrate significant changes in their crystal structures. Also, more than one electron transfer can occur per transition metal, thus providing high specific capacities. Specifically, highly ionic metal fluorides and halides have high output voltages as cathodes in the conversion reactions. Recently conversion metal fluorides, such as  $\text{FeF}_2$  [5, 6],  $\text{FeF}_3$  [7-10],  $\text{BiF}_3$  [11, 12], and  $\text{CuF}_2$  [8, 10] have been extensively investigated due to their high energy density, low cost and low toxicity. However, they associated with low electronic conductivity; therefore, metal fluoride carbon nanocomposites can be fabricated to enhance the electrochemical properties.

Iron oxyfluoride has a higher theoretical capacity (800mAh/g) and cycling stability as compared to  $\text{FeF}_2$ . The formations of covalent Fe-O bonds in iron oxyfluoride improve its electronic conductivity. The first region of lithiation occurs between 3.5 to

2.1 V,  $\text{Li}^+$  is inserted into the FeOF to form  $\text{Li}_x\text{Fe}_x^{2+}\text{Fe}_{1-x}^{3+}\text{OF}$  via a single phase (equ. 1), which corresponds to iron valence reduction from  $\text{Fe}^{3+}$  to  $\text{Fe}^{2+}$  [13, 14].



In the second region between  $x = 0.7$ - $1.7$  Li (2.1- 1.5V), the intermediate phase converts into rocksalt-type phase LiF, and metallic iron (equ. 2).



The charge process involves the formation of rocksalt-type and amorphous-rutile phases. This amorphous phase has found to recrystallize to rutile-type phase under the low electron irradiation. The fluorine compounds are very sensitive to the electron beam, and it can lead to degradation of materials; it is necessary to study and characteristics of these damages and controls them. Understanding the microscopic mechanisms of structural transformations of FeOF after various cycle number is critical to control and optimize the conversion behavior such as voltage hysteresis and cycle life. The structural changes of FeOF occur upon discharge and recharge, however, are not well understood and needs to be studied more to determine the causes of capacity failure

Conversion materials undergo considerable structural changes during the lithiation-delithiation process, involving both alteration of the crystal structures and coexistence of separate nanophases. Thus the surface of the electrode is constantly modified and thus in principle offers fresh reactive sites leading to increase the electrode and electrolyte interaction as well as metal dissolution into the SEI layer. Gmitter and coworkers [12, 15] studied the failure mechanism of the conversion  $\text{BiF}_3$  positive electrode. They reported that the Fe nanodomains can catalyze the formation of a SEI

layer after cycling, and the SEI growth exacerbated the capacity loss. In this work transmission electron microscopy (TEM) and scanning transmission electron microscopy techniques are used to provide valuable information on nanostructures and distribution of the converted phases after cycling.

## **1.2. Background**

### **1.2.1. Rechargeable Li-ion batteries**

Batteries convert chemical energy into electrical energy via reduction-oxidation reactions. The primary electrochemical unit, which provides this electrical energy, is a cell. An electrochemical cell consists of one cathode, an anode, and an electrolyte (Figure 1-1). The anode or negative electrode is a place where oxidation occurs and gives out electrons during discharge, whereas the cathode or positive electrode is a place where the reduction reaction occurs and accepts electrons. The electrolyte connects these electrodes ionically, but not electronically. The chemical potential differences between the two electrodes cause electrons to flow through an external circuit and balancing charge neutrality. Electrolyte can be either a solid or a liquid. In liquid form a porous paper (separator) is used to isolate the electrodes electronically and mechanically [3, 16, 17].

Batteries can be classified as primary and secondary in terms of their rechargeability. Primary cells are only discharged once. These batteries are typically easy to use and have good shelf life; however, they can be discarded after one use. Secondary cells can be recharged by applying an external current in the opposite direction that of the discharge.

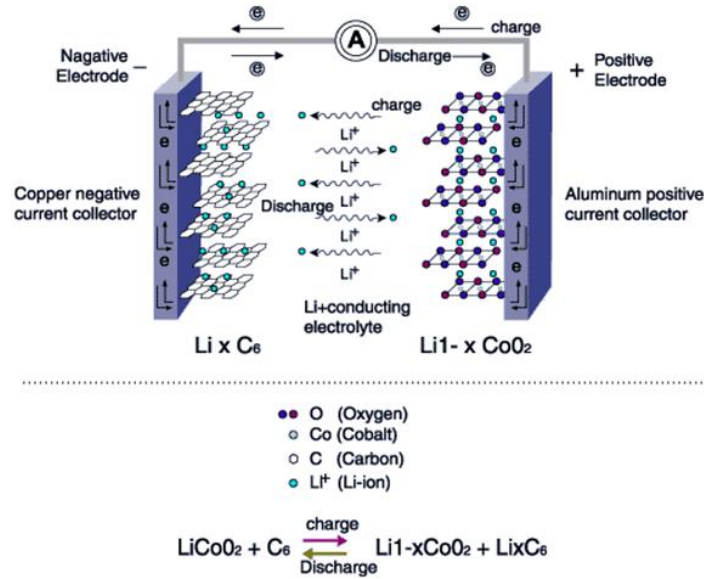


Figure 1-1 Schematic showing charge/discharge process in a Li-ion battery cell [17].

The cell potential (V) and capacity ( $\text{A h kg}^{-1}$ ) are the most important intrinsic parameters, which determine the amount of electrical energy ( $\text{W h kg}^{-1}$  or  $\text{W h l}^{-1}$ ) that can be provided by a battery.

Li-ion batteries received much attention as the highest gravimetric and volumetric energy density. Also, a variety of cathode and anode compounds were implemented for Li-ion batteries. In order to obtain a cell with high energy density, high voltage cathode and low voltage anode need to be paired because the cell potential being the difference of the two [3, 16, 17].

#### 1.2.1.1. Anodes for Li-ion batteries

Lithium metal, carbon, and lithium alloys have been used as the anode materials for Li-ion batteries. Carbon is typically used as the anode material, because it maintains its dimension and structure during discharging and charging, and it provides high

capacity (372 Ah/kg). Although lithium metal can obtain higher capacity (3862 Ah/Kg), it forms lithium dendrites at the interphase of anode and electrolyte [17].

### **1.2.1.2. Cathodes for Li-ion batteries**

A good cathode material needs to have some requirements: 1- The material should be able to insert and extract a large amount of lithium to maximize its specific capacity, 2- The material should be electronically and ionically conductive. 3- The material should be structurally stable to be able to go under structural changes upon reversible lithiation and delithiation. 4- The material should be safe, environmentally friendly, and low cost. 5- The cathode materials can be classified into three types: (a) intercalation, (b) conversion, and (c) displacement cathodes.

#### *(a) Intercalation cathode materials*

There are three crystallographic classes for layered materials: layered trigonal structure, spinel-type, and channeled olivine-type structure. The layered trigonal intercalation cathode materials are represented by the formula  $\text{LiMO}_2$  like  $\text{LiCoO}_2$ , where M is a transition metal. In intercalation materials  $\text{Li}^+$  intercalates and deintercalates between the layers during discharging and charging along with reducing the oxidation state of the transition metal during intercalation (Figure 1-2). The possible oxidation valence states of the transition metal is restricted because of the limited available lithium vacancies for lithium intercalation, which corresponds to low specific capacity. These materials do not show significant structural changes during intercalation/ deintercalation and have a good cycle life.  $\text{LiCoO}_2$  is mostly used as a positive electrode in Li-ion batteries, which stores 0.55  $\text{Li}^+$  per Co and has a reversible specific capacity of 150mAh/g [4, 17, 18].



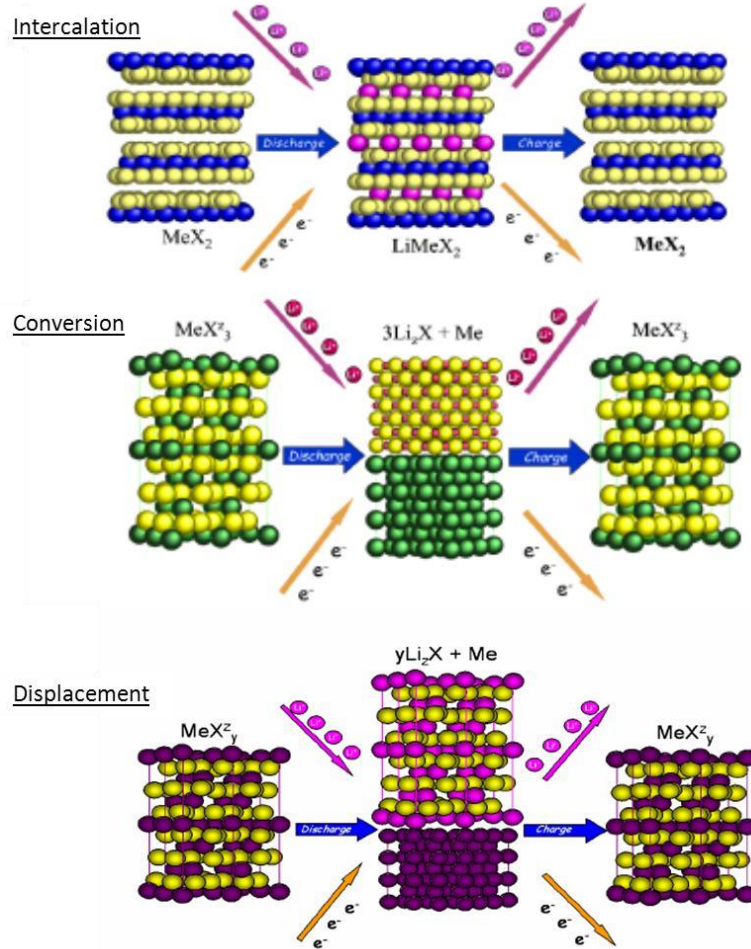


Figure 1-2 Schematic showing the discharge reaction mechanisms of the intercalation, conversion, and displacement cathodes [5].

(b) Conversion cathode materials

In contrast to intercalation materials, conversion materials change their crystal structures into new phases upon Li insertion. These materials have high specific capacities, which are associated with utilizing all the possible oxidation states of the metal. The conversion reaction can be written as follows (equ. 3):



In this reaction metal compound include metal nitrides, fluorides, and oxide convert and reduce upon fully lithiation [4, 5, 17].

Fluorine-base positive electrodes: Metal fluorides are the potential positive electrodes for lithium ion batteries that lithiate/delithiate through conversion reactions. These materials have high voltages and high specific capacities due to their highly ionic bonding, while they have high band gaps resulting to low electronic conductivities. It was shown that fabricating carbon metal fluoride nanocomposites enhances electrochemical properties of metal fluoride (Figure 1-3), in which metal iron particle size reduced in the conductive carbon [5].

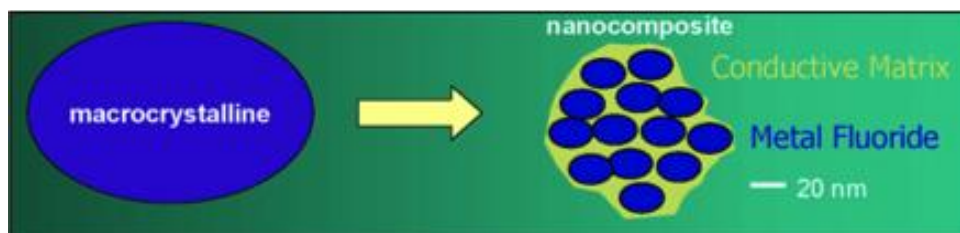
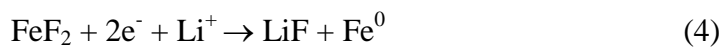


Figure 1-3 Schematic illustration of the formation of a nanocomposite carbon metal fluoride [5].

It has been shown that for  $\text{FeF}_2$  [6] the lithiation process is a fully reversible conversion reaction with specific capacity of about 600 mAh/g, which is attributed to the formation of bicontinuous network metallic iron among lithium fluoride phase. Iron fluoride ( $\text{FeF}_2$ ) has a theoretical capacity of 571 mAh/g. The electrochemical activity of  $\text{FeF}_2$  shows the following a three phase conversion reaction without having Li intercalation in the system (equ. 4).



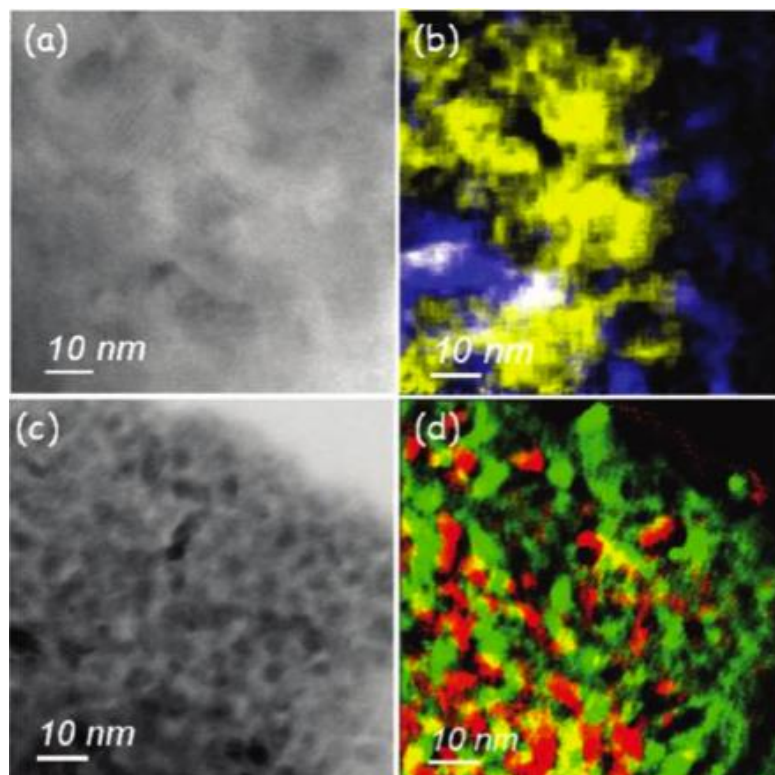


Figure 1-4(a) Bright-Field TEM image of the initial  $\text{FeF}_2$ , and (b) its color elemental map indicating C (blue) and  $\text{FeF}_2$  (yellow), (c) BF TEM image of the fully lithiated  $\text{FeF}_2$ , and (d) its false color elemental map showing Fe (green) and LiF (red) [6].

Bright field TEM (BF) image (Figure 1-4(a)) shows nanoparticles with about 10 nm, and also from the EELS elemental map represents agglomerated  $\text{FeF}_2$  (yellow region) surrounded by the carbon (blue) matrix (Figure 1-4(b)). Upon fully lithiation the BF-TEM image shows a reduction in the particle sizes to about 3-5 nm (Figure 1-4(c)), LiF cannot be detected from the BF image, selected area electron diffraction (SAED) pattern and electron energy loss spectroscopy (EELS) spectrum were utilized to confirm the existence of LiF. The LiF and Fe reflections observed in the SAED pattern (Figure 1-5 (a)). In addition, Fe-M and Li-K in the spectrum (Figure 1-5 (b)) showed the presence

of LiF and Fe. (Figure 1-4(d)) false-colored composite image represents LiF (red) and Fe (green) phases, in which Fe particles are connected. The formation of this bi-continuous Fe network leads to high conductivity and is responsible for the reversibility of the system [5-7].

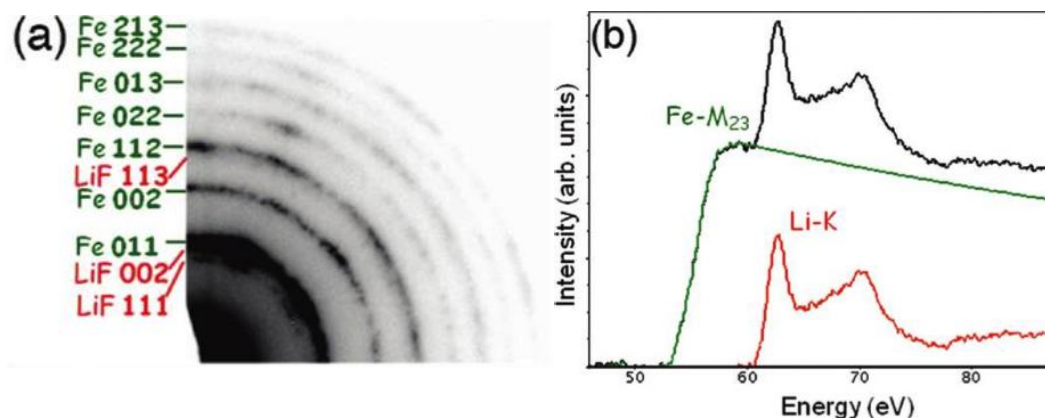


Figure 1-5 (a) SAED pattern of the fully lithiated  $\text{FeF}_2$ , showing the existence of LiF and Fe, and (b) Li-K and Fe-M edges taken from the fully lithiated  $\text{FeF}_2$ .

Unlike  $\text{FeF}_2$ ,  $\text{CuF}_2$  undergoes irreversible conversion reaction upon discharge into LiF and individual Cu particles. Copper fluoride ( $\text{CuF}_2$ ) is a promising cathode material because it provides a specific capacity of 528 mAh/g and the highest theoretical potential of 3.55 V. The irreversible conversion reaction of  $\text{CuF}_2/\text{C}$  is involving the direct formation of Cu and LiF.

HAADF STEM image (Figure 1-6(a)) nanocomposite  $\text{CuF}_2/\text{C}$  shows the agglomerated  $\text{CuF}_2$  (bright) nanoparticles embedded in a carbon matrix (dark). Figure 1-6(b) shows BF-TEM image of the fully lithiated  $\text{CuF}_2/\text{C}$ , which displays spherical Cu particle with average particle size of 5-12 nm. From EELS/STEM map (Figure 1-6(c)) the agglomerated Cu (green) particles and LiF (red), [7, 19-21]. Figure 1-6(d) shows the

presence of stacking faults in the converted Cu nanoparticles. Previous studies on  $\text{FeF}_3/\text{C}$  [21] have shown that  $\text{FeF}_3/\text{C}$  has a reversible high capacity about 600 mAh/g. The lithiation process has two regions. From 0 Li to 0.5 Li, Li inserted into the rhombohedral  $\text{FeF}_3$  leads to  $\text{Li}_{0.5}\text{FeF}_3$  (tri-rutile) formation through a two phase reaction, on further lithiation (0.5 Li to 1 Li), which is a single phase reaction  $\text{LiFeF}_3$  with rutile-like structure is formed, along with reducing more  $\text{Fe}^{3+}$  to  $\text{Fe}^{2+}$ . In the second region (1 Li to 3 Li), Li insertion occurs via a conversion reaction, which is associated with the formation of metallic iron and LiF (Figure 1-7).

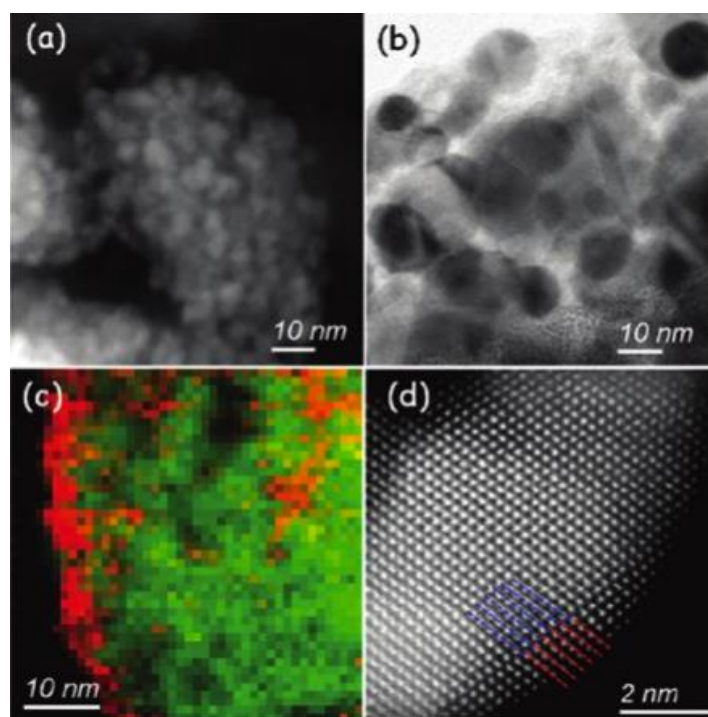


Figure 1-6(a) ADF-STEM image of the initial  $\text{CuF}_2/\text{C}$  sample, (b) BF-TEM image of fully lithiated  $\text{CuF}_2/\text{C}$ , and (c) false color composite image of fully lithiated  $\text{CuF}_2/\text{C}$  showing LiF (red) and Cu (green) phases, and (d) HAADF atomic image from a Cu particle [6].

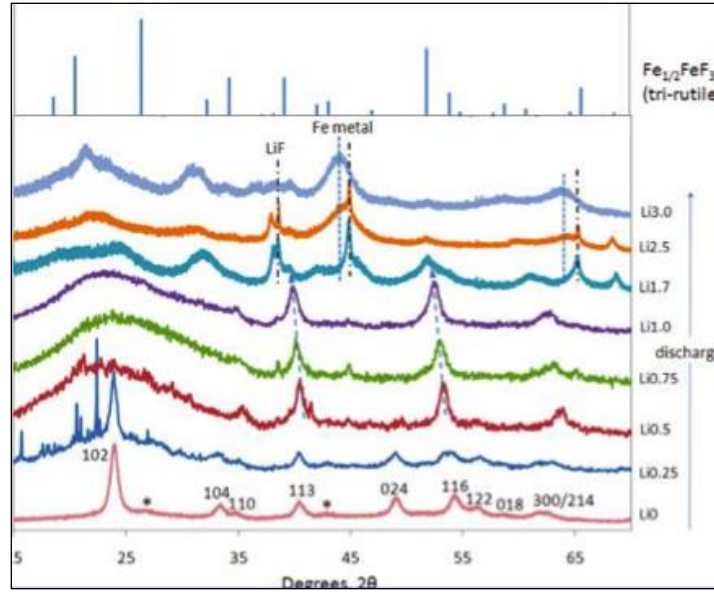
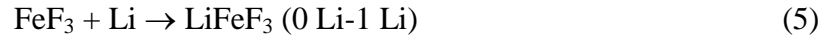


Figure 1-7 XRD patterns of lithiated  $\text{FeF}_3/\text{C}$  samples [21].



The charge process is accompanied by formation of rutile-type phase through a reconversion reaction followed by deintercalation process and reoxidation of Fe (Figure 1-8).



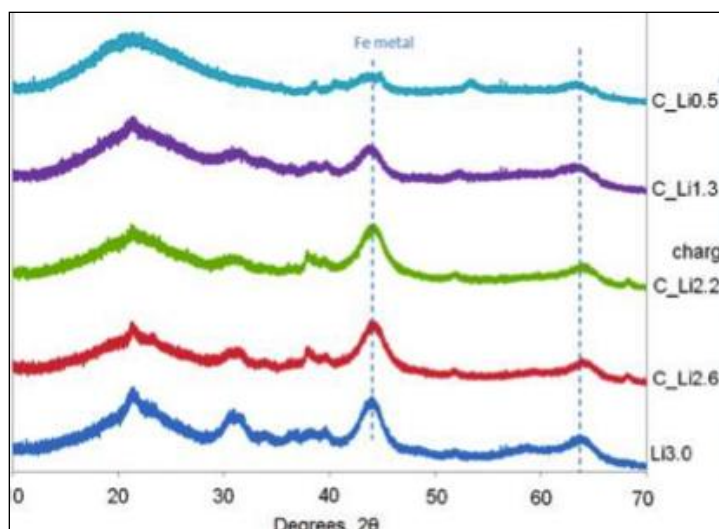


Figure 1-8 XRD patterns of delithiated  $\text{FeF}_3/\text{C}$  samples [21].

Iron oxyfluoride carbon nanocomposite provides a high theoretical capacity of about 500-800 mA/g. On the basis XRD results, the lithiation includes two regions as shown in Figure 1-9[13, 14].

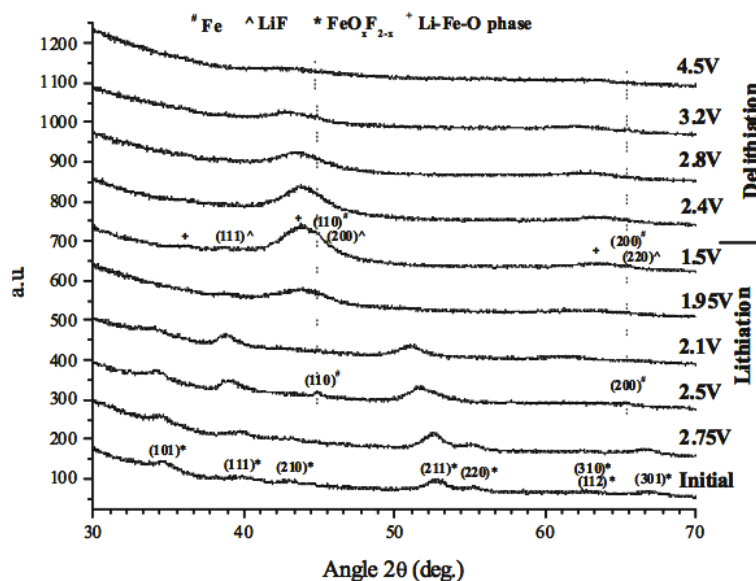
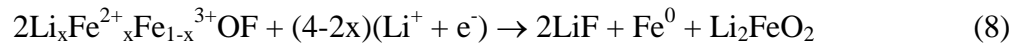


Figure 1-9 XRD patterns of  $\text{FeOF}/\text{C}$  nanocomposite at various discharged voltages. Cells were cycled at 50 mA/g at 60°C [14].

At the early stage, lithium is inserted into the FeOF ( $\text{Li}_x\text{Fe}^{2+}\text{Fe}_{1-x}^{3+}\text{OF}$ ) associated with the reduction of  $\text{Fe}^{3+}$  to  $\text{Fe}^{2+}$  (equ. 7)



Further lithiation down to 1.5V involves the formation of converted phases



It has been shown that FeOF has higher cycling performance compared to  $\text{FeF}_2$  nanocomposite. The introduction of oxygen into the  $\text{FeF}_2$  leads to the improvement in the cycling stability even for the low content of oxygen (Figure 1-10).

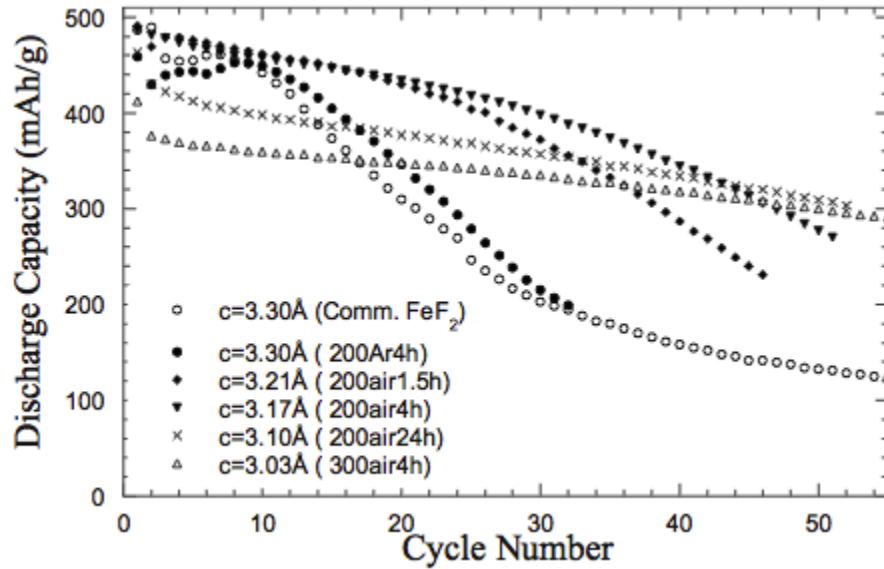


Figure 1-10 Specific capacity of  $\text{FeO}_x\text{F}_{2-x}$  nanocomposite with different oxygen content as a function of cycle number. Cells cycled at 50 mA/g between 1.5 and 4.5 V at 60°C [14].



(c) Displacement cathode materials

Displacement materials do not need to have a layered structure for lithiation as opposed to the intercalation materials. In these materials all the valence states of the cation are utilized and replaced upon  $\text{Li}^+$  insertion, without changing their crystal structure. The cation is replaced.

## 1.2.2. Transmission Electron Microscopy (TEM)

### 1.2.2.1. Electron Diffraction

Electron diffraction is a powerful technique to characterize the structure of materials. Electron diffraction ring patterns are utilized for completely random polycrystalline specimens. The ring patterns form as a result of intersecting of spheres (formed by rotating the reciprocal lattice around the all axes) with the Ewald sphere. It is evident that the spotty diffraction pattern with less uniform rings corresponding to the specimen with larger particle size. The intensity of the rings is not uniform along a ring. Therefore in order not to lose information the ring pattern (Figure 1-11(a)) is circularly averaged intensity for acquiring 1D distribution (Figure 1-11(b)) (XRD-like), in which the intensity plotted as a function of the length of the scattering vector. The 1D function indicated peaks versus the circle radius (bright rings in the DP). The high-energy scattered electrons in SAED have small scattering angle ( $<5^\circ$ ), and the length of the scattering vector is roughly proportional to the scattering angle with a little correction. The small elliptical distortion as a result of the magnetic lenses needs to be corrected during circular averaging. The diffraction pattern of amorphous materials contains broad and diffuse rings [22-24].

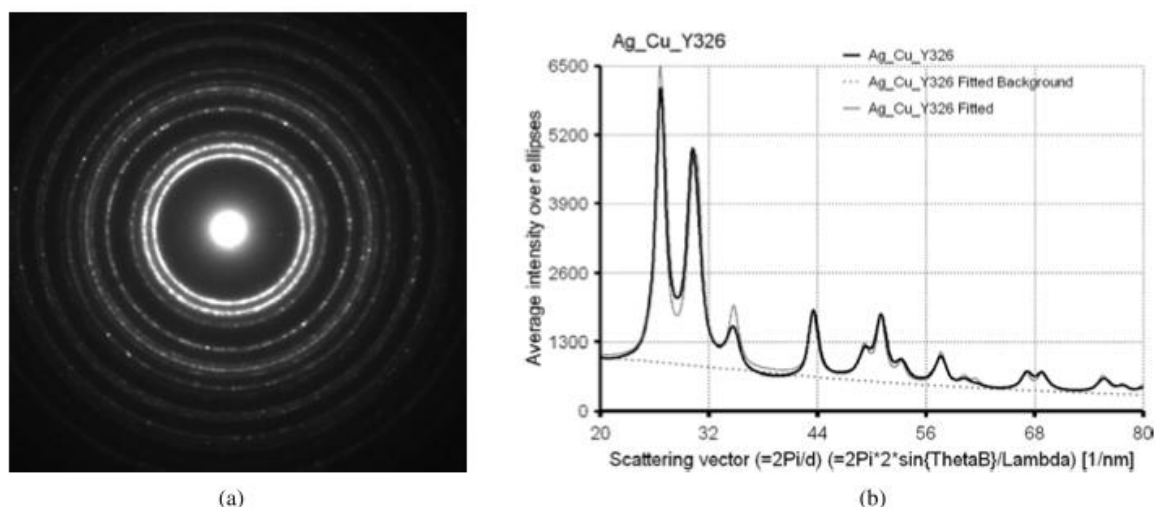


Figure 1-11 (a) The collected 2D SAED pattern. (b) The correspondin 1D distribution obtained from it. [24].

### 1.2.2.2. Electron energy loss spectroscopy (EELS)

The importance of the Electron Energy Loss Spectroscopy (EELS) has been known since 1978, and significant developments have occurred in the scheme of energy loss spectrometers for electron microscopy usages. When high-energy electrons interact with a thin specimen, a transmitted beam travels inside the sample and gives information about the internal structure. Upon traversing a spectrometer, where the electrons dispersed in terms of their kinetic energy, EELS shows the distribution of the scattered electrons into a spectrum. A typical spectrum is shown in Figure 1-12 that contains two regions: 1- Low loss and 2- high loss. The first peak, zero-loss or elastic peak is very intense and shows transmitted electrons without losing energy. The width of the zero-loss peak corresponds to the energy resolution (0.2-2 eV). Low loss features give information from inelastic scattering by valence and conduction-band electrons, whereas High-loss

reflects ionization edges from the core shell (which their electron density decrease in compare with low-loss region) [25-28].

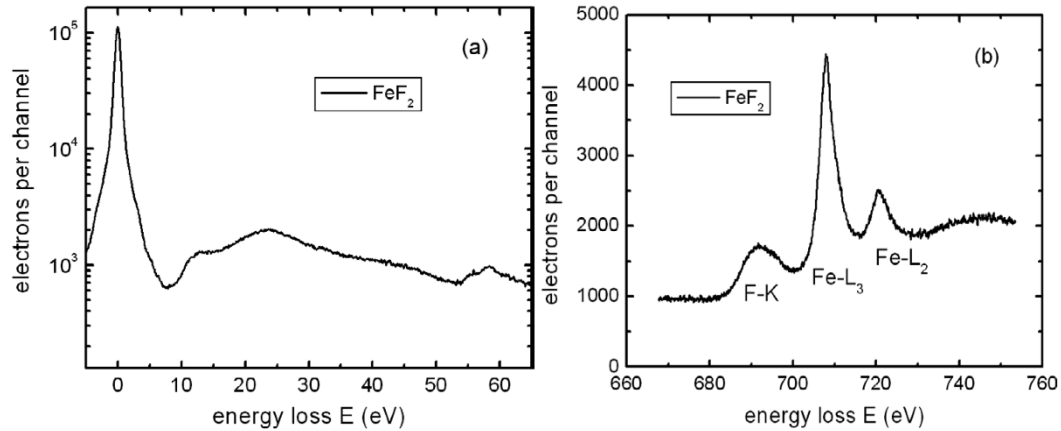


Figure 1-12 Typical energy loss spectrum of an iron fluoride film: (a) low-loss spectrum, and (b) high-loss spectrum [29].

#### (a) Core Loss Spectra

The high energy-loss spectrum ( $>50\text{eV}$ ) provides information (bonding and atomic position) about the inelastic interactions of the electrons from core electron shells. Ionization of elements requires sufficient energy to make a hole in the electron shell of elements, which is much stronger, for the higher atomic number of elements. Different edges can be detected from the ionization energy. Figure 1-13 shows all the different possible edges schematically.

The plasma excitation cross section is much higher than the ionization cross section, so the core-edge intensity is less than Plasmon in a spectrum. The minimum energy, which is required to overcome the binding energy, is called critical energy ( $E_c$ ).

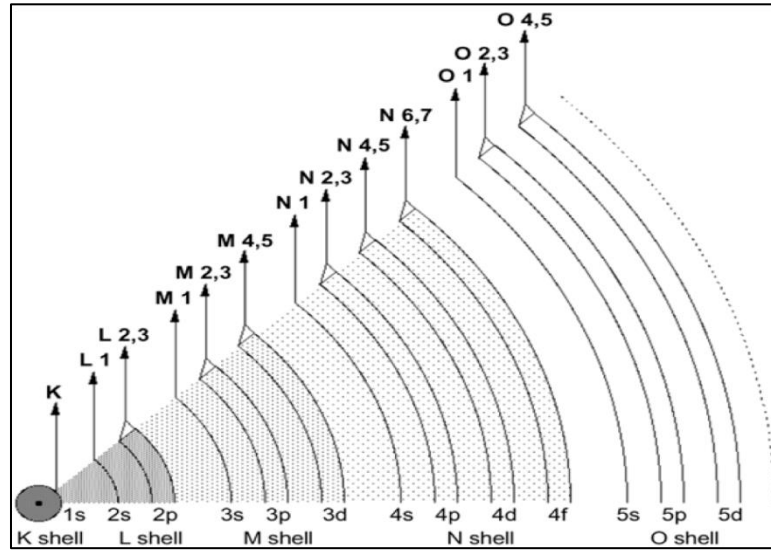


Figure 1-13 All range of ionization edges in the energy-loss spectrum [28].

The ionization decreases as the energy increased above  $E_c$ . This is due to the decreasing the ionization cross section with increasing the energy transfer. This follows by dropping intensity above  $E_c$ , which makes it like triangle shape (Figure 1-14(a)), which is called hydrogenic. In fact, elements that are bound and share electrons with other atoms have different edge shape in the spectrum. Additionally, the effect of plural inelastic scattering is another effect, which change the shape of the edges (Figure 1-14(b)). The ionization near edge fine structure indicates oscillations ( $\sim 50\text{eV}$ ) because of the bonding effect (Figure 1-14(c)), which is called energy-loss near-edge structure (ELNES). Also a little further from the edge ( $>50\text{eV}$ ) may you can find the small oscillations, which is the diffraction effects of the surrounded neighbor atoms around the ionized atom (Figure 1-14(d)) and calls extended energy-loss fine structure (EXFLFS). Lastly, the ionization-loss electrons can possibly have low-loss interaction and affect the edge fine structure with having extra plural scattering intensit and produce plasmons

around 15-25eV after the edge (Figure 1-13(E)). Therefore, ionization edges give a lot of information about the chemical bonding [25-28].

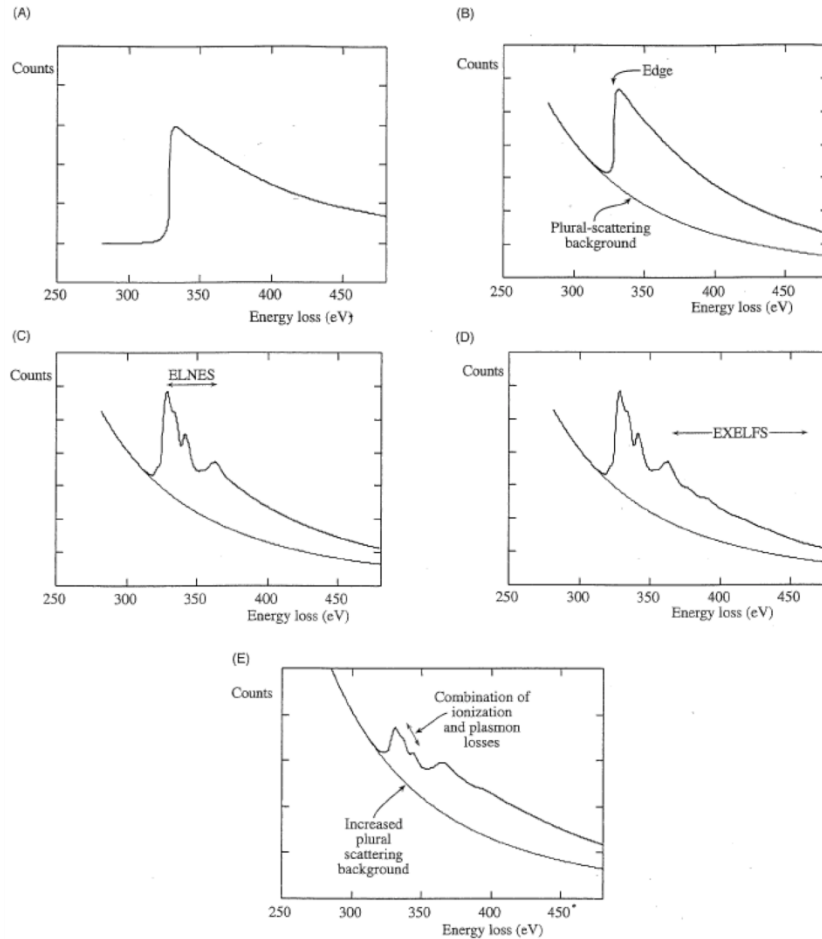


Figure 1-14 (a) Ideal triangular inner edge, (b) The idealized sawtooth sitting on the background, (c) The electron loss near edge structure (ELNES), (d) The extended energy loss fine structure (EXELFS), (e) Increasing plural scattering because of thickness provides another edge to post-edge structure [28].

In order to acquire high-loss spectrum, several requirements should be considered:

1. Beam energy ( $E_0$ ): Using higher beam energy decreases scattering cross section.

2. Beam size and current: The beam size controls the spatial resolution in STEM mode, and the beam current constrains the intensity of signals.
3. Specimen thickness: The specimen thickness should be thin enough to limit the plural scattering otherwise spectrum requires deconvolution.
4. Energy resolution: The energy resolution ( $\Delta E$ ) needs to be low in order to be able to identify the edge and its fine structure. The energy resolution is mostly controlled by electron source except if it has a monochromator.
5. Energy range: The energy range of spectrum is up to 2keV more than this range gives rise to reduce the intensity [25-28].

(b) Fine Structure and Finer details

Oscillations intensities above the ionization edge is called energy-loss near-edge structure (ELNES) and extended energy-loss fine structure (EXELFS). These structures provide information about bonding, neighbor's atoms, and its density of states.

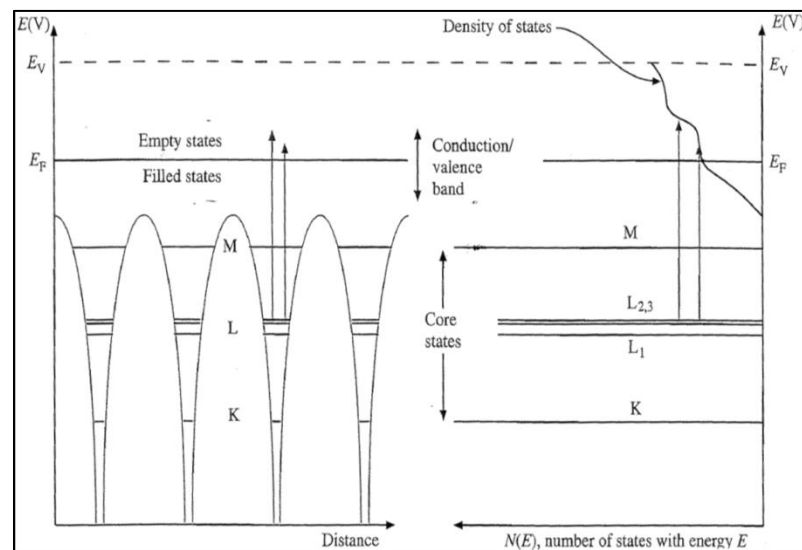


Figure 1-15 Correlation between the energy diagram and the density of empty and filled.

Upon ionization of the atom, the ejected electron may excited to the vacuum level or the other unfilled energy levels of the atom above the Fermi level, which depends on the level probabilities to be filled. Thus, this unequal possibility of filling the unoccupied states is called the density of states (DOS). Figure 1-15 shows this DOS of a metal atom. The ELNES intensity becomes greater for the energy losses associated with the unoccupied states with higher chance of filling. This high filling chance area corresponds to the critical ionization energy ( $E_C$ ) (Figure 1-16). In addition, the DOS is dependent to the bonding or valence in the atom and you can identify these ELNES by comparing the fingerprints [13, 25, 26, 28, 30].

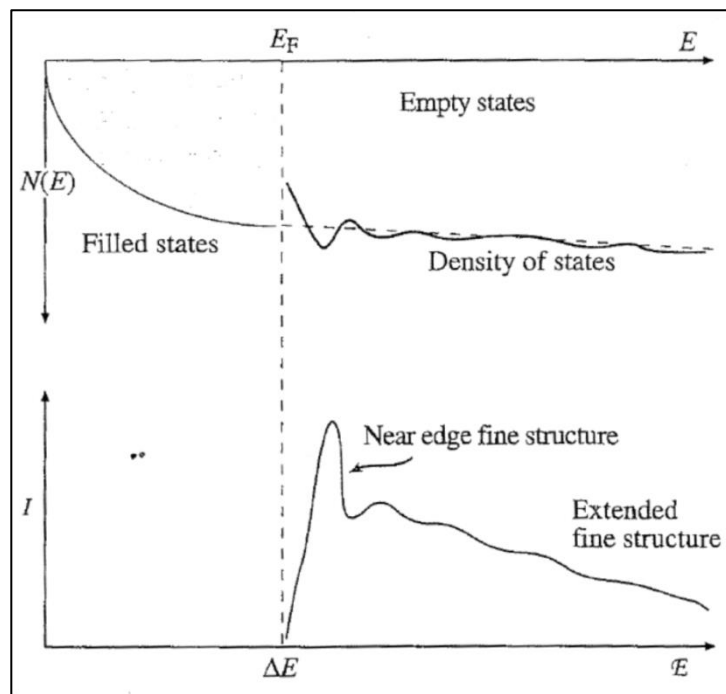


Figure 1-16 Diagram of the empty density of state and ELNES in the fine structure [28].

White lines are intense edges in the spectrum and occur when the electrons reside in distinct empty levels instead of a wide coherent states (Figure 1-17).

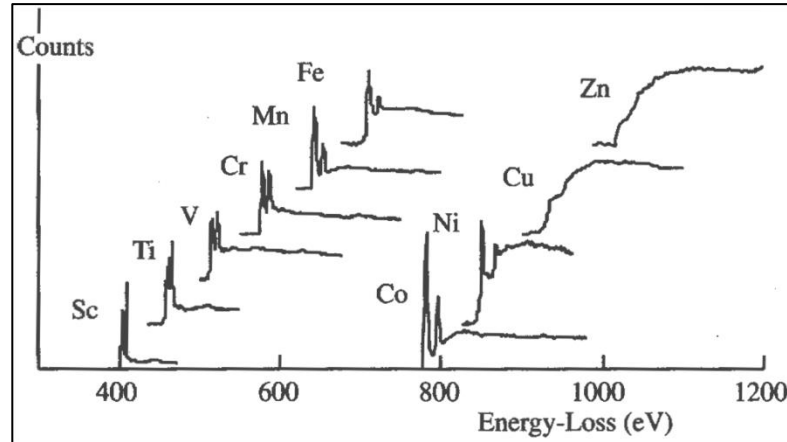


Figure 1-17 Ionization edge energies change in different elements, and white lines reflects the existence of unfilled d-band [28].

(c) Applications of EELS

Elemental analysis (Quantitative analysis) Energy of ionization edges is specific for each element and by extrapolating and subtracting the background, the quantity of the element can be obtained. To measure the quantity, we need to identify the integral of the intensity of ionization edge in which plural scattering has been removed. It assumes that no angular restrictions for intensities. The following equation will obtain [25-28].

$$I_k = P_k I_T \quad (9)$$

Where  $I_k$  is K-edge intensity, which is associated with the chance of ionization,  $P_k$  is the probability of ionization and  $I_T$  is the total transmitted intensity. For a thin specimen the  $I_T$  considers as the incident intensity (without backscatter and absorption



effects) and also electrons experience single scattering, therefore equation can be changed to the following form:

$$P_k = N_{\sigma k} \exp (-t/\lambda_k) \quad (10)$$

Where N equal to the number of atoms per unit area, which involves in obtaining the k edge. Single scattering leads to the large mean free path so equation 3 can be written as follow:

$$I_k \approx N \sigma_k I_T \quad (11)$$

And also

$$N = I_k / \sigma_k I_T \quad (12)$$

Then the number of the number of atoms per area can be quantified. For elements A and B  $I_T$  drops out and the following equation is obtained.

$$N_A/N_B = (I_K^A \sigma_K^B) / (I_K^B \sigma_K^A) \quad (13)$$

Use of chemical shifts and near-edge fine structure: The shape of the ELNES is affected by the neaberest-neighbor coordination, as a result of changes in the structure. Thus by utilizing a fingerprinting approach, in which recording reference spectra (Figure 1-17). from standard samples, we can determine the chemistry of them and interpret the spectra. In addition, in transition metals  $L_3/L_2$  (fine structures) changes can be measured for determining the valence states. Wang et al (1999) demonstrated the changes of valence states of Mn and Co ( $L_3/L_2$ ) by using Energy-filtered imaging (EFTEM). Therefore, we can get significant information such as bonding, valences and coordination [25-28].

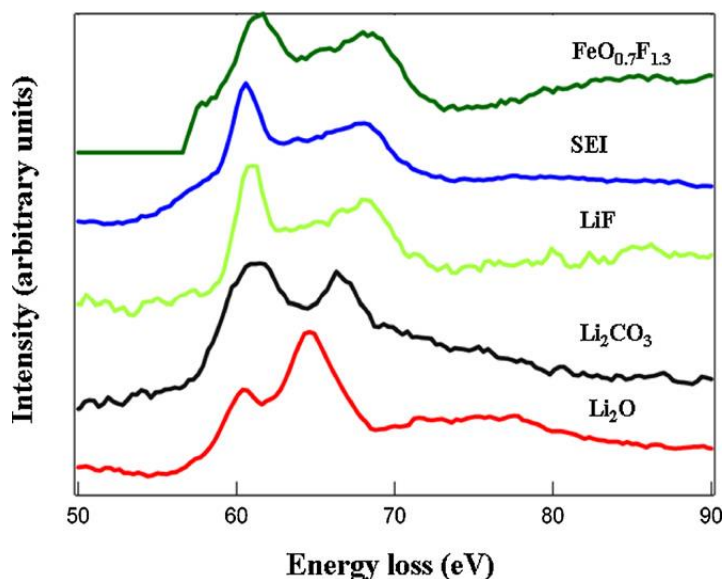


Figure 1-18 Li K-edge near-edge fine structure is taken from different lithium compounds,  $\text{Li}_2\text{O}$ ,  $\text{Li}_2\text{CO}_3$ ,  $\text{LiF}$ , SEI, and lithiated  $\text{FeO}_{0.7}\text{F}_{1.3}$  with 1.68 Li.

A series of Li-K edges are collected from various Li compounds (Figure 1-18) the Li threshold is the energy position at the half height of the edges energy. The Li thresholds for different compounds are different, and it shifted toward higher energy for elements with higher electronegativity. Each spectrum (Figure 1-18) contains two Li edges and the distance between these peaks as well as the peak position are characteristics for identifying the Li compounds [13, 25, 26, 28, 30]

Determining transition metal valence state: Valuable information about the density of states (DOS) of unoccupied states can be obtained by characterizing the white lines of transition elements.  $L_3$  and  $L_2$  (white lines) attributed to the transition of electrons from  $2P_{3/2}$  and  $2P_{1/2}$  to unoccupied 3d-states (respectively). Fe- $L_{2,3}$  edges of  $\text{FeF}_2$  are shown in Figure 1-19. It has been reported that there is a linear correlation between the

total intensity of the white line and the number of unoccupied states. The valence states can be measured based on their  $L_3$  over  $L_2$  intensity ratio and also the sum of the their intensities divided by the continuous L edge contribution. Different methods have been proposed to measure valence states of the transition metals such as Maximum-intensity method, Pearson method, Curve fitting method, and Positive second derivative method. Positive second derivative is taking the positive components of the second derivative under  $L_3$  and  $L_2$  edges (Figure 1-19). We used Positive second derivative method for measuring relative intensity of  $L_3/L_2$  of fluorine base materials [13, 25, 26, 28, 30].

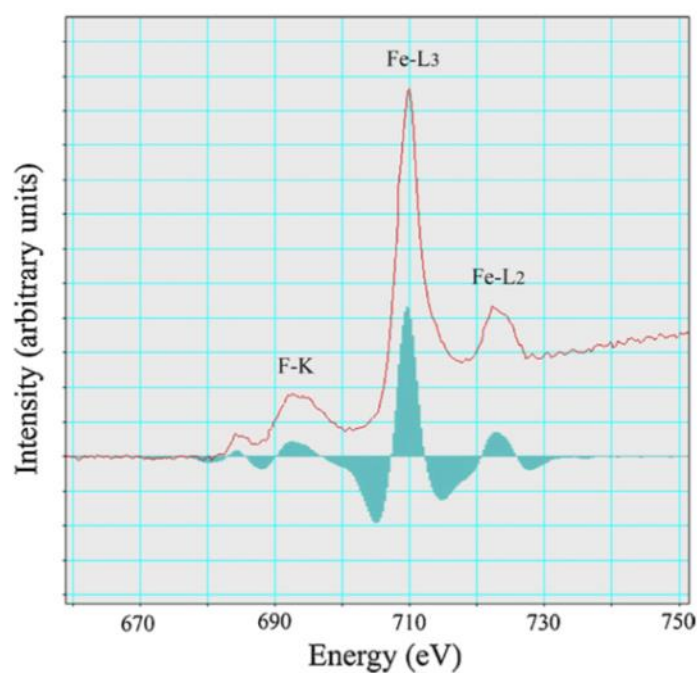


Figure 1-19 Second derivative (solid green) of FeOF/C spectrum.

### 1.3. Thesis objectives

Metal fluorides such as FeOF, FeF<sub>2</sub> and FeF<sub>3</sub>, conversion positive electrodes, are promising materials for Li-ion batteries due to their high specific capacity, low cost and low environmental impact. However, significant issues including voltage hysteresis and poor cycling performance have limited their applications. STEM/EELS can provide insights on the structural changes as well as phase distributions of the converted materials on nanoscale. Thus, understanding the microscopic changes of the cycled electrodes is critical to control and optimize the electrochemical performance. In this work TEM/STEM, electron diffraction, and EELS techniques are used to better identify the correlation between structural changes and capacity fade after cycling.

## 2. Structural phase transformation and Fe valence evolution in $\text{FeO}_x\text{F}_{2-x}/\text{C}$ nanocomposite electrodes during lithiation and de-lithiation processes <sup>1</sup>

### 2.1. Abstract

In this study, the structural changes of  $\text{FeO}_x\text{F}_{2-x}/\text{C}$  during the first discharge and recharge cycles were studied by ex-situ electron microscopy techniques including annular dark field scanning transmission electron microscopy (DF-STEM) imaging, selected area electron diffraction (SAED) and electron energy loss spectroscopy (EELS) as well as by in-situ X-ray absorption spectroscopy (XAS). The evolution of the valence state of Fe was determined by combined EELS using the Fe-L edge and XAS using the Fe-K edge. The results of this investigation show that conversion reaction path during 1st lithiation is very different than the re-conversion path during 1st delithiation. During lithiation, intercalation is first observed followed by conversion into a lithiated rocksalt (Li-Fe-O-F) structure, metallic Fe and LiF phases. During delithiation, the rocksalt phase does not disappear, but co-exists with an amorphous (rutile type) phase formed initially by the reaction of LiF and Fe. However, a de-intercalation stage is still observed at the end of reconversion similar to a single phase process despite the coexistence of these two (rocksalt and amorphous) phases.

### 2.2. Introduction

Lithium ion batteries are now widely used as rechargeable energy storage for a variety of electronic applications ranging from appliances to laptops and cell phones. At

---

<sup>1</sup>[31. Sina, M., et al., *Structural phase transformation and Fe valence evolution in  $\text{FeO}_x\text{F}_{2-x}/\text{C}$  nanocomposite electrodes during lithiation and de-lithiation processes*. J. Mater. Chem. A, 2013. **1**(38): p.

the present time, intercalation compounds are used almost exclusively for the positive electrodes but despite their success, their practical capacity remains limited in the range of 120 to 200 mAh/g [1, 4, 32].

This limitation is caused in part to the intercalation process which limits the charge transfer to one electron per transition metal. In order to improve the capacity of positive electrodes, conversion materials are being explored where all the valence states of the transition metal are used leading to higher theoretical capacities. In particular, reversible conversion materials based on metal fluorides have been considered due to their high theoretical capacity (500 to 750 mAh/g) at intermediate voltages (2-3 V) [5, 7, 8, 18, 33, 34]. Conversion materials have been explored since the 70's as primary battery electrode but their more recent resurgence has been enabled through the use of metal fluoride/carbon nanocomposites [5]. Numerous systems have now been explored such as  $\text{FeF}_2$  [6, 7, 35]  $\text{NiF}_2$  [7],  $\text{CoF}_2$  [7],  $\text{TiF}_3$ ,  $\text{FeF}_3$  [7, 8, 11, 21, 33-38],  $\text{BiF}_3$  [11, 12, 19] and  $\text{CuF}_2$  [6, 19, 21, 39]. In these conversion systems, the cycling performance is strongly dependent on their synthesis method, fluoride chemistry, cycling rate and temperature. For  $\text{FeF}_2$ , direct two phase conversion to metallic Fe (3nm in size) and LiF has been observed with the possible formation of a bi-continuous network thus allowing for a high conductivity path [6]. In contrast, the poor reversibility of  $\text{CuF}_2$  was attributed to  $\text{Cu}^{1+}$  dissolution upon charge [19]. For system with possible multiple valence states ( $\text{Fe}^0$ ,  $\text{Fe}^{2+}$  and  $\text{Fe}^{3+}$ ) such as for the  $\text{FeF}_3$  system, more complex phase transformation reactions are occurring involving first intercalation with possible phase transformation from initial rhombohedral to a defective tri-rutile phase followed by conversion into metallic Fe and LiF [10, 40].

In the search for conversion materials with improved capacity and cycle life, iron oxyfluoride nanocomposites have been explored due to the high theoretical specific capacity of about 885 mAh/g [14] for  $\text{Fe}^{3+}\text{OF}$  after full reduction of  $\text{Fe}^0$  to its metallic state. This system is also of interest as  $\text{FeOF}$  has the same rutile ( $\text{p4}_2/\text{mnm}$ ) structure as  $\text{FeF}_2$  but with higher  $\text{Fe}^{+3}$  valence state. In addition, it has been shown recently that single phase  $\text{FeO}_x\text{F}_{2-x}$  with a range in oxygen content  $x$  from 0 to 0.7 can be synthesized by a single synthesis processing path [14].

Studying the structural transformations that accompanied lithiation and delithiation is important in order to optimize the performance of the compound and to understand phenomena such as voltage hysteresis and transformation kinetics. However, for  $\text{FeO}_x\text{F}_{2-x}$ , more in-depth studies of the structural changes during cycling are needed. X-ray diffraction (XRD) measurements of the  $\text{FeO}_x\text{F}_{2-x}$  electrodes revealed first a Li intercalation process into rutile followed by a phase transformation into Fe metallic, LiF and an intermediate mixed cubic rocksalt-spinel phase (Li-Fe-O) for 1.6 Li [14]. Recent STEM-EELS analysis with sub-nanometer spatial resolution, show the presence of Fe and a rocksalt structured Li-Fe-O-F phase with  $\text{Fe}^{+2.3}$  valence state and with a Fe/O concentration ratio of 0.8 [13]. These results are also consistent with in-situ Mossbauer results showing the presence of both  $\text{Fe}^{2+}$  as well as  $\text{Fe}^0$  metallic although these experiments have been performed at room temperature. Upon complete conversion at the lowest voltage of 0.8V, the cubic Li-Fe-O-F phase transforms to metallic  $\text{Fe}^0$ , LiF and  $\text{Li}_2\text{O}$  [13, 14]. Recently, in-situ pair distribution function (PDF) analysis has been performed on  $\text{FeO}_x\text{F}_{2-x}/\text{C}$  (with  $x = 0.49$  and  $x = 0.60$ ) nanocomposites [41] showing detailed results on molar fraction of Fe containing phases (rutile, rocksalt and iron) as a

function of lithiation and delithiation. In addition, the presence of an amorphous rutile type structure is also reported in this PDF study. However, PDF obtained from X-Ray data is most sensitive to high Z elements containing phases such as Fe phases but is not sufficient sensitive for determining the presence of LiF or Li<sub>2</sub>O phases. On the theory side, only one first-principles study has been published on iron oxyfluorides and lithiation of FeOF [42]. In this study by density functional theory (DFT), intercalation up to 0.5 Li is confirmed with Li occupying octahedral sites along the 001 direction O/F channels. Conversion is also predicted by theory but with LiFe<sup>3+</sup>O<sub>2</sub> rocksalt phases in equilibrium with Fe, LiF. At the present time, the role of oxygen content x in FeO<sub>x</sub>F<sub>2-x</sub>/C on rocksalt phase formation, chemistry and valence state is still unknown. Despite these early results, details of this structural phase transformation starting with intercalation at low Li content and followed by conversion at higher Li content is at present not fully understood. Furthermore, the re-conversion process is now known to form an amorphous phase or with short-range order but whose structure, valence and chemistry is not yet known.

In view of the complex conversion mechanisms occurring during lithiation and delithiation of FeO<sub>x</sub>F<sub>2-x</sub>/C nanocomposites, it is necessary to perform experiments with a range of techniques in order to provide information on all aspects of phase formation such as structure, chemistry and presence of all phases, including LiF as well as direct measurement of Fe valence state. In this study, we performed a set of experiments on FeO<sub>x</sub>F<sub>2-x</sub> to study structural phase transformation using a combination of ex-situ TEM techniques including annular dark field (ADF) STEM imaging for determining formation of Fe nanoclusters, electron energy loss spectroscopy (EELS) for distribution analysis of all elements (Fe, O, F and Li) and for LiF phase formation via F near-edge structure, as



well as for Fe valence state determination and finally selected area electron diffraction (SAED) for phase identification. In addition phase formation and Fe valence was also determined by in-situ X-ray absorption near edge structure (XANES) spectroscopy. In this investigation, most experiments we performed on  $\text{FeO}_x\text{F}_{2-x}/\text{C}$  nanocomposites with oxygen content of  $x = 0.7$  ( $\text{FeO}_{0.7}\text{F}_{1.3}$ ) with additional data obtained for chemistries with O content of  $x = 0.5$  ( $\text{FeO}_{0.5}\text{F}_{1.5}$ ).

## **2.3. Experimental procedure:**

### **2.3.1. Material synthesis and electrode fabrication**

The iron oxyfluoride nano-powders were synthesized via a solution process involving reacting iron metal with fluorosilicic acid aqueous solution [14]. The resulting  $\text{FeSiF}_6 \cdot 6\text{H}_2\text{O}$  precursor was then annealed in air between 150 and 300 °C to synthesize  $\text{FeO}_x\text{F}_{2-x}$  nanoparticles 20 nm in size with  $x$  ranging from 0 to 1.  $\text{FeOF}$  is found to co-exist with  $\text{FeF}_3$  and  $\text{Fe}_2\text{O}_3$  phases but single phase  $\text{FeO}_x\text{F}_{2-x}$  is observed for  $x = 0.7$  and lower [14]. The  $\text{FeO}_x\text{F}_{2-x}/\text{C}$  nano-composites were then prepared by high-energy ball milling with 15 wt% activated carbon black (Asupra, Norit) for 1 hour in helium atmosphere. For in-situ XANES experiments, plastic electrodes were fabricated using the Bellcore [43] developed process consisting of mixing the active materials with poly (vinylidene fluoride-cohexafluoropropylene) (Kynar 2801, Elf Atochem), carbon black (SuperP, MMM), and dibutyl phthalate (Aldrich). The resulting electrodes typically consisted of 57% active material and 12% carbon black. For ex-situ TEM experiments, nanocomposites were mixed with 10% carbon black. No plastic binder or plasticizers

were used in order to facilitate disassembling the cells and extracting the powder electrode. Further experimental details on electrode preparation can be found elsewhere [14].

### **2.3.2. Electrochemistry**

Transformation kinetics, capacity and reversibility of conversion electrodes are dependent on both cycling rate and temperature. For iron fluorides [7], it has been found that optimum conditions are obtained for cycling in the 50 to 70 °C range with higher temperatures allowing faster charge-discharge rates. In this study, all ex-situ samples for STEM imaging, EELS and SAED were obtained electrochemically in galvanostatic mode at 60°C using a constant current density of 50mA/g. The coin cells were assembled in a He-filled glove box with a lithium-foil counter electrode and a 1 M LiPF<sub>6</sub> in ethylene carbonate:dimethyl carbonate (EC:DMC) as the electrolyte [14]. A custom build cell was used for in-situ XANES experiments with electrochemical cycling performed between 1.5 and 4.3V at 50 °C using a lower constant current density of 24mA/g.

### **2.3.3. Transmission Electron microscopy**

The samples for TEM characterization were prepared by disassembling the cells after electrochemical lithiation/delithiation in a He glove box. The powder electrodes were washed in DMC and a few drops were placed onto a TEM lacey carbon film supported on a copper grid. The grids were preserved in He sealed bags and then transferred to the electron microscope.

High resolution transmission electron microscopy (HRTEM) and annular dark field scanning transmission electron microscopy (ADF-STEM) images, selected area electron diffraction (SAED) pattern and electron energy loss (EELS) spectra were

obtained using a JEOL 2010F microscope operated at 197 kV equipped with a Gatan GIF 200 spectrometer. The STEM-EELS spectrum imaging experiments were also recorded at 197 kV with a Hitachi 2700 STEM equipped with a Gatan Enfina EELS spectrometer. The EELS spectra energy resolution was 0.7 eV and utilized a collection half angle ( $\beta$ ) of 20 mrad and convergence angle ( $\alpha$ ) of 10 mrad. As fluorine compounds are sensitive to the electron beam, the SAED patterns and STEM/EELS spectrum imaging experiments were taken with maximum dose of 40 C/cm<sup>2</sup> and a total dose of 5x10<sup>3</sup> C/cm<sup>2</sup> respectively to minimize electron beam damage.

SAED intensity profiles were obtained using Process Diffraction program [23] by taking the rotational average followed by background removal. Simulations of SAED patterns for nano-sized particles in the 2-5 nm range were obtained ab-initio by solving the Debye equation using JEMS program [44].

#### **2.3.4. In-situ X-ray Absorption Spectroscopy (XAS)**

In-situ Fe K-edge XAS spectra were collected in the transmission mode at beamlines X18A and X19A at the National Synchrotron Light Source (NSLS) using a Si (111) double-crystal monochromator. The beam intensity was reduced by 30% to minimize the high order harmonics. The charge-discharge cycling of the FeO<sub>0.7</sub>F<sub>1.3</sub>/C electrode during in-situ measurements was performed between 1.5 and 4.3V at 50 °C using a constant current density of 24 mA/g to ensure complete conversion and reconversion reactions, and to finish the experiment within the assigned beam time. For this purpose, a customized in situ heating cell holder was designed and used during the in-situ experiments. The in situ spectra were continuously collected while the cell was cycled. Reference spectra of a metallic Fe foil were simultaneously collected with the

corresponding in-situ spectra for energy calibration. The collected in-situ X-ray absorption near edge structure (XANES) spectra were processed using standard procedures with the Athena software [45].

## **2.4. Results.**

### **2.4.1. Initial microstructure**

After synthesis, the  $\text{FeO}_x\text{F}_{2-x}/\text{C}$  nanocomposite is composed of uniformly distributed crystals embedded in a carbon matrix as shown in the HRTEM image of Figure 2-1(a). The dark field image depicted in Figure 2-1(b) reveals a fairly uniform distribution of nanoparticles with an average particle size of 15-20 nm. The valence state of Fe was measured as 2.7 by Mossbauer spectroscopy leading to a nanocomposite of composition  $\text{FeO}_{0.7}\text{F}_{1.3}/\text{C}$ . A similar Fe valence state of 2.8 was measured also by EELS using the white line Fe  $L_3/L_2$  intensity ratio [13]. The electron diffraction pattern of the initial  $\text{FeO}_{0.7}\text{F}_{1.3}/\text{C}$  nanocomposite shown in Figure 2-1(c) confirms the existence of a single phase as observed by X-ray [14] with a well crystallized rutile structure of space group  $\text{P4}_2/\text{mm}$ .

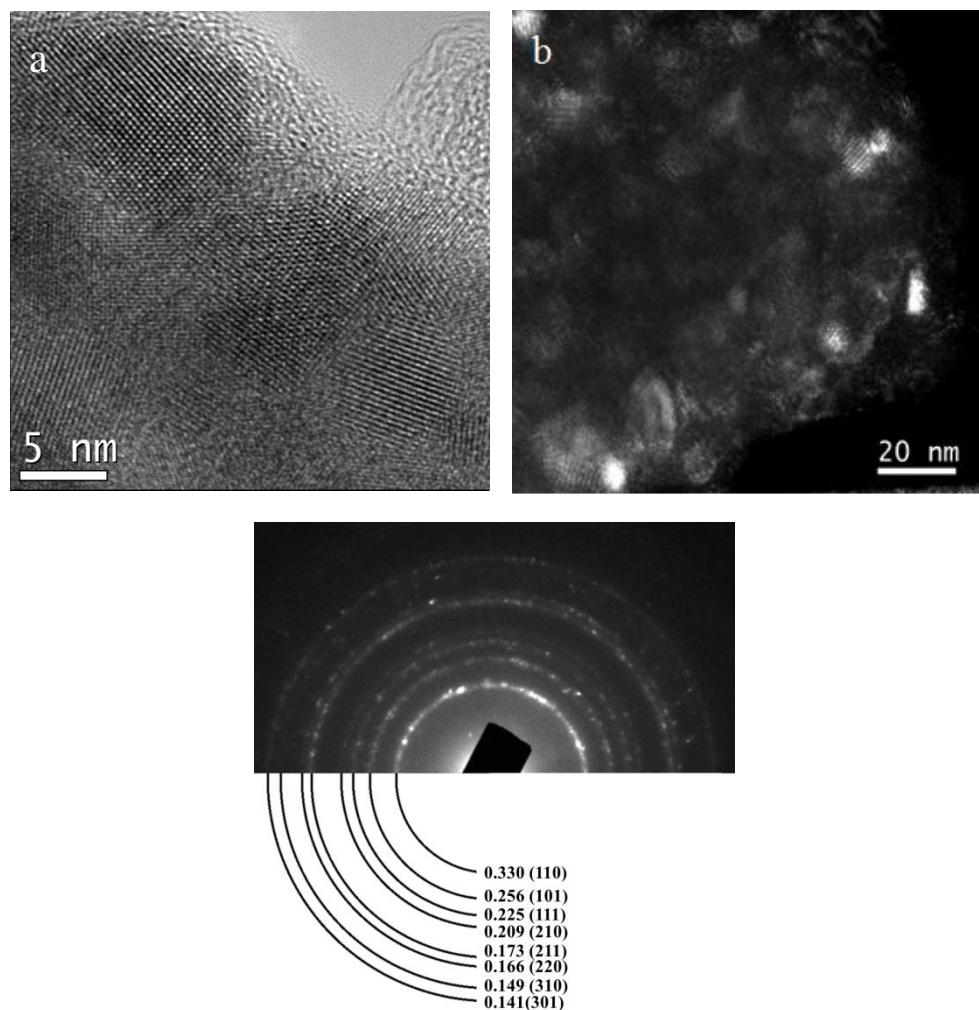


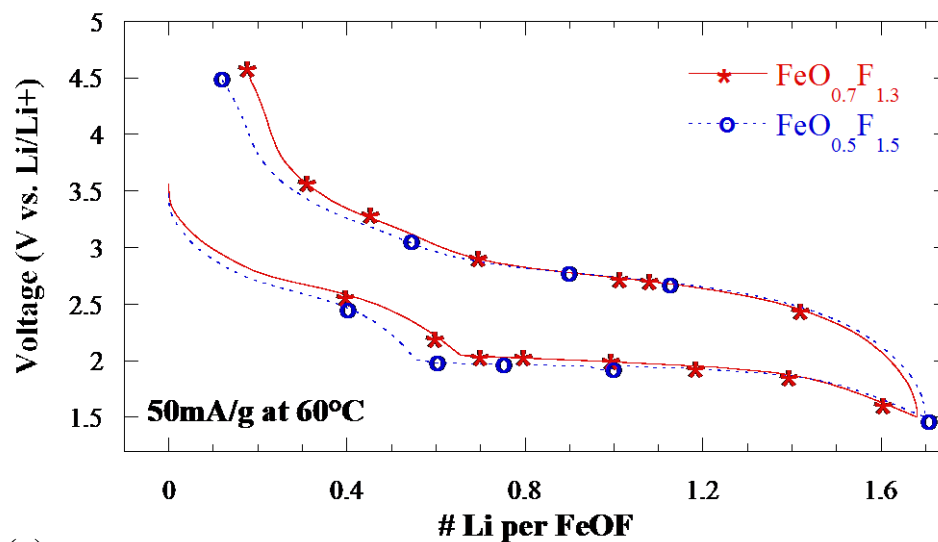
Figure 2-1 (a) High resolution TEM image (b) dark Field TEM image and (c) SAED pattern of as synthesized  $\text{FeO}_{0.7}\text{F}_{1.3}/\text{C}$  nanocomposite. The diffraction rings are expressed in nm with the corresponding (hkl) rutile reflections.

#### 2.4.2. Electrochemistry

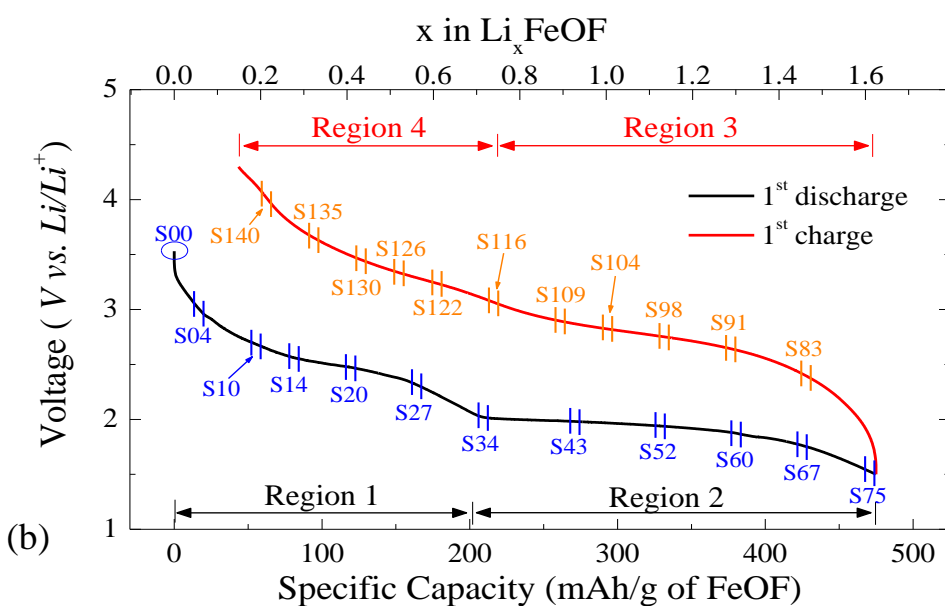
The electrochemical performances of two  $\text{FeO}_{0.7}\text{F}_{1.3}/\text{C}$  and  $\text{FeO}_{0.5}\text{F}_{1.5}/\text{C}$  nanocomposites chemistries are shown in Figure 2-2(a) where the electrode was cycled at  $60^\circ\text{C}$  between 1.5 and 4.5 V versus  $\text{Li}/\text{Li}^+$  under a constant current density of 50 mA/g. The respective open circles and stars on the curves indicate conditions where the ex-situ TEM samples were collected. For the  $\text{FeO}_{0.7}\text{F}_{1.3}/\text{C}$  chemistry, the voltage profile exhibits

a continuous decrease from 3.5 to 2.1 V (Li content  $x = 0$  to 0.68) followed by a second redox plateau with a slow decrease from 2.1 V to 1.5 V (Li content  $x = 0.68$  to 1.68). The specific capacity for the first discharge cycle between 1.5 and 4.5 V is 490 mAh/g of  $\text{FeO}_{0.7}\text{F}_{1.3}$ . The lithiation profiles reveal excellent correlation with theoretically expected lithiation stoichiometry. For FeOF, the theoretical capacity in the 1.5 and 4.5 voltage range is 590 mAh/g [14]. Upon re-charge, a continuously inclining curve is observed with voltage profile showing possibly 3 different regions. However, the transitions (during recharge) between these three regions are less pronounced than during discharge. For the  $\text{FeO}_{0.5}\text{F}_{1.5}/\text{C}$  chemistry, a similar behavior is observed but with a transition to the second redox plateau occurring for a lower Li content of 0.6.

The 1st discharge-charge curves of  $\text{FeO}_{0.7}\text{F}_{1.3}/\text{C}$  nanocomposite electrode during in-situ XAS measurements are shown in Figure 2-2(b). The cell was cycled at 50 °C using a constant current density of 24 mA/g between 1.5 and 4.3 V versus  $\text{Li}/\text{Li}^+$ . The scan numbers marked on the curves indicate conditions where the in-situ XAS spectra were collected for further analysis. Although the discharge capacity is slightly less than that from the cell for ex-situ TEM shown in Figure 2-2(a) (e.g., 475 vs. 490 mAh/g), the electrochemical profile of the in-situ cell is quite similar to the one used for ex-situ TEM experiments ensuring good correspondence between the two sets of experiments despite the slight difference in charge-discharge rate (24 vs. 50 mA/g) and temperature (50 vs. 60 °C)



(a)



(b)

Figure 2-2 (a) First discharge-charge voltage profile of  $\text{FeO}_{0.7}\text{F}_{1.3}/\text{C}$  and  $\text{FeO}_{0.5}\text{F}_{1.5}/\text{C}$  nanocomposite used for ex-situ TEM experiment marked by circles. (Cycling rate of 50 mA/g at 60°C) (b) First discharge-charge voltage profile of  $\text{FeO}_{0.7}\text{F}_{1.3}/\text{C}$  nanocomposite during in situ XAS experiment. The scan numbers marked on the curves indicate where the in situ XAS spectra were taken for further analysis (Cycling rate of 24 mA/g at 50°C).

### 2.4.3. Electron Diffraction and STEM/EELS results

#### 2.4.3.1. Lithiation of $\text{FeO}_{0.7}\text{F}_{1.3}/\text{C}$ nanocomposite

The selected area electron diffraction (SAED) patterns of  $\text{FeO}_{0.7}\text{F}_{1.3}/\text{C}$  nanocomposite after discharge to 2.12 V (0.6 Li) and 1.5 V (1.68 Li) are shown in Figure 2-3(a) and Figure 2-3(b) respectively revealing a transition from rutile to cubic structures consisting of superposition of metallic Fe plus rocksalt reflections. This gradual transition from rutile to Fe plus rocksalt phases is shown in the series of electron diffraction intensity profiles depicted in fig.

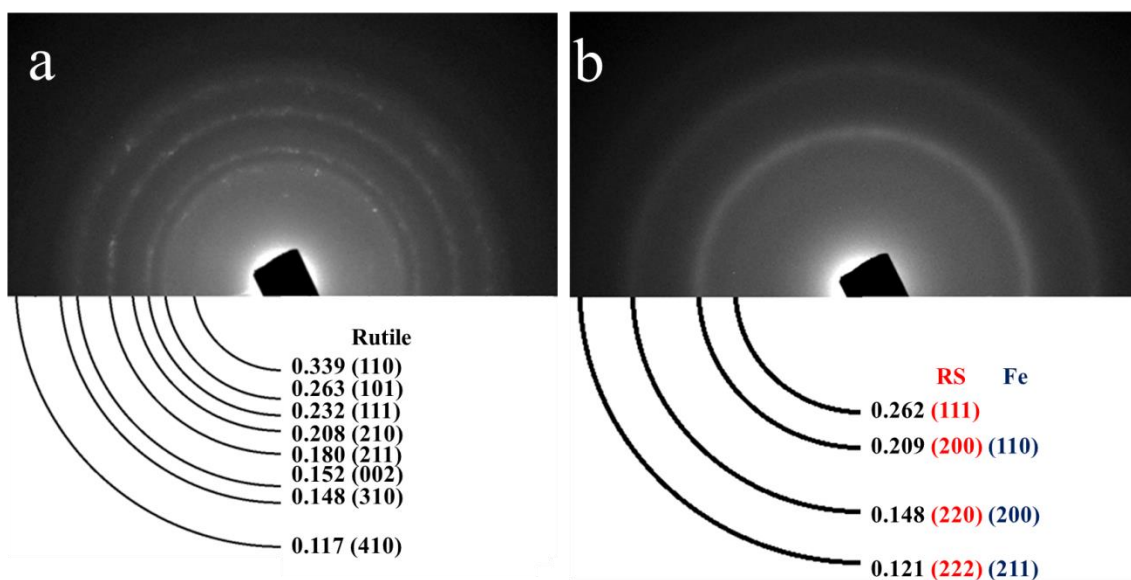


Figure 2-3 SAED pattern of  $\text{FeO}_{0.7}\text{F}_{1.3}/\text{C}$  after discharge to a) 2.12 V (0.6 Li) and b) 1.5 V (1.68 Li). The diffraction rings are expressed in nm with the corresponding (hkl) reflections for rutile in (a) and superposition of rocksalt (RS) and bcc Fe in (b)

Upon lithiation from  $x = 0$  to  $x = 0.7$ , the rutile (110) reflection shifts toward larger d-spacings indicative of volume expansion (about 5%) upon lithium insertion into



the structure and reduction of  $\text{Fe}^{3+}$  to the larger  $\text{Fe}^{2+}$  ion. A gradual decrease in the intensity of the first rutile (110) reflection ( $3.03 \text{ nm}^{-1}$ ) is also observed up to 0.7 Li (c.f. Figure 2-4) and disappears faster than the other rutile reflections. Actually, the rutile (101) and (211) reflections with  $3.8 \text{ nm}^{-1}$  and  $5.55 \text{ nm}^{-1}$  reciprocal lattice spacings respectively become relatively more intense up to 0.8 Li, which can be attributed to transformation from rutile to a new lithiated rutile II structure ( $\text{Li}_x\text{FeO}_{0.7}\text{F}_{1.3}$ ). In this new phase, there are four prominent reflections with reciprocal d-spacings of 3.8, 4.35, 5.55 and  $6.58 \text{ nm}^{-1}$ . For 0.7 Li and higher, two new reflections at  $4.78 \text{ nm}^{-1}$  and  $6.76 \text{ nm}^{-1}$  start to form, reaching their maximum intensity for 1.68 Li.

These two peaks can be attributed to the formation of rocksalt phase with (200) and (220) miller indices. The first (111) reflection at  $4.17 \text{ nm}^{-1}$  of the rocksalt phase is very weak which can be simulated using a lithiated rocksalt phase with (non-ordered) Li substitution for Fe in the lattice. Also, this low peak intensity (almost nonexistent) and the absence of other reflections below  $4.78 \text{ nm}^{-1}$  are further indication of the formation of a rocksalt structure instead of spinel phase. Ordering of O and F in the rutile structure has been reported experimentally [46] and theoretically [42] but no evidence for F/O ordering has been found in the rocksalt phase. The transformation from lithiated rutile II to cubic rocksalt coincide with the beginning of the plateau-like region observed at 0.68 Li in the voltage profile curve shown in Figure 2-2(a) and Figure 2-2(b). Due to the overlap between rocksalt and Fe reflections, the presence of Fe cannot be obtained from diffraction alone but can be inferred from the presence of a strong contrast in the ADF-STEM images as shown in Figure 2-4(b) and Figure 2-4(c) for 0.7 and 0.8 Li content respectively.

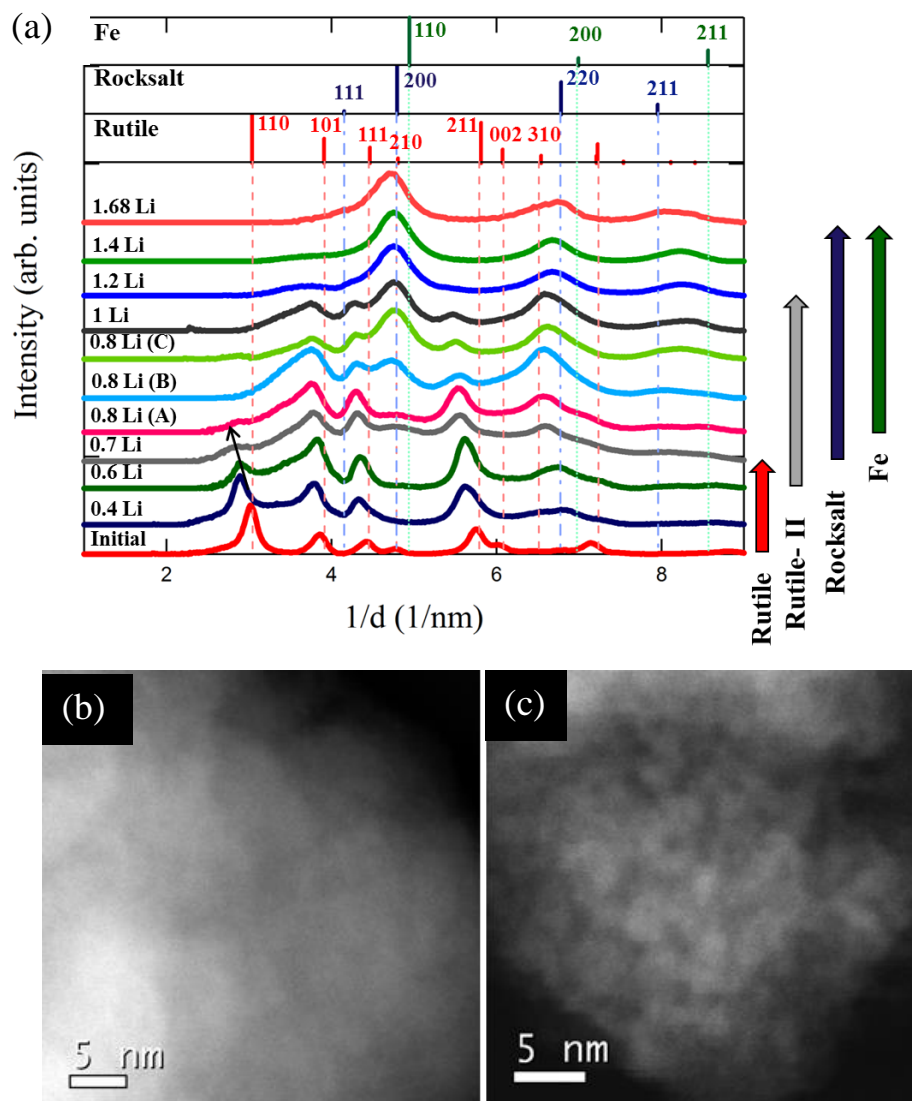


Figure 2-4 (a) SAED intensity profile of  $\text{FeO}_{0.7}\text{F}_{1.3}/\text{C}$  as a function of Li content. For 0.8 Li, the microstructure is highly in-homogeneous and the intensity profiles from three different areas marked A,B,C are depicted in the graph. Also shown in the graph are the positions of the reflections for rutile, rocksalt and Fe phases with (hkl) indices of the most intense reflections. The corresponding annular dark field STEM images of  $\text{FeO}_{0.7}\text{F}_{1.3}/\text{C}$  lithiated with (b) 0.7 Li, and (c) 0.8 Li.

As ADF-STEM images have a contrast which scales as  $Z^2$ , the contrast observed in Figure 2-4(c) is indicative of the presence of Fe nanoparticles with particle sizes in the 2-3 nm range. A contrast associated with Fe nanoparticles has not been observed for 0.7

Li. For 0.8 Li content, a range of SAED intensity profile marked 0.8 Li A,B or C in Figure 2-4(a) has been observed. It can be observed that the (200) and (220) rocksalt reflections  $4.78$  and  $6.76\text{ nm}^{-1}$  have increasing intensity from A to C, suggesting that lithiation and associated phase transformation is not uniform within the sample. From DF-STEM images, the presence of Fe nanoparticles is observed for 0.8 Li content and higher. However, the presence of a small diffraction peak, at  $4.78\text{ nm}^{-1}$  for 0.7 Li content, would suggest that the Li-Fe-O-F rocksalt phase precedes the nucleation of crystalline Fe nanoparticles. Upon further lithiation to 1.68 Li (1.5V), the reflections associated with rutile II phase type reflections are no longer visible and the crystal structure has converted completely to Fe and Li-Fe-O-F rocksalt phases. The phase evolution of the  $\text{FeO}_{0.5}\text{F}_{1.5}/\text{C}$  nanocomposite shown in Figure 2-5 is identical to  $\text{FeO}_{0.7}\text{F}_{1.3}/\text{C}$  with only the apparition of (200) and (220) rocksalt reflections  $4.78$  and  $6.76\text{ nm}^{-1}$  occurring at lower Li content of 0.6 instead of 0.7. This early rocksalt phase formation is similar to what is observed electrochemically from the early occurrence of the second redox plateau. In addition, Fe nanoparticles are also forming at lower Li content for  $\text{FeO}_{0.5}\text{F}_{1.5}/\text{C}$  as depicted in Figure 2-5(b) and Figure 2-5(c). The Fe nanoparticle sizes measured from the dark field STEM images are 2.3 and 2.4 nm for  $\text{FeO}_{0.7}\text{F}_{1.3}/\text{C}$  and  $\text{FeO}_{0.5}\text{F}_{1.5}/\text{C}$  sample respectively with the combined Fe plus rocksalt particle sizes measured from dark field TEM images corresponding to 3.6 and 3.4 nm respectively.

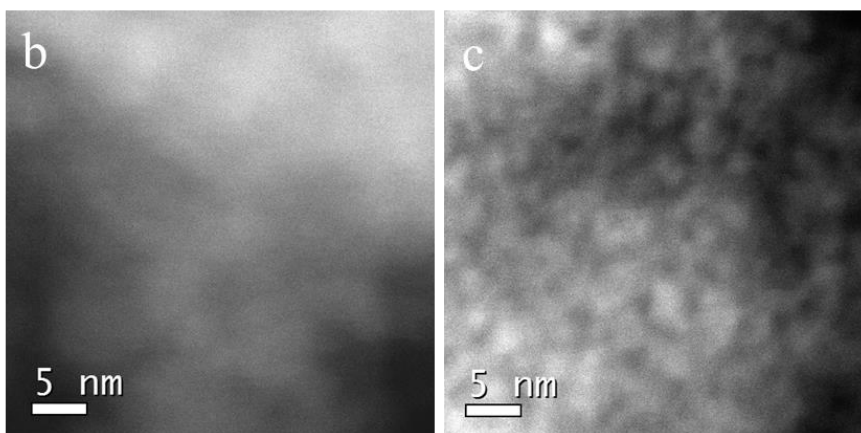
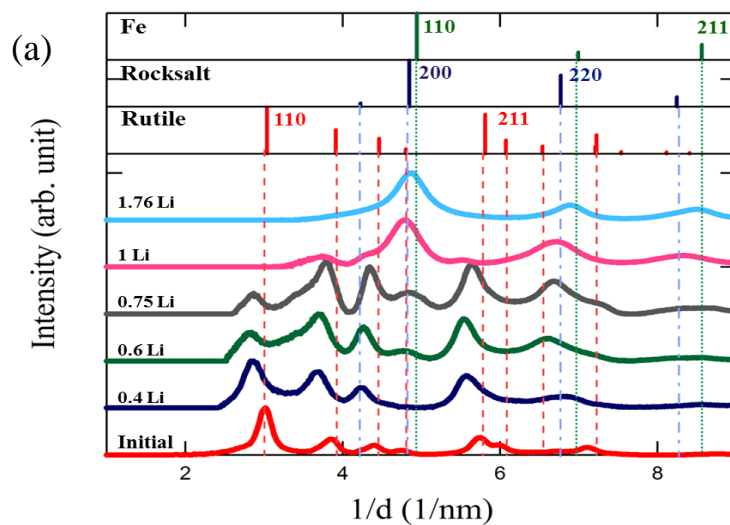


Figure 2-5 (a) SAED intensity profile of  $\text{FeO}_{0.5}\text{F}_{1.5}/\text{C}$  as a function of Li content. Also shown in the graph are the positions of the reflections for rutile, rocksalt and Fe phases with (hkl) indices of the most intense reflections. The corresponding annular dark field STEM images of  $\text{FeO}_{0.5}\text{F}_{1.5}/\text{C}$  lithiated with (b) 0.6 Li, and (c) 0.75 Li.

The formation of LiF is also expected to occur with the apparition of the cubic reflections, however reflections associated with LiF have not been observed. This could be attributed in part to the much lower atomic scattering factor for LiF and lower crystallinity. Indeed, recent molecular dynamic simulations have revealed that for  $\text{FeF}_2$ , the initial LiF nuclei are amorphous which then crystallize upon further growth [47].

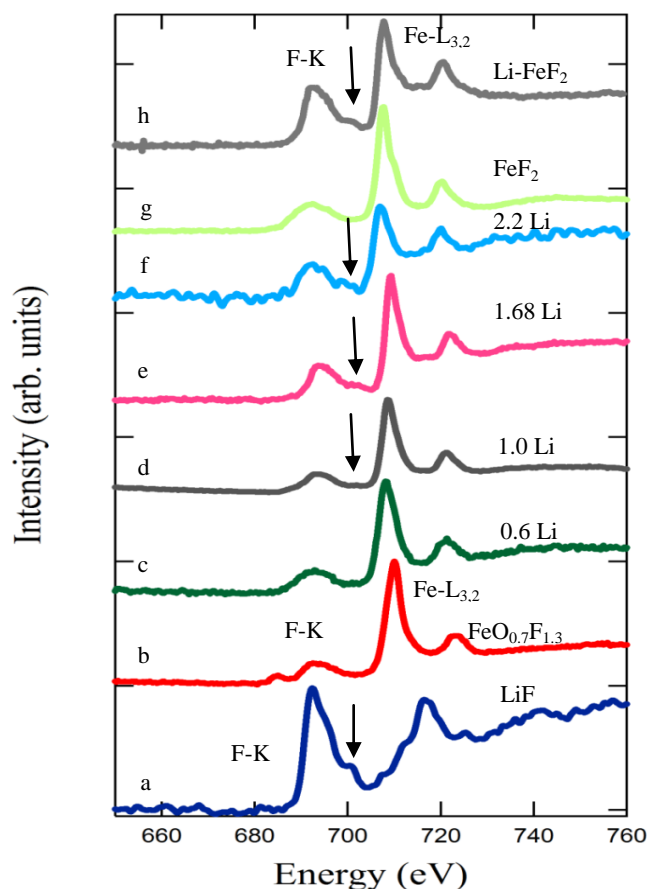


Figure 2-6 Typical EELS spectra showing (a) F-K edge of standard LiF with characteristic post peak at 700 eV marked by an arrow, and F-K and Fe-L<sub>3,2</sub> edges of (b) initial FeO<sub>0.7</sub>F<sub>1.3</sub>, (c) lithiated with 0.6 Li, (d) lithiated with 1.0 Li (e) lithiated with 1.68 Li (f) lithiated with 2.2 Li. Also shown are the F-K and Fe-L<sub>3,2</sub> edges for (g) initial FeF<sub>2</sub> and (h) lithiated FeF<sub>2</sub>

This is in contrast to lithiation of FeF<sub>2</sub> with atomic Li showing clearly the formation of crystalline LiF [48]. Despite the lack of diffraction evidence, the presence of LiF can be inferred indirectly by EELS from the presence of a small post peak on the F K-edge as shown in Figure 2-6. The standard F-K edge for LiF shown in Figure 2-6(a) consists of two intense peaks with a small post peak at 700 eV marked by an arrow. Such a post peak is characteristic of LiF and is absent in either FeO<sub>0.7</sub>F<sub>1.3</sub> (spectrum b), FeF<sub>2</sub> (spectrum g) or FeF<sub>3</sub> [35]. There is an overlap between the second F-K peak and Fe-L<sub>3,2</sub> edges but the first F-K and post peaks are clearly separated from the Fe-L edge. The evolution of F K-edge as function of lithiation is summarized in Figure 2-6. The F post

peak is visible for 1.0 Li, 1.68 Li and 2.2 Li as marked by arrows in spectra d, e and f respectively. The fact that the post peak is observed for 1.0 Li after the formation of rocksalt (Li-Fe-O-F) phase occurring for 0.7 Li is indicative that the F post peak is solely attributed to the presence of LiF and not associated with F in the rocksalt phase.

An ADF STEM image and associated O K-edge, F K-edge and F L-edge elemental maps are shown in Figure 2-7(a) to (d) respectively. As expected the bright contrast in the DF-STEM image is associated with the phase with the highest average Z corresponding to Fe nanoparticles.

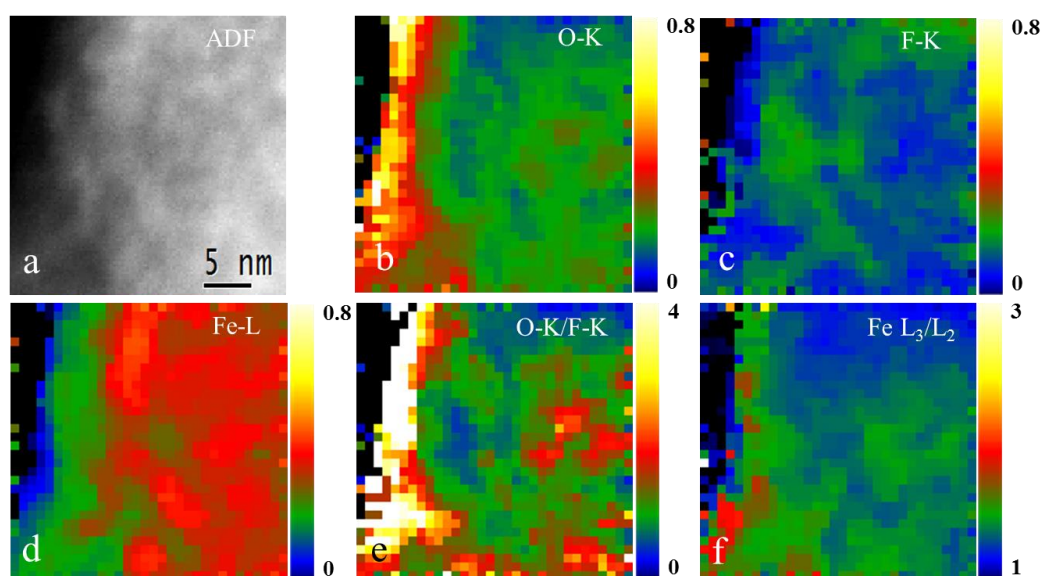


Figure 2-7 (a) ADF-STEM image of FeO<sub>0.7</sub>F<sub>1.3</sub> lithiated with 1.68 Li and corresponding concentration maps in at% for (b) O-K, (c) F-K, (d) Fe-L and (e) O-K/F-K atomic ratio with in (f) the Fe valence map expressed as Fe L<sub>3</sub>/L<sub>2</sub> intensity ratio.

At the surface edge, an oxygen rich layer is observed which has been attributed to the formation of a Li-rich SEI layer [13]. Due to the overlap of the different phases (Fe, Li-Fe-O-F and LiF) which are 3-5 nm in size as compared to the TEM sample thickness

which is about 20-30 nm, an accurate determination of chemical composition and valence state of the various phases cannot be obtained. Nevertheless some general observations can be made. In addition to the presence of metallic Fe nanoparticles, there is a phase separation into O-rich and F-rich phases as revealed in the O-K/F-K ratio map of Figure 2-7(e). Fluorine rich areas are associated with LiF while oxygen rich areas are associated with the Li-Fe-O-F cubic rocksalt phase. This phase separation occurs to within a 5 nm range. This oxygen rich phase is also the one with the highest valence state as shown on the Fe  $L_3$  over  $L_2$  intensity map of Figure 2-7(f). A quantitative EELS analysis of this Li-Fe-O-F rocksalt phase revealed a O/Fe atomic ratio of 1.4 [13] with a Fe valence state of  $2.3 \pm 0.3$ . Additional measurements of Fe valence state for various Li content during lithiation and delithiation are presented in section 3.2.3.

#### **2.4.3.2. Delithiation of $\text{FeO}_{0.7}\text{F}_{1.3}/\text{C}$ nanocomposite**

Two SAED patterns of  $\text{FeO}_{0.7}\text{F}_{1.3}/\text{C}$  re-charged to 2.4 V (1.42 Li) and 4.5 V (0.18 Li) are shown in Figure 2-8(a) and (b) respectively. The diffraction pattern for 1.42 Li is similar to 1.68 Li (c.f. Figure 2-3(b)) with diffraction ring intensities corresponding to the superposition of Fe and Li-Fe-O-F rocksalt phases. However, the re-charged  $\text{FeO}_{0.7}\text{F}_{1.3}/\text{C}$  sample does not reveal the typical rutile structure of the initial sample depicted in Figure 2-1(c) but contains only diffuse rings. The evolution of the electron diffraction intensity profiles during delithiation is depicted in Figure 2-9 as a function of Li content. The intensity of the peaks  $I_1$  at  $4.85 \text{ nm}^{-1}$  and  $I_2$  at  $6.85 \text{ nm}^{-1}$  which for 1.68 Li correspond to the superposition of reflections from both rocksalt and Fe phases remain present throughout the re-charge process but become broader with changes in their relative intensity. A plot of their intensity ratios ( $I_1/I_2$ ) as a function of Li content  $x$  is shown in

Figure 2-10 for both chemistries  $\text{FeO}_{0.7}\text{F}_{1.3}/\text{C}$  and  $\text{FeO}_{0.5}\text{F}_{1.5}/\text{C}$ . This intensity ratio is larger for  $\text{FeO}_{0.5}\text{F}_{1.5}/\text{C}$  than for  $\text{FeO}_{0.7}\text{F}_{1.3}/\text{C}$  composition which is indicative of an increase in the fraction of Fe nanoparticles as oxygen content decreases.

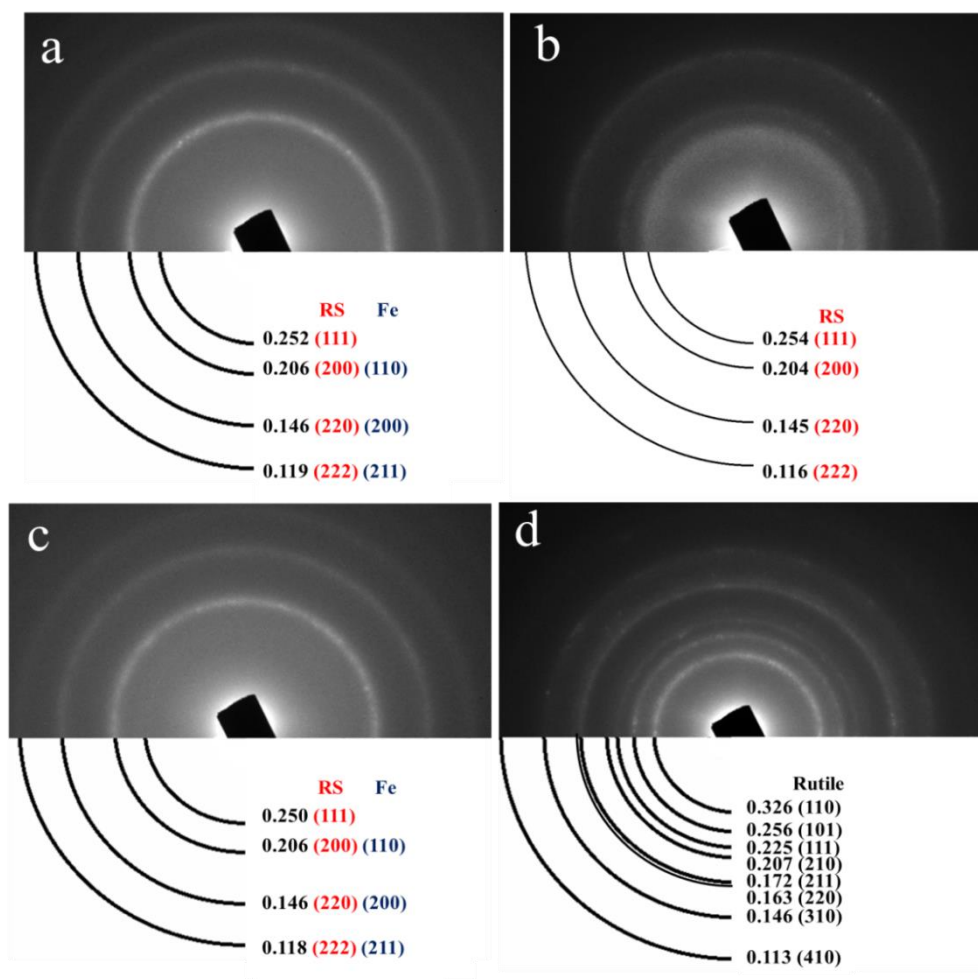


Figure 2-8 SAED patterns of delithiated  $\text{FeO}_{0.7}\text{F}_{1.3}/\text{C}$  with a) 1.42 Li and b) 0.18 Li with corresponding patterns c) 1.4 Li and d) 0.18 Li after irradiation with an electron dose of 780 C/cm<sup>2</sup>. The diffraction rings are expressed in nm with the corresponding (hkl) reflections corresponding to the superposition of rocksalt (RS) and bcc Fe in (a) and (c), rocksalt (RS) with amorphous ring in (b) and rutile in (d). Electron beam induced crystallization from rocksalt-amorphous to crystalline rutile is occurring in the delithiated electrode.



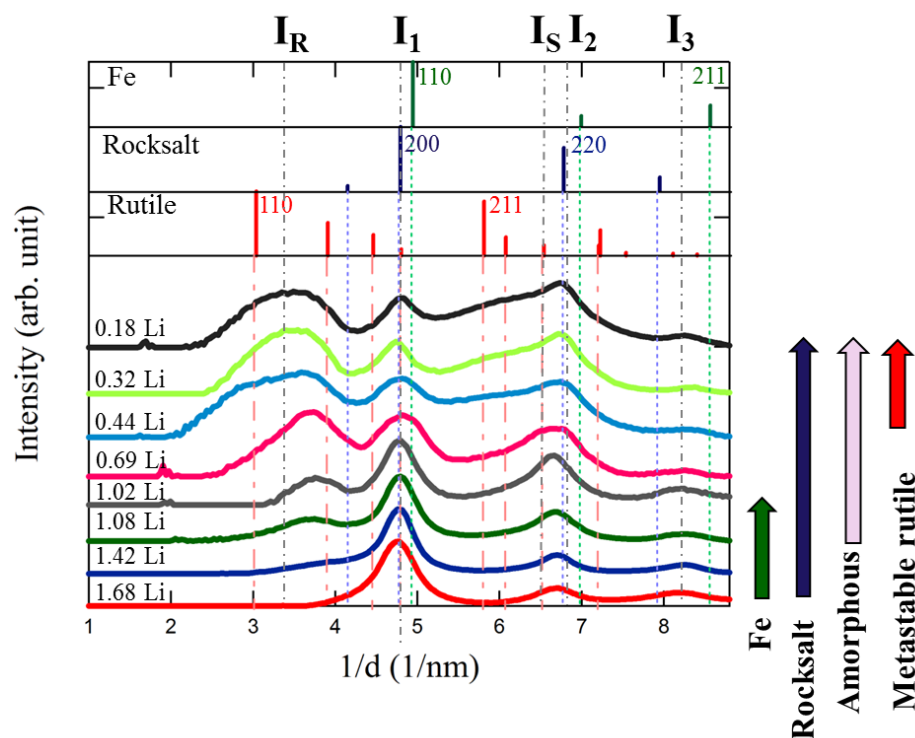


Figure 2-9 (a) SAED intensity profiles during delithiation of  $\text{FeO}_{0.7}\text{F}_{1.3}/\text{C}$ . Also shown in the graph are the positions of the reflections for rutile, rocksalt and Fe phases with (hkl) indices of the most intense reflections.

A quantitative analysis of diffracted intensities gives an Fe molar fraction of 0.5 and 0.6 for  $\text{FeO}_{0.7}\text{F}_{1.3}/\text{C}$  and  $\text{FeO}_{0.5}\text{F}_{1.5}/\text{C}$  respectively. In Figure 2-10, a sharp decrease in intensity is observed upon delithiation followed by a plateau which can be ascribed to the disappearance of metallic Fe nanoparticles. For  $\text{FeO}_{0.5}\text{F}_{1.5}/\text{C}$  sample, this transition occurs at a lower Li content than for  $\text{FeO}_{0.7}\text{F}_{1.3}/\text{C}$  (0.77 Li versus 0.90 Li). The associated dissolution of the Fe nanoparticles can be observed clearly in the ADF-STEM images shown in Figure 2-11 for  $\text{FeO}_{0.7}\text{F}_{1.3}/\text{C}$  and  $\text{FeO}_{0.5}\text{F}_{1.5}/\text{C}$  sample chemistries. From extrapolation of the  $I_1/I_2$  intensity ratio curves extrapolations depicted in Figure 2-10, a

precise measurement of Fe nanoparticles dissolution occurs for Li content of 0.77 and 0.90 for  $\text{FeO}_{0.7}\text{F}_{1.3}/\text{C}$  and  $\text{FeO}_{0.5}\text{F}_{1.5}/\text{C}$  sample chemistries respectively.

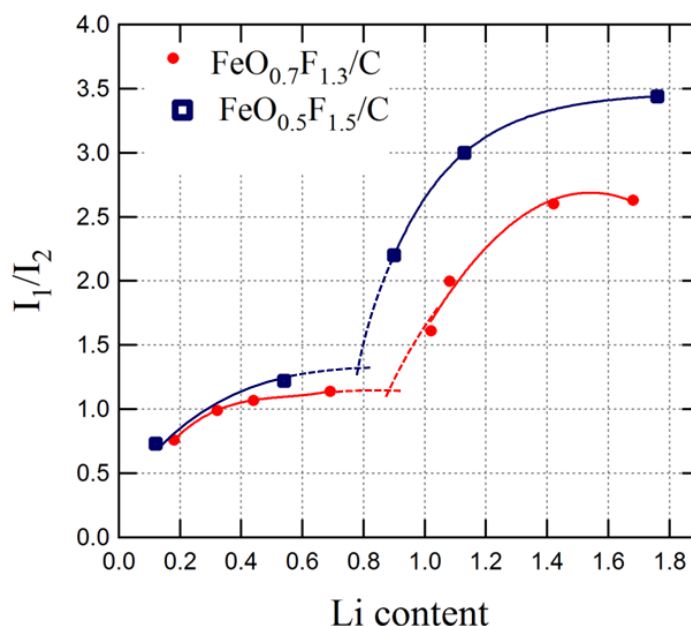


Figure 2-10 Evolution of  $I_1/I_2$  diffracted peak intensity ratio as a function of Li content obtained during first recharge cycle for  $\text{FeO}_{0.7}\text{F}_{1.3}/\text{C}$  and  $\text{FeO}_{0.5}\text{F}_{1.5}/\text{C}$  electrode compositions.

In addition to the cubic phase reflections associate with metallic Fe and rocksalt phases, two broad and diffuse peaks marked as  $I_R$  and  $I_S$  in Figure 2-9, appear at about 1.08 Li and increase in amplitude as Li content decreases. These peaks are associated with the formation of an amorphous phase. At a recharge voltage of 4.5V, the microstructure is a nanocomposite composed of an intimate mixture of a cubic rocksalt phase surrounded by an amorphous phase. An interesting point to note is that this nanocomposite microstructure formed during recharge is metastable and upon exposure

with a low electron dose of 440 to 780 C/cm<sup>2</sup> at 200 keV, it recrystallizes completely into rutile structure.

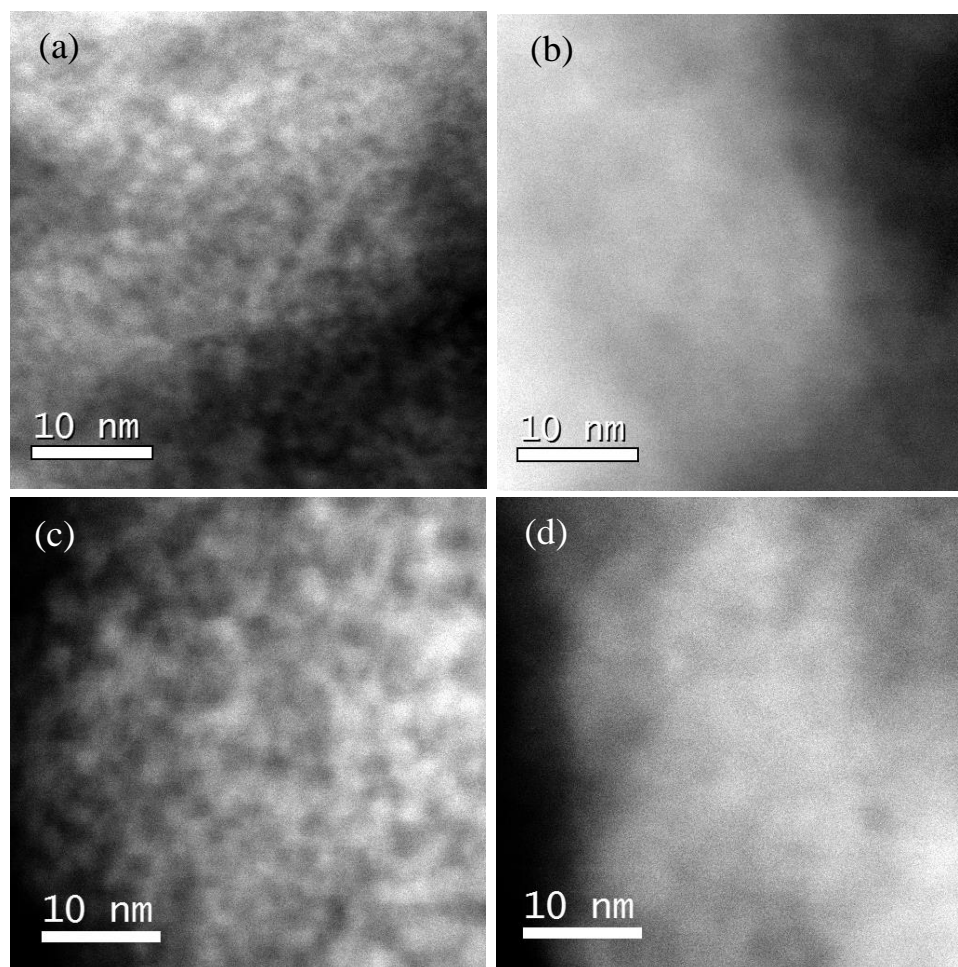


Figure 2-11 ADF- STEM images of (a)  $\text{FeO}_{0.7}\text{F}_{1.3}/\text{C}$  delithiated with 1.02 Li, (b)  $\text{FeO}_{0.7}\text{F}_{1.3}/\text{C}$  delithiated with 0.69 Li, (c)  $\text{FeO}_{0.5}\text{F}_{1.5}/\text{C}$  delithiated with 0.9 Li, and (d)  $\text{FeO}_{0.5}\text{F}_{1.5}/\text{C}$  delithiated with 0.54 Li.

This recrystallization phenomenon is shown in Figure 2-8(c) and Figure 2-8(d) the corresponding SAED patterns of Figure 2-8(a) and Figure 2-8(b) after electron beam irradiation. Such a recrystallization phenomenon has been reported previously for other

fluorides amorphous thin films such as  $\text{AlF}_3$  [49] and  $\text{FeF}_3$  [50] used as e-beam resists and is caused by knock-on displacement, enhanced diffusion and crystallization which is induced by the high energy electron flux. The tendency for the formation of crystalline rutile Li-Fe-O-F phase from the initial rocksalt/ amorphous nanocomposite is also correlated with lithium content. As delithiation reactions proceed from 0.44 to 0.18 Li, a lower electron dose is required for crystallization with a faster transition from short-range amorphous to long-range crystalline order. For 0.44 Li the (200) and (220) reflections of (Li-Fe-O-F) phase are still present while they have completely disappeared at full delithiation (0.18 Li). As delithiation occurs, less energy is required to reach full crystallization possibly from a decrease of the energy barrier from amorphous to crystalline phases. After crystallization, the diffraction peaks are identical to those of the initial undistorted rutile I structure.

Despite the total dissolution of Fe nanoparticles observed already for 0.69 Li (c.f. Figure 2-10), only de-lithiated  $\text{FeO}_{0.7}\text{F}_{1.3}/\text{C}$  samples with 0.44 Li, 0.32 Li and 0.18 Li have been found to recrystallize under the electron beam. This is an indication that despite the presence of two distinct phases (rocksalt and amorphous) they appear to be intimately mixed with similar local averaged chemistry and valence state. This Li range from 0.44 to 0.18 Li experiencing a transition to crystalline rutile has been denoted as metastable rutile in Figure 2-9.

#### **2.4.3.3. Fe valence determination by EELS (Fe L-edge)**

The valence state of transition elements such as Fe can be determined by EELS with nanometer spatial resolution by measuring the relative intensity of Fe- $\text{L}_3$  and Fe- $\text{L}_2$  white lines resulting from the transition of electrons from spin-orbit split level  $2p^{2/3}$  and

$2p^{1/2}$  to unoccupied 3d states [51, 52]. It has been found that the total  $L_3+L_2$  intensity decreases with increasing d-band occupancy [53]. In addition, the  $L_3/L_2$  intensity ratio and energy position of  $L_3$  and  $L_2$  lines are also strongly dependent on the d-band occupancy and therefore on the oxidation state of the transition element [35, 51, 54]. In this study, we have measured this  $L_3/L_2$  ratio to determine the Fe valence state during lithiation and delithiation processes. Details on  $L_3$  and  $L_2$  measurement methodology and Fe valence calibration can be found elsewhere [13]. The Fe valence states measured during lithiation and delithiation are summarized as a function of Li content  $x$  in Figure 2-12.

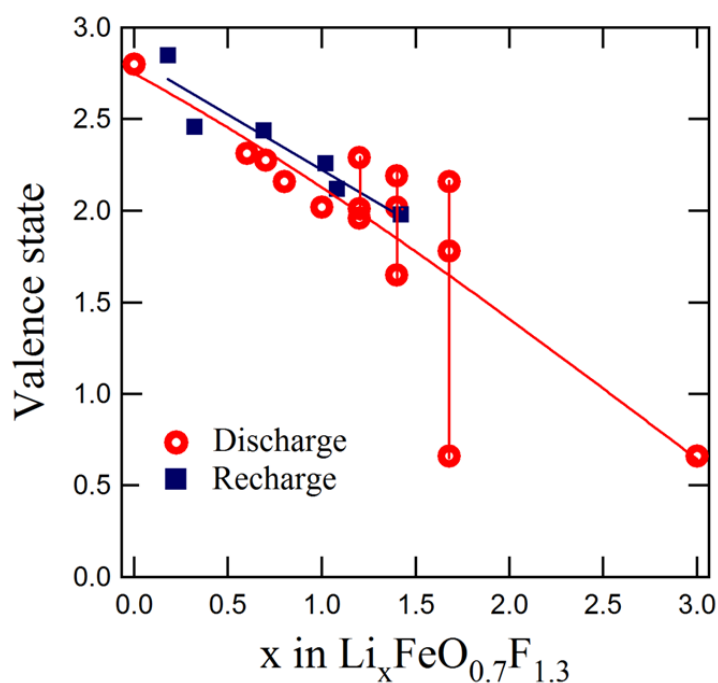


Figure 2-12 Average Fe valence state calculated from Fe  $L_3$  over  $L_2$  intensity ratio as a function of Li content  $x$  for discharge (round symbols) and recharge (square symbols) samples. For 0.8 and higher Li content, the data scatter increases due to the presence of two distinct Fe valence states. In addition to the average Fe valence value, the data also show the valence value for the oxygen rich phase.

First it can be seen that upon delithiation, the Fe valence state returns to its initial value of  $\text{Fe}^{+2.7}$ . Also, the general trends of average Fe valence as a function of Li content  $x$  are similar during lithiation and delithiation. It has been observed also that the scatter in Fe valence measurement increases at higher Li content which is indicative of conversion into two phases with two different valence states corresponding to metallic  $\text{Fe}^0$  and rocksalt  $\text{Li-Fe}^{+x}\text{-O-F}$ . The data corresponding to the 15% highest and lowest values are depicted during lithiation for 1.2, 1.4 and 1.6 Li content. As the EELS signal averages over the entire film thickness (20-30 nm) which is much larger than the Fe or rocksalt particles sizes in the 2-4 nm range, the reported values have an accuracy of about 15%. Based on these data reported in Figure 2-12, a valence value for Fe ranging from 2.3 to  $2.2 \pm 0.3$  at 1.3 and 1.67 Li respectively is determined for the rocksalt  $\text{Li-Fe}^{+x}\text{-O-F}$  phase. In view of the high spatial resolution obtainable by STEM/EELS analysis, it is possible to map the Fe valence state from a map of the  $\text{Fe L}_3/\text{L}_2$  ratio [13]. Such a map is shown in Figure 2-7(f) revealing a valence distribution in the 5nm range. As discussed previously [13], the highest Fe valence state corresponds to area having the highest oxygen content corresponding to the rocksalt phase.

#### **2.4.3.4. Fe valence determination by in-situ XANES results (Fe K-edge)**

The in-situ Fe K-edge from XANES spectra obtained during 1st discharge and charge are presented in Figure 2-13. The spectra can be divided into 4 regions based on the valence evolution and are marked in Figure 2-2(b) for a comprehensive comparison of the spectral feature changes. In region 1 showing a continuous voltage decline from 3.5 to 2.1V, the XANES spectra in Figure 2-13(a) clearly shows rigid edge shift toward lower energy in a continuous manner revealing continuous reduction in average Fe

oxidation state from  $\text{Fe}^{+2.7}$  to  $\text{Fe}^{+2}$  through lithium insertion into the rutile  $\text{FeO}_{0.7}\text{F}_{1.3}$  phase. The Fe valence state was determined from comparison with  $\text{Fe}^{+(2+x)}\text{O}_x\text{F}_{2-x}$  standard compounds with rutile structure. On the other hand, in region 2 corresponding to the voltage plateau at *ca.* 2.0V, the spectra shown in Figure 2-13(b) do not show rigid edge shifting but profile distorting centered on an isosbestic point located at *ca.* 7121 eV (circled region). The isosbestic point is common in spectroscopic data suggesting that two phases with distinct valence states co-exist (i.e., in this system,  $\text{Li}_x\text{-Fe}^{n+}\text{-O-F}$  and  $\text{Fe}^0$ ) with changing ratios of their fraction in the mixture, which contribute to the absorption around the isosbestic point. The relative molar fraction of  $\text{Li}_x\text{-Fe}^{n+}\text{-O-F}$  and  $\text{Fe}^0$  phases can be estimated from a linear combination of Fe K-edge from metallic iron and rocksalt phases. At the present time, there is no pure standard rocksalt phase of mixed composition (Li-Fe-O-F) available for modeling the Fe K-edge. However, as the position and shape of Fe K-edge is dependent on valence state and local environment, the Fe K-edge of the rocksalt salt phase has been approximated assuming the superposition of FeO and  $\text{FeF}_2$  standard compounds. Using this superposition, the residual fit is lower than for using only FeO rocksalt phase. Quantitative fit analysis of the Fe-K edge XANES spectra of  $\text{FeO}_{0.7}\text{F}_{1.3}/\text{C}$  nanocomposite discharge to 1.5V corresponding to lowest discharged state in this study (Curve S75) is shown in Figure 2-14. The best fit is obtained with superposition of metallic  $\text{Fe}^0$ , with  $\text{Fe}^{2+}\text{O}$  and  $\text{Fe}^{2+}\text{F}_2$  in molar fraction corresponding to 50.4%, 25.6% and 24%. This Fe molar fraction of about 50 % is comparable to the value obtained from simulation of peak intensities of the SAED patterns.

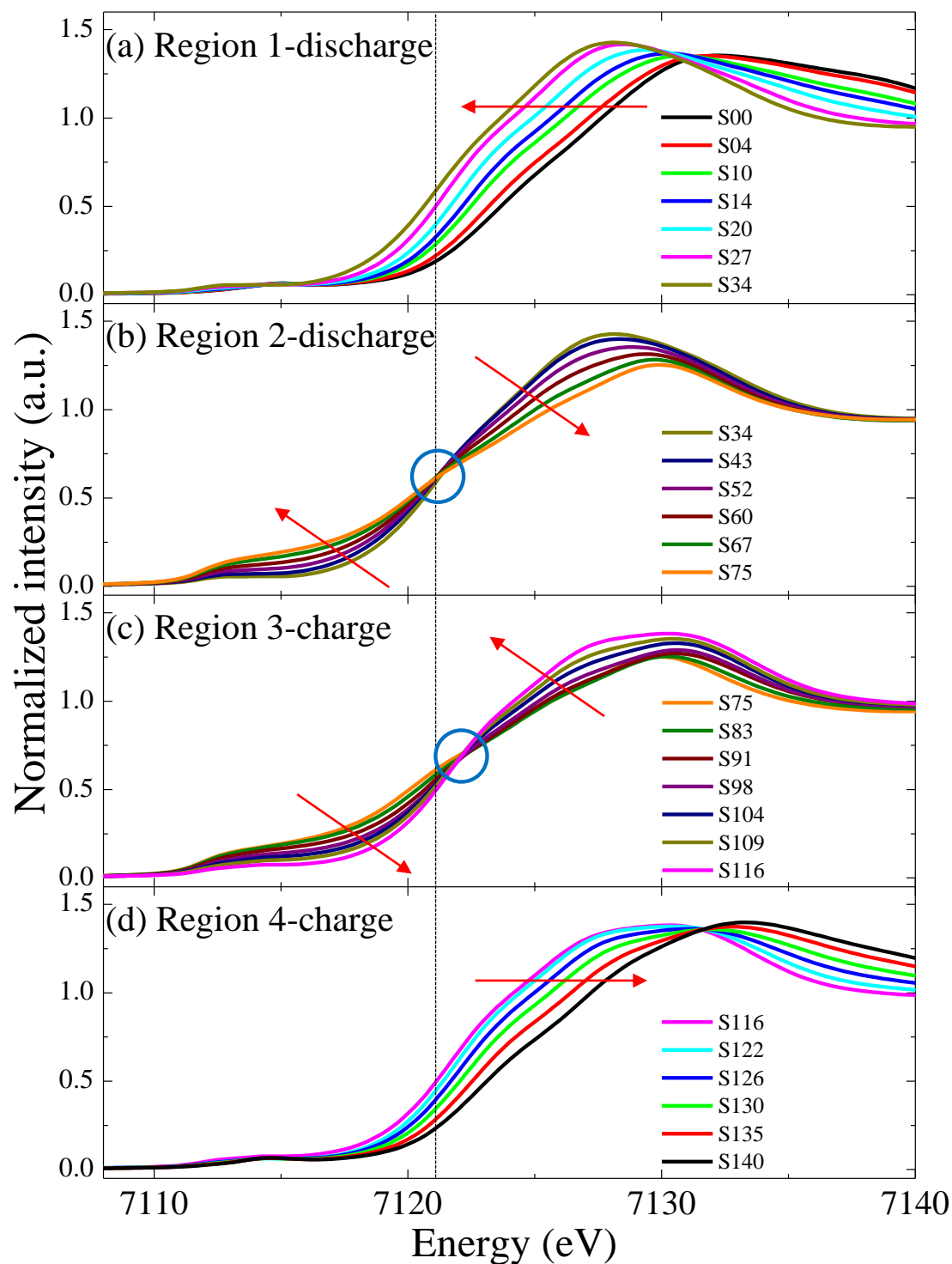


Figure 2-13 In situ Fe-K edge XANES spectra of  $\text{FeO}_{0.7}\text{F}_{1.3}/\text{C}$  nanocomposite during 1<sup>st</sup> discharge and 1<sup>st</sup> recharge. Graph (a) and (b) correspond to regions 1 and 2 marked in Figure 2-2(b) during 1<sup>st</sup> discharge while graph (c) and (d) correspond to regions 3 and 4 marked in Figure 2-2(b) during 1<sup>st</sup> recharge.



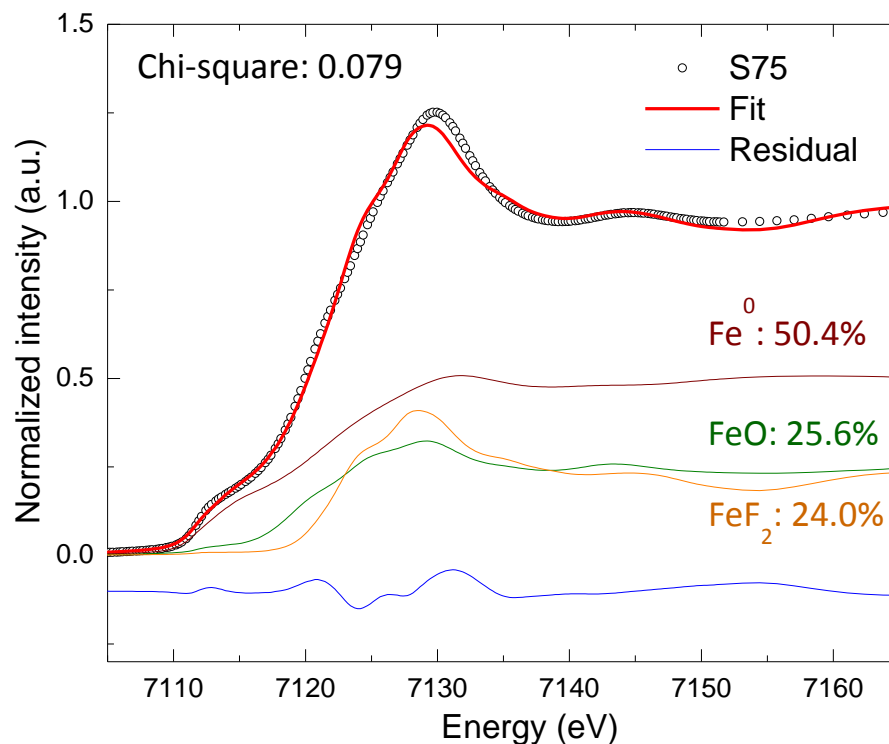


Figure 2-14 Quantitative fit analysis of the Fe-K edge XANES spectra of FeO<sub>0.7</sub> F<sub>1.3</sub>/C nanocomposite discharge to 1.5V corresponding to lowest discharged state in this study (Curve S75). The best fit is obtained with superposition of metallic Fe<sup>0</sup>, with Fe<sup>2+</sup>O and Fe<sup>2+</sup>F<sub>2</sub> in molar fraction corresponding to 50.4%, 25.6% and 24%

During the first recharge (delithiation), the spectra basically changed back reversibly to end with a spectrum close to the original spectrum of the pristine FeO<sub>0.7</sub>F<sub>1.3</sub>/C (curve S00). In region 3 shown in Figure 2-13(c), the spectra changes in the opposite manner to the spectral changes in region 2 with an isosbestic point, confirming the reversible reconversion reactions between Fe and lithiated iron oxyfluoride phase. However, it should be noted that the isosbestic point in this region 3 is slightly shifted to higher energy compared with that in region 2 during discharge revealing different reaction pathways during reconversion reaction. The exact composition of the lithiated phase which is being formed during reconversion reaction in the region 3 is unknown but

it may be the amorphous phase observed by diffraction with higher average Fe oxidation state than the one formed during discharge. In the following region 4, the entire edge continuously shifted back to higher energies as clearly shown in Figure 2-13(d) indicating continuous increase of average Fe oxidation state via lithium extraction from lithiated phase during reconversion reaction at voltages over ~3.1V.

## 2.5. Discussion

The results of this investigation show that the conversion reaction path of  $\text{FeO}_{0.7}\text{F}_{1.3}/\text{C}$  nanocomposite during 1<sup>st</sup> lithiation is very different than the reconversion path during 1<sup>st</sup> delithiation. During lithiation, intercalation is observed first, followed by a conversion reaction into Li-Fe-O-F rocksalt, Fe and LiF phases. During delithiation, the rocksalt phase is observed continuously up to the end of delithiation process, accompanying by the formation of an amorphous phase. However, as observed by XANES, a de-intercalation process is still observed at the end of reconversion process similar to a single phase process despite the coexistence of these two phases.

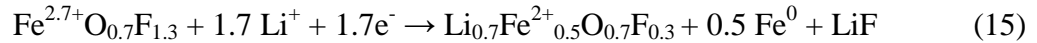
During initial discharge, Li intercalates into rutile leading to a lithiated rutile structure with expanded lattice parameter:



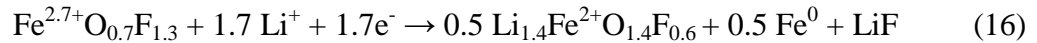
At  $x = 0.7$ , the  $\text{Li}_x\text{Fe}^{(2.7-x)+}\text{O}_{0.7}\text{F}_{1.3}$  starts to convert into a lithiated rocksalt type phase (Li-Fe-O-F) followed by the formation of metallic Fe as observed by ADF-STEM imaging. From EELS analysis, evidence for the apparition of LiF is also presented for 1.0 Li and higher as the F post-edge feature is associated exclusive to LiF but not rocksalt Li-Fe-O-F phase. In addition, the first (110) reflection of rutile disappear at 0.8 Li but the

remaining rutile reflections are still visible corresponding to a modified rutile II phase. This second stage is completed at the end of lithiation with 1.68 Li but rutile II type reflections have disappeared at 1.4 Li already (c.f. Figure 2-4(a)). The exact composition of the rocksalt Li-Fe-O-F phase has not yet been fully determined but a O/Fe concentration ratio for the rocksalt phase of 1.4 has been reported previously [13]. The Mossbauer spectroscopy results reported two valence state of +2 and 0 for Fe similar to present XANES analysis, while Fe valence states of +2.3 to +2.2  $\pm$  0.3 (depending on Li content) are measured by EELS. From XANES data, a transition is observed at 0.68 Li from a one phase intercalation process to a two phase reaction process with two different Fe valence state phases.

Based on these results the following lithiation reaction can be expressed at the end of lithiation at 1.5V corresponding to 1.7 Li:



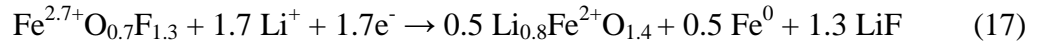
or



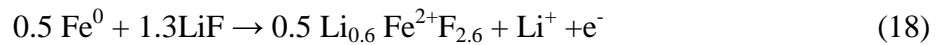
In the lithiated rocksalt phase  $\alpha$ -LiFe<sup>3+</sup>O<sub>2</sub> phase, Fe and Li occupy the same 4b lattice sites while O occupies the 4a lattice sites [55]. Substitution of O by F may occur with a corresponding reduction of Fe valence state. For Li<sub>1.4</sub>Fe<sup>2+</sup>O<sub>1.4</sub>F<sub>0.6</sub> described in equation 2b, only 1 Li can occupy 4b lattice sites with the remaining 0.4 Li possibly located in octahedral or tetrahedral interstitial sites. Experimentally, we know from EELS analysis that LiF is present but the amount of F or Li remaining in the rocksalt phase is at present unknown. The quantitative XANES fit analysis composed of the superposition of

metallic Fe, FeF<sub>2</sub> and FeO standards spectrum seems to indicate that O and F are both present in the rocksalt phase.

Alternatively, it can be envisioned that the rocksalt phase decomposes to form a high oxygen rocksalt phase with higher fraction of LiF than described in relations (2) and (3) with:



In contrast to lithiation path, rutile type reflections are not observed upon full delithiation but instead, rocksalt reflections are observed throughout delithiation process with in addition the occurrence of amorphous type reflections. Furthermore, Fe nanoparticles have been observed to disappear at 0.69 Li with XAS data showing a single Fe valence state (possibly Fe<sup>2+</sup>) for 0.72 Li and lower. These combined results are indicative of a delithiation process occurring in two stages. During the first stage (from 1.68 Li up to 0.69 Li) corresponding to removal of 1Li, Fe nanoparticles react solely with remaining LiF to form a partially lithiated amorphous phase that can be expressed as:



This lithiated phase has the same valence state as the remaining rocksalt phase (Li<sub>0.8</sub>Fe<sup>2+</sup>O<sub>1.4</sub>). During the second delithiation stage (0.69 Li to 0.18) where only one unique Fe valence state is observed by XAS and EELS, simultaneous delithiation of the rocksalt and amorphous phases is occurring.

The observed electron beam induced transformation of the combined amorphous plus rocksalt phases to crystalline undistorted rutile I, observed only during this second delithiation stage, indicates that these two phases are intimately mixed at the nanoscale

where only local atomic displacements are needed to form a unique phase with rutile structure similar to the initial rutile structure before lithiation. Due to the small scale of the amorphous rutile/rocksalt nanocomposite, we have not been able to determine their individual chemistry as a function of delithiation. However, some form of F and O exchange is expected to occur towards the end of discharge leading to a metastable two phase mixture (amorphous rutile and rocksalt) but with similar chemistry and Fe valence state. Further studies are in progress to determine the role of this highly disordered two phase mixture on cycling behavior of FeOF.

## 2.6. Conclusion

In this study, the structural changes of  $\text{FeO}_x\text{F}_{2-x}/\text{C}$  during the first discharge and recharge cycle were studied by ex-situ electron microscopy techniques including annular dark field scanning transmission electron microscopy (DF-STEM) imaging, selected area electron diffraction (SAED) and electron energy loss spectroscopy (EELS) as well as by in-situ x-ray absorption spectroscopy (XAS). The evolution of the valence state of Fe was determined by combined EELS using the Fe-L edge and XAS using the Fe-K edge. The results of this investigation show that conversion reaction path during 1<sup>st</sup> lithiation is very different than the re-conversion path during 1<sup>st</sup> delithiation. During lithiation, intercalation is first observed followed by conversion into a lithiated rocksalt (Li-Fe-O-F) structure, metallic Fe and LiF phases. During delithiation, the rocksalt phase does not disappear during delithiation, but co-exists up to the end of delithiation with an amorphous (rutile type) phase formed initially by the reaction of LiF and Fe. However, a de-intercalation stage is still observed at the end of reconversion similar to a single phase process despite the coexistence of these two (rocksalt and amorphous) phases.

### **3. Amorphous phase formation, electron beam induced crystallization and stability upon cycling in delithiated FeOF nanocomposites<sup>2</sup>**

#### **3.1. Abstract**

Lithiated  $\text{FeO}_{0.7}\text{F}_{1.3}/\text{C}$  undergoes a conversion reaction involving the transformation from rutile structure to Li-Fe-O-F rocksalt-type phase, metallic Fe and LiF. Upon delithiation, a gradual transformation from rocksalt (Li-Fe-O-F), Fe and LiF to a mixture of metastable amorphous rutile and rocksalt phases has been observed. The delithiated samples with amorphous rutile and nanocrystalline rocksalt phases have been found to intermix and recrystallize under the electron beam via a knock-on atomic displacement process to form a long-range crystalline rutile phase. We have used this phenomenon of electron irradiation induced recrystallization to study the formation and relative stability of amorphous phase upon delithiation. Also, the effects of electrochemical cycling on amorphous phase formation and stability has been explored. The recrystallization of amorphous rutile-rocksalt nanocomposites is dependent on the Li content and became more complete as the de-lithiation reaction proceeded.

#### **3.2. Introduction**

Transition metal fluoride/carbon nanocomposites have been under extensive investigation in the recent years due to their theoretical high capacity in the range of 500 to 800 mAh/g [5, 18]. These electrode materials possess high capacity because their transition metals are reduced completely to their metallic state and transferring all their valence electrons [5, 6, 8, 11, 13, 14, 19]. In fluoride-based compounds with trivalent

---

<sup>2</sup> M. Sina, N. Pereira, G. G. Amatucci and F. Cosandey, “Amorphous phase formation, electron beam induced crystallization and stability upon cycling in delithiated FeOF nanocomposites” in prep (2014)

cations, the conversion and re-conversion reactions are complex and numerous studies have been performed in various systems such as  $\text{FeF}_3$  [8, 14, 21, 35],  $\text{BiF}_3$  [7, 11, 12] and the  $\text{FeOF}$  [13, 14, 31, 41, 42]. Among the iron fluorides systems,  $\text{FeOF}$  nanocomposite system show the most promise as a high capacity cathode material because of its higher capacity retention upon cycling and lowest intrinsic charge-discharge voltage hysteresis of 0.7 V (measured by reverse step PITT at  $C/1000$ ) as compared to 1.3 V for  $\text{FeF}_3$  and  $\text{FeF}_2$  [56]. This low hysteresis is due in part to a similar reaction mechanism associated with lithiation-delithiation of a (Li-Fe-O-F) rocksalt phase formed upon the transformation from the initial rutile ( $P4_2/mnm$ ) structure [13, 14, 31, 41, 42]. In addition, general observation from these studies by X-ray diffraction [14], PDF [41] and electron diffraction [31] is a reduction in crystallinity and that the original rutile structure is not reversible but delithiation leads to a complex multiphase microstructure [31, 41] consisting of a (Li-Fe-O-F) rocksalt and an amorphous phase with rutile type short range order.

In the course of our initial STEM/EELS and electron diffraction investigation, we also observed that the amorphous phase crystalizes under the electron beam [31]. It is now well documented that the electron beam can lead to irradiation effects such as heating, electrostatic charging, ionization (radiolysis), and Knock-on displacement (atomic displacement) [57]. These irradiation effects are generally associated with material degradation such as decomposition and material loss by sputtering.

The two principal irradiation mechanisms are knock-on displacement and ionization damage. Knock-on displacement originates from interaction of elastic scattering with the nucleus of the atom, which can displace the atoms to interstitial

positions or to sputtering of surface atoms. Knock-on displacement occurs when the incident electron energy is higher than the displacement energy and is dependent on material characteristics such as atomic number and bond strength [57-59]. There exists also a threshold energy below which knock-on displacement does not occur, which is dependent on atomic number. Ionization damage occurs through inelastic scattering and for inorganic materials, is found to occur primarily in oxides, and halides. This phenomenon, called radiolysis, can occur in numerous systems at very low beam energies and lead to material decomposition followed by material loss. In particular, metal fluorides are known to dissociate under the electron beam and electron-beam dissociation has been studied in numerous systems such as  $\text{AlF}_3$  [49, 60, 61],  $\text{FeF}_2$  and  $\text{FeF}_3$  [35, 50],  $\text{LiF}$  [62] and  $\text{BaF}_2$ ,  $\text{LaF}_3$ ,  $\text{CsF}$ ,  $\text{SrF}_2$  [63].

Electron irradiation, however, is not always detrimental and under small electron dose it can promote a phase transition from non-equilibrium to equilibrium states, such as a transition from amorphous to crystalline states. This transition from amorphous to crystalline states occurs when electron irradiation by knock-on displacement provides sufficient atomic displacement to move the atoms into their stable crystalline configuration, which corresponds to a net decrease in Gibbs free energy [64-66]. The driving force for crystallization is the difference in Gibbs free energy between the amorphous and crystalline states, which is illustrated in Figure 3-1. Such a transition is similar to the process occurring by annealing [59, 67-70] at high temperatures more than half the melting point ( $> T_M/2$ ) while beam-induced crystallization occurs without any local beam heating [65, 66, 68, 70, 71]. Several studies have shown that electron beam induced crystallization is a general phenomenon and can occur in a wide range of



amorphous materials such as Si [58],  $\text{ZrO}_2$  [72],  $\text{MgAl}_2\text{O}_4$  [73],  $\text{FeF}_3$  [50] and metallic glasses [64, 65, 74]. For instance, using EELS, Saifullah et al. found that under the influence of the electron beam, amorphous  $\text{FeF}_3$  film rearrange their randomly distributed  $\text{FeF}_6$  octahedra to form first crystalline  $\text{FeF}_2$  followed by  $\text{FeF}_3$  [50].

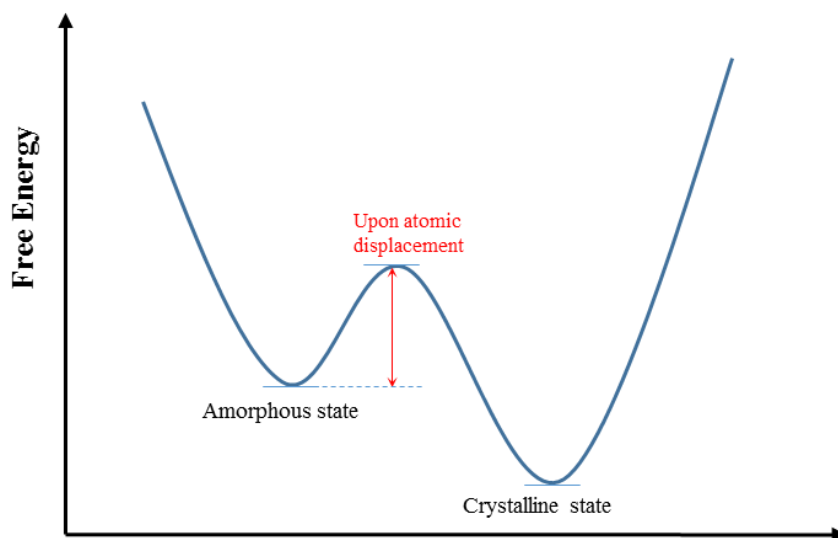


Figure 3-1 Schematic diagram of free energy differences between amorphous and crystalline states. The electron beam increases the free energy of the amorphous phase to overcome the energy barrier.

In the present work, we have used the formation of long-range order induced by electron beam irradiation to study the metastability of phases formed during delithiation of  $\text{FeO}_{0.7}\text{F}_{1.3}/\text{C}$  nanocomposites. TEM experiments were conducted at 200 KeV under various electron doses ranging from 0 to  $780 \text{ C/cm}^2$  ( $4.89 \times 10^7 \text{ e/nm}^2$ ). Electron energy loss spectroscopy was also performed to follow electron beam induced chemical changes such as F loss that can occur upon electron irradiation. Using this methodology of

electron beam induced crystallization, we have also followed the effect of electrochemical cycling on formation and stability of metastable phases.

### **3.3. Experimental**

#### **3.3.1. Materials synthesis**

The nanostructured iron oxyfluoride were synthesized by a solution process from reacting iron metal with fluorosilicic acid aqueous solutions ( $\text{H}_2\text{SiF}_6$ ). In this process a mixture of dissolved iron metal in a 20-25 wt % fluorosilicic acid heated at 40-45°C for 12 hours, and then heated at 110°C until the dry powder ( $\text{FeSiF}_6 \cdot 6\text{H}_2\text{O}$ ) is formed. After formation of  $\text{FeSiF}_6 \cdot 6\text{H}_2\text{O}$  powder it was annealed (150-300°C) under controlled atmosphere or in air to form  $\text{FeO}_{0.7}\text{F}_{0.3}$ . The  $\text{FeO}_{0.7}\text{F}_{0.3}/\text{C}$  nano-composite was prepared by high-energy ball milling with 15 wt% activated carbon black (Asupra, Norit) for 1 hour under helium atmosphere. Further details can be found in the original paper by Pereira et al [14].

#### **3.3.2. Electrochemistry**

For electrochemical testing, coin cells were assembled in a He-filled dry box using glass fiber separators saturated with 1 M  $\text{LiPF}_6$  in ethylene carbonate:dimethyl carbonate (EC/DMC) electrolyte (Ferro). The cells were tested versus lithium metal (Maccor) in galvanostatic mode. The cells were cycled under a constant current of 50 mA/g between 1.5 and 4.5 V at 60°C (Pereira, Badway et al. 2009).

### 3.3.3. TEM analysis

The cycled cells were disassembled in a He glove box and the  $\text{FeO}_{0.7}\text{F}_{0.3}/\text{C}$  electrode material was extracted in powder form. The powder was then dispersed in DMC, and a small droplet of the dispersion was cast on a lacy carbon grid and then transferred into the TEM under controlled atmosphere with a vacuum transfer TEM holder (Gatan).

Selected area electron diffraction (SAED) patterns and EELS spectra were obtained with a JEOL 2010F microscope at 197 kV equipped with a Gatan Image Filter (GIF-200) spectrometer. The energy resolution was 0.9 eV with EELS data obtained using a collection angle ( $\beta$ ) of 27 mrad and convergence angle ( $\alpha$ ) of 10 mrad.

The uniformly irradiated area was obtained in TEM mode by over focusing the condenser lens. The SAED patterns and EELS spectra were each recorded as a function of time at a dose rate of  $1.42 \text{ C/cm}^2/\text{s}$ . Total doses from 20 to  $780 \text{ C/cm}^2$  were used in this study. Radially averaged diffraction patterns were quantified using Process Diffraction in order to obtain diffraction pattern intensity profiles [22].

## 3.4. Results

### 3.4.1. Phase transformation during lithiation and delithiation of $\text{FeO}_{0.7}\text{F}_{1.3}/\text{C}$

Structural characterizations were performed by electron diffraction (SAED) on lithiated and delithiated  $\text{FeO}_{0.7}\text{F}_{1.3}/\text{C}$  nanocomposite samples with various lithium contents. The SAED pattern of the initial  $\text{FeO}_{0.7}\text{F}_{1.3}/\text{C}$  (Figure 3-2(a)) confirms the existence of crystalline rutile structure (space group  $\text{P4}_2/\text{mnm}$ ). Upon lithiation with 1.68 Li (1.5 V), SAED pattern is consistent with the formation of (Li-Fe-O-F) lithiated cubic

rocksalt phases and metallic iron (Figure 3-2(b)) as noted in previous investigations [13, 14, 31]. The formation of an intermediate rocksalt type phase is not unique for rutile FeOF as a similar result has been reported by Vijayakumar et al. [75] for rutile  $\text{TiO}_2$ . In that paper, electron diffraction measurements indicated that lithiated  $\text{Li}_x\text{TiO}_2$  transformed to spinel followed by rocksalt structures at  $x = 0.46$  and  $x = 0.88$  Li contents, respectively. Despite the overlap of the reflections from LiF, (Li-Fe-O-F) rocksalt and Fe phases, it is possible to determine the presence of LiF by the appearance of an extra (311) reflection at 0.121 nm. In this study, the presence of LiF has been confirmed from EELS experiments; however, it has not been detected in the diffraction patterns. This could be due to the extremely fine particle size or amorphous structure as observed in other experimental [6] and recent molecular dynamic studies [47] revealing first the formation of amorphous LiF followed by crystallization. Recently, it has been postulated that LiF is present in the solid electrolyte interphase (SEI) layer but that only Fe and (Li-Fe-O-F) rocksalt are formed from the lithiation, which are subsequent conversion from rutile  $\text{FeO}_{0.7}\text{F}_{1.3}$  [56].

Upon full delithiation to 4.5V with residual Li content of 0.18, the diffracted reflections are more diffuse but still reveal rocksalt-type reflections with an additional strong diffuse ring at 0.254 nm. Surprisingly the initial rutile structure is not present after fully delithiation. The change in relative intensities of the reflection at 0.206 nm and 0.146 nm between 1.42 Li (Figure 3-2(c)) and 0.18 Li (Figure 3-2(d)) is caused by the disappearance of Fe nanoparticles. The evolution of electron diffraction intensity profiles of the delithiated samples is shown in more details in Figure 3-3. From 1.68 to 1.02 Li,

the intensity profile corresponds to the superposition of rocksalt-type structure and Fe (reflections  $I_1, I_2$ ).

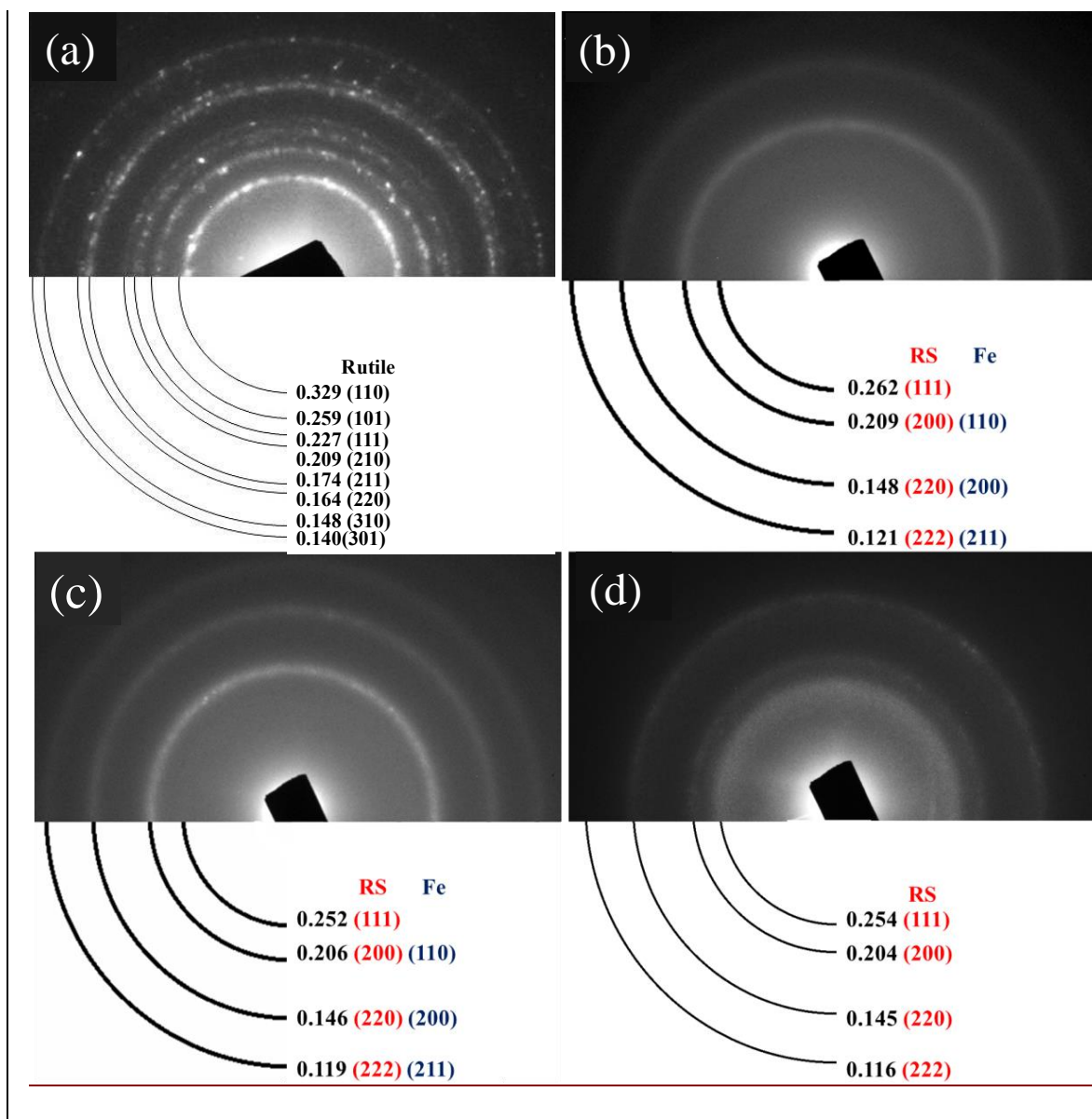


Figure 3-2 SAED pattern of  $\text{FeO}_{0.7}\text{F}_{1.3}/\text{C}$  as a function of Li content with a) initial  $\text{FeO}_{0.7}\text{F}_{1.3}/\text{C}$ , b)  $\text{FeO}_{0.7}\text{F}_{1.3}/\text{C}$  lithiated with 1.6 Li, c) delithiated  $\text{FeO}_{0.7}\text{F}_{1.3}/\text{C}$  with 1.42 Li, b) fully delithiated  $\text{FeO}_{0.7}\text{F}_{1.3}/\text{C}$  with 0.18 Li.

A new broad peak marked  $I_R$  and a broad shoulder marked  $I_S$  start to appear. Both of these peaks become stronger and broader with decreasing Li content, whereas the

rocksalt reflections ( $I_1$ , and  $I_2$ ) remain in the same positions with their intensities decreasing gradually with decreasing Li content. The  $I_S$  and  $I_R$  peak intensities are most likely associated with the formation of a disordered phase with short-range order. The steady decrease of  $I_1/I_2$  intensity ratio between 1.68 to 0.69 Li is associated with decreasing concentration of metallic iron, because the  $I_1/I_2$  intensity ratio is four times larger for metallic iron than for the intermediate rocksalt phase. At 0.69 Li, Fe nanoparticles are no longer observed by ADF-STEM imaging and the phases present are mostly rocksalt and an amorphous phase [31].

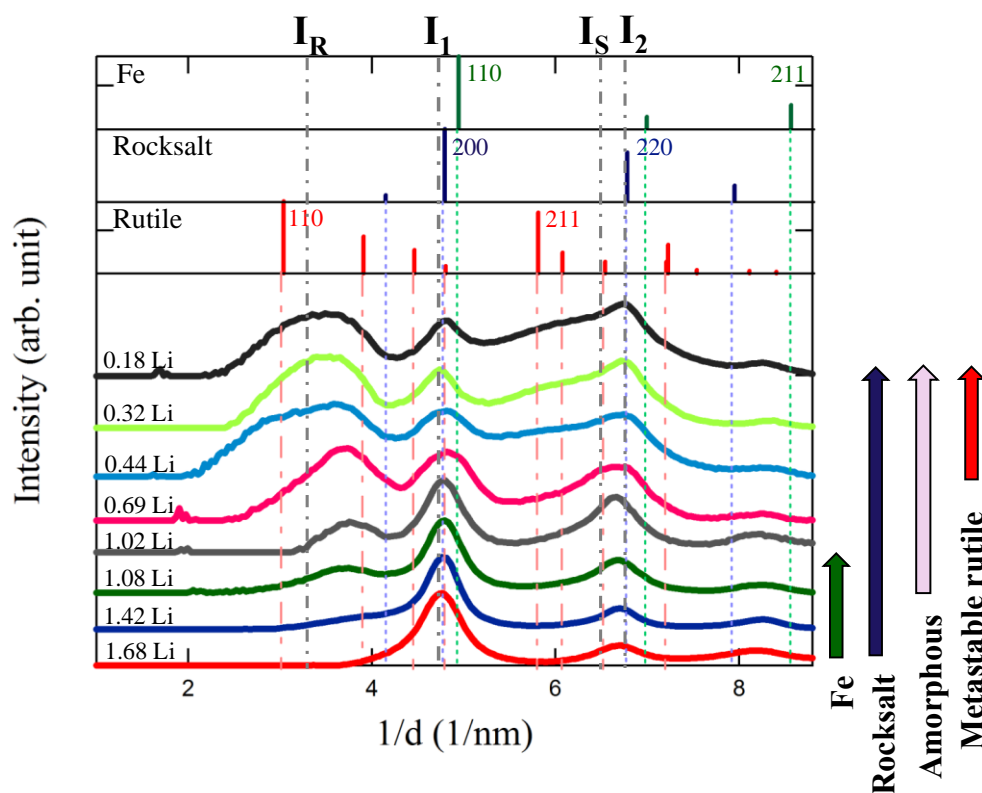


Figure 3-3 SAED intensity profiles of delithiated  $\text{FeO}_{0.7}\text{F}_{1.3}/\text{C}$  electrode as a function of Li content. The reflections marked  $I_1$ ,  $I_2$  and  $I_3$  correspond to the cubic rutile phase with also metallic Fe below 0.69 Li while reflections marked  $I_R$  and  $I_S$  correspond to amorphous type structure

### 3.4.2. Effect of electron beam irradiation

As mentioned in the introduction, electron beam irradiation can induce crystallization of metastable amorphous materials at low electron dose [59, 67-69, 71]. To determine the stable equilibrium structure of the delithiated sample at various Li stoichiometries, we performed a series of experiments with increasing electron dose from 20 C/cm<sup>2</sup> to 780 C/cm<sup>2</sup>. Figure 3-4(a) and Figure 3-4(b) shows SAED patterns of the delithiated samples with 1.42 Li and 0.18 Li, respectively, after an electron dose of 780 C/cm<sup>2</sup>. By comparing SAED patterns before (c.f. Figure 3-2(c) and Figure 3-2(d)) and after (c.f. Figure 3-3(a) and Figure 3-3(b)) electron beam irradiation, the recharge sample with 1.42 Li is stable under electron irradiation while transformation to rutile structure is observed for the fully delithiated sample (0.18 Li). For the 1.4 Li sample, Fe nanoparticles were still present while an amorphous phase was present in the 0.18 Li sample before irradiation (Figure 3-2(d)). The long range crystalline structure can be image directly by HRTEM as shown in Figure 3-4(c,d) the corresponding Fourier transform revealing diffraction periodicities corresponding to rutile

Figure 3-5 shows SAED intensity profiles of all delithiated FeO<sub>0.7</sub>F<sub>1.3</sub>/C samples ranging from 1.68 to 0.18 Li content obtained after an electron dose at 780 C/cm<sup>2</sup>. By comparison with Figure 3-3, electron beam irradiation does not affect the shape of the intensity profiles of the delithiated samples from 1.68 to 0.69 Li as their intensity profiles remain identical. This range in Li content corresponds to microstructures in which Fe nanoparticles are still present. However, electron beam irradiation induces a gradual crystalline rutile structure for 0.44 Li and lower Li content samples with a gradual increase in intensity of rutile type reflections.

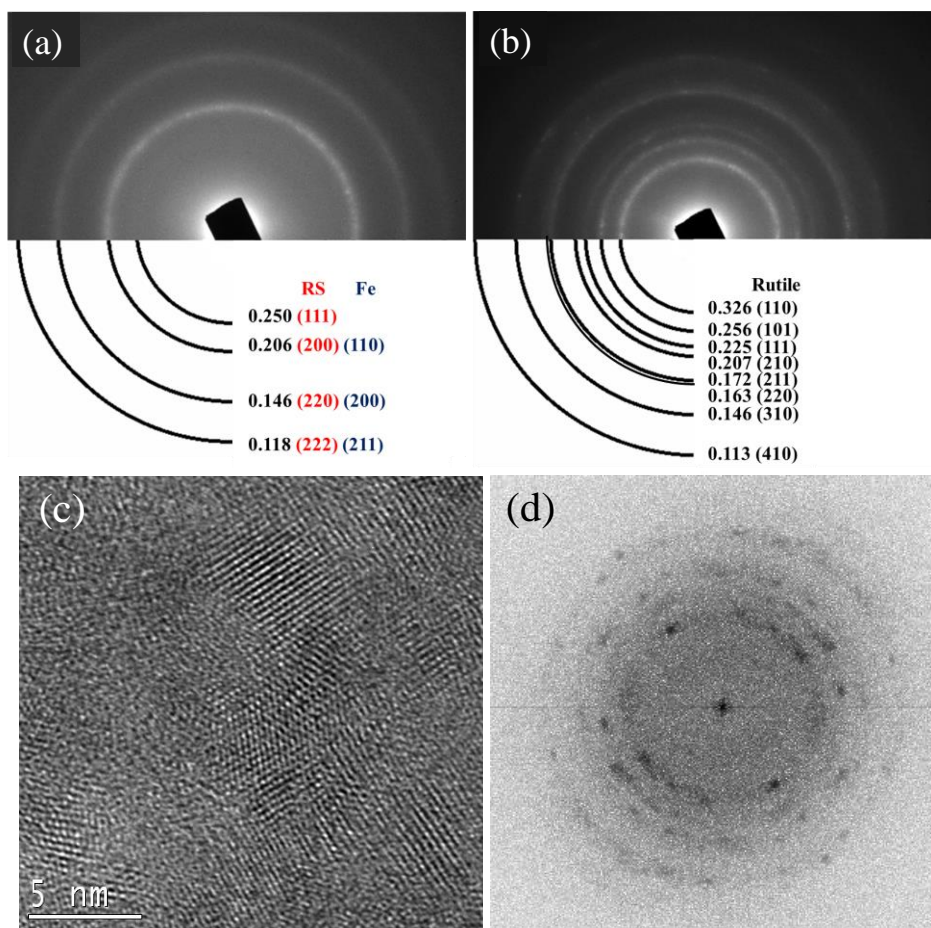


Figure 3-4 (a,b) SAED patterns of delithiated  $\text{FeO}_{0.7}\text{F}_{1.3}/\text{C}$  electrode after electron irradiation with an electron dose of  $780 \text{ C}/\text{cm}^2$  with (a) 1.4 Li and (b) fully delithiated (0.18 Li) revealing a transformation to crystalline rutile for the fully de-lithiated electrode. (c) HRTEM image of recrystallized delithiated sample with (d) corresponding Fourier transform (FFT).



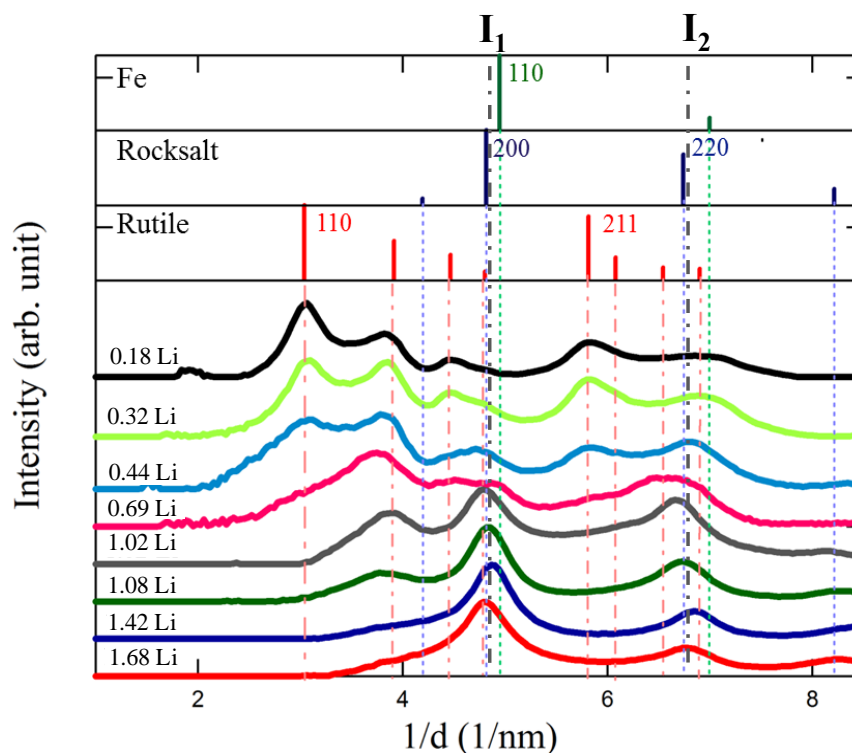


Figure 3-5 SAED intensity profiles of delithiated  $\text{FeO}_{0.7}\text{F}_{1.3}/\text{C}$  electrode for various Li content after an electron dose  $780 \text{ C}/\text{cm}^2$ . Electron irradiation induced amorphous to crystalline transition occurs for Li content below 0.69 Li.

This phenomenon is visible from the apparition of the strongest (110) and (211) rutile reflection at 0.329 nm and 0.172 nm respectively (Figure 3-5). These results imply that delithiated samples with 0.44 Li and below contain a metastable amorphous-nanocrystalline microstructure and consequently, transform back to crystalline rutile structure upon electron beam irradiation. In addition, crystallization in the fully delithiated sample (0.18 Li) is fastest and requires a lower electron dose ( $270 \text{ C}/\text{cm}^2$ ) compared to crystallization of the 0.44 Li or 0.32 Li samples which are requiring 550 and  $780 \text{ C}/\text{cm}^2$  respectively (see supplemental information Figure 3-6-S)

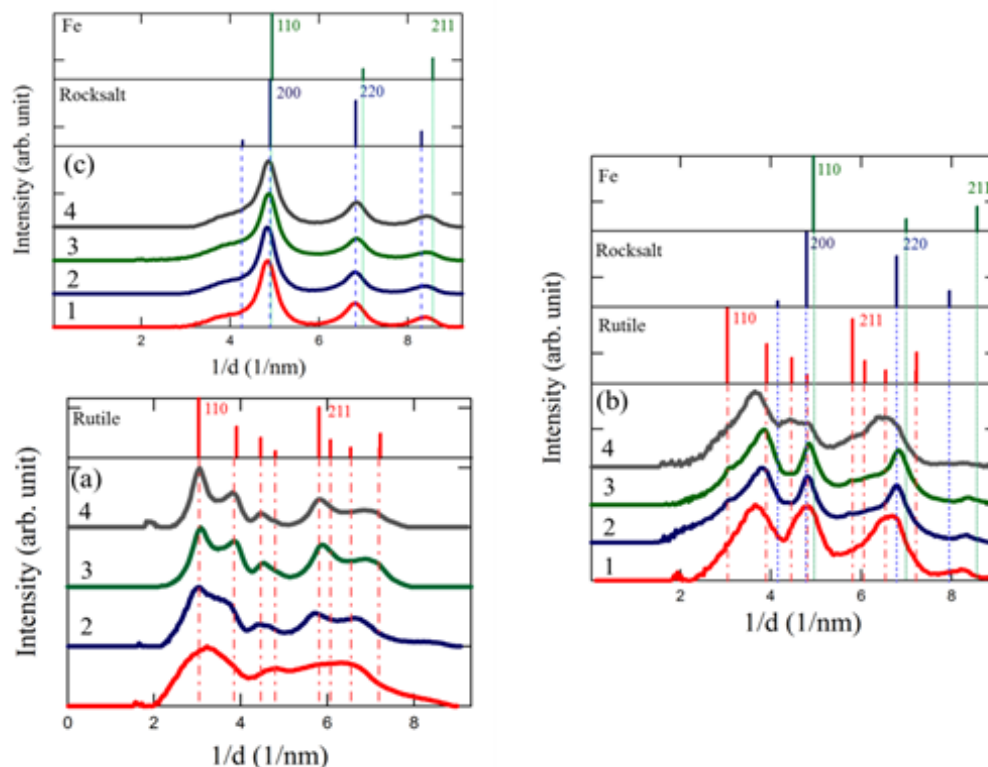


Figure 3-6-S Changes in SAED intensity profiles of  $\text{FeO}_{0.7}\text{F}_{1.3}/\text{C}$  recharged with (a) 1.42 Li, b) 0.69 Li, and (c) 0.18 Li as a function of electron beam dose corresponding to (1)  $20 \text{ C/cm}^2$ , (2)  $270 \text{ C/cm}^2$ , (3)  $550 \text{ C/cm}^2$  and (4)  $780 \text{ C/cm}^2$ .

Electron beam irradiation can cause beam induced irreversible damage. Fluorine compounds, in particular, are electron beam sensitive and are known to decompose by ionization followed by fluorine loss. Hence, EELS was used to track chemical changes occurring under electron beam irradiation. Electron energy loss spectra were collected as a function of electron dose from recharged  $\text{FeO}_{0.7}\text{F}_{1.3}/\text{C}$  with 1.08 Li and 0.18 Li and results are shown in Figure 3-7. In this Figure, the chemistry of the material as a function of electron dose is expressed as F over Fe EELS intensity ratio. It can be seen that this intensity ratio decreased gradually as the electron dose increased to the maximum of  $7,500 \text{ C/cm}^2$ . The maximum electron dose of  $780 \text{ C/cm}^2$  used in our SAED pattern

experiments, which is also marked in Figure 3-7. The differences in F loss between the two delithiated samples (1.08 Li and 0.18 Li) are due to the existence of different fluorine compounds in the two samples. The fully delithiated sample comprises  $\text{FeO}_{0.7}\text{F}_{1.3}$  compound with rocksalt-amorphous rutile phases, whereas three phases coexist in the 1.08 Li sample corresponding to (Li-Fe-O-F) rocksalt, Fe and possibly LiF phases. The increase of F loss could be attributed to higher electron beam sensitivity of LiF as compared to other two F containing phases (Li-Fe-O-F rocksalt and amorphous  $\text{FeO}_{0.7}\text{F}_{1.3}$ ). From Figure 3-7 fluorine intensity losses of about 8% and 27% can be estimated at 7000  $\text{C}/\text{cm}^2$  electron irradiation dose for the delithiated samples with 1.08 Li and 0.18 Li, respectively. However, a maximum F loss of 1 % is calculated for the maximum does of 780  $\text{C}/\text{cm}^2$  of our SAED experiments. This result indicates that the samples did not suffer any significant F loss during the electron beam recrystallization experiment which could possibly have an impact on phase stability.

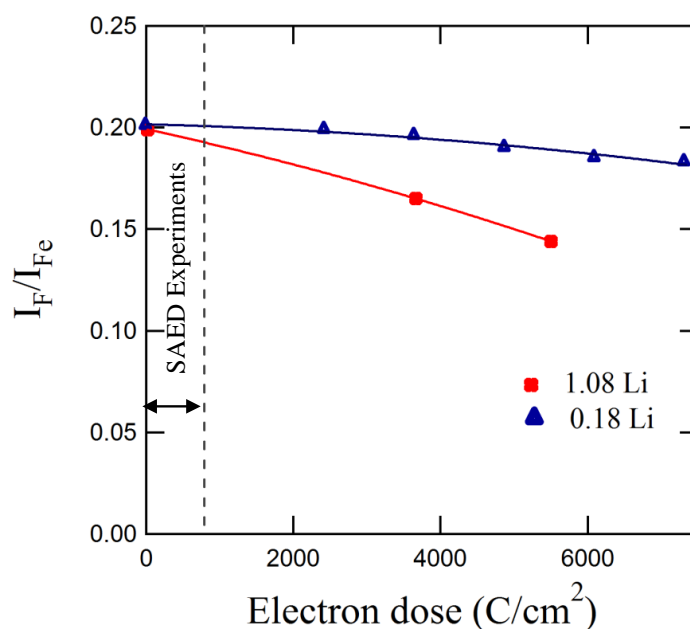


Figure 3-7 F-K over Fe-L EELS intensity ratio ( $I_F/I_O$ ) as a function of electron dose for delithiated  $\text{FeO}_{0.7}\text{F}_{1.3}/\text{C}$  with 1.08 Li and 0.18 Li.

### 3.4.3. Effect of cycling on phase transformation and stability

We also studied the structural changes of the delithiated samples as a function of cycle numbers. Figure 3-8 shows the electrochemical behavior for  $\text{FeO}_{0.7}\text{F}_{1.3}/\text{C}$  at a rate of 50 mA/g at 60°C. The capacity remains constant at about 330 mAh/g up to 20 cycles after which it drops to approximately 80 mAh/g at 60 cycles.

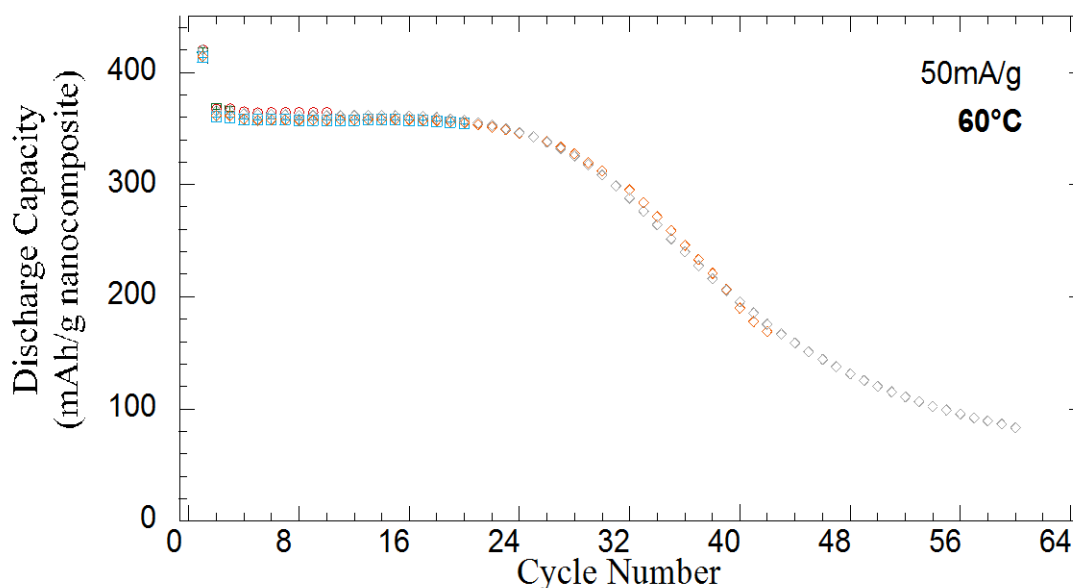


Figure 3-8 Discharged capacity as a function of cycle number for  $\text{FeO}_{0.7}\text{F}_{1.3}/\text{C}$  cathode cycled at a rate of 50 mA/g at 60 °C.

The SAED pattern of the delithiated sample after 3 cycles (Figure 3-9(a)) contains diffuse rings corresponding to the presence of amorphous phase and rocksalt-type phase; however, strong rings are observed for the delithiated sample after 60 cycles (Figure 3-9(b)) associated with crystalline LiF and metallic iron. The corresponding SAED

intensity profiles of delithiated  $\text{FeO}_{0.7}\text{F}_{1.3}/\text{C}$  after various numbers of cycles are shown in Figure 3-10(a). After one cycle, the microstructure of the fully delithiated sample consists of a mixture of rocksalt-type and amorphous (rutile-type) phases. From Figure 3-10(a), the  $I_1$  and  $I_2$  reflections become more intense, whereas the amorphous reflections ( $I_R$  and  $I_S$ ) decreased in intensity after cycling. The amorphous reflections ( $I_R$  and  $I_S$ ) are almost nonexistent at 40 cycled. The sharp diffraction spots with individual spots now appearing in the SAED shown in Figure 3-9(b) are indicative of an increased particle size and crystallinity.

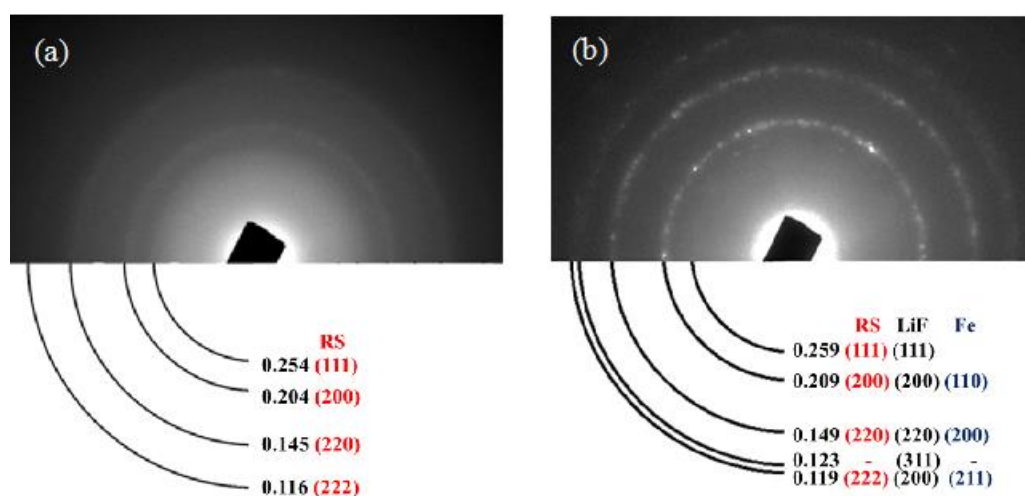


Figure 3-9 SAED pattern of delithiated  $\text{FeO}_{0.7}\text{F}_{1.3}/\text{C}$  after (b) 3 cycles, and (d) 60 cycles.

The evolution of the corresponding SAED intensity profiles after electron exposure  $780 \text{ C/cm}^2$  is shown in Figure 3-10(b). The intensity profiles, which contain rocksalt and amorphous reflections ( $I_R$  and  $I_S$ ) recrystallized under an electron dose of  $780 \text{ C/cm}^2$  to a rutile-type structure.

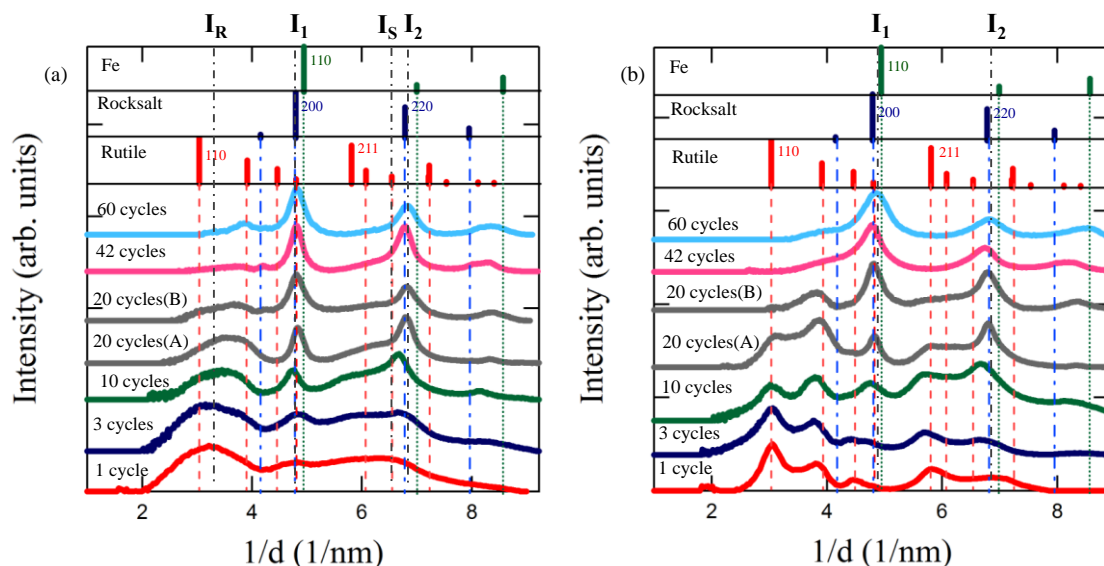


Figure 3-10 SAED intensity profiles of cycled delithiated  $\text{FeO}_{0.7}\text{F}_{1.3}/\text{C}$  as a function of number of cycles (a) before and (b) after electron irradiation with an electron dose of  $780 \text{ C/cm}^2$

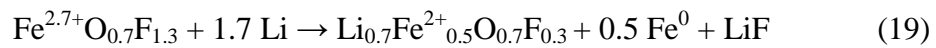
This is observed from the appearance of the most intense (110) and (211) reflections of  $\text{P4}_2/\text{mmn}$  rutile structure. The recrystallization to rutile-type structure decreased as the number of cycles increased. The delithiated-cycled samples after 42 cycles and higher only comprise cubic reflections ( $I_1$  and  $I_2$ ) that are associated with the presence of rocksalt-type, Fe phases and crystalline LiF (Cf Figure 3-9(b)). These phases (rocksalt-type, LiF and Fe) are the same converted products observed at lithiation to 1.5V, which did not reconverted back to the metastable amorphous-rocksalt phase mixture formed upon delithiation. Several phenomena can lead to this incomplete reversion upon. First, electrochemical disconnection can isolate and aggregate the active phases leading to isolation. In addition, possible aggregation can also be associated would lead to a lack of the interconnectivity of the various phases at the nano level required for reversion. Finally, the increase in the SEI layer thickness upon cycling

can become deleterious to the reconversion process. Indeed, the SEI layer, which is composed of insulating inorganic and organic materials (LiF and  $\text{Li}_2\text{CO}_3$ ), can reduce the  $\text{Li}^+$  transfer from the electrolyte into the active electrode leading to incomplete reconversion [12].

### 3.5. Discussion

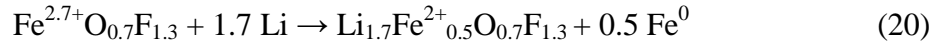
The results of this investigation show that after first delithiation, the initial rutile phase does not reform but instead the new microstructure is composed of a mixture of two phase consisting of a rocksalt-type phase and an amorphous phase[41]. These two phases are intimately mixed and upon low dose electron irradiation recrystallize into a stable rutile structure similar to the initial  $\text{P4}_2/\text{mm}$  structure. Upon second lithiation, the amorphous phase disappears, leaving a microstructure consisting of a lithiated (Li-Fe-O-F) rocksalt phase with Fe nanoparticles. The amorphous rutile-type phase re-appears upon delithiation suggesting an active participation in the lithiation-delithiation process. The exact composition of these phases is not known but it has been proposed that the rocksalt phase is oxygen rich while the amorphous phase is fluorine rich [31, 41]. The molar fraction of Fe in metallic form is 0.5.

Based on these results the following lithiation reaction has been proposed at lithiation:



In contrast to other fluoride systems ( $\text{FeF}_2$  and  $\text{FeFe}_3$ ), crystalline LiF has not been observed for FeOF. The presence of LiF has only been detected by EELS from the

presence of F post peak [31]. There is therefore the possibility that LiF remains associated with the rocksalt phase [56]:



Delithiation process occurs in two stages. During the first stage (from 1.68 Li up to 0.69 Li), Fe nanoparticles react with remaining LiF to form an amorphous  $\text{Fe}_x\text{Li}_{2-x}\text{F}_2$  phase with x possibly as high as 0.4-0.5. The existence of such a phase has been proposed recently as a transient phase during the delithiation process of  $\text{FeF}_2$  [56]. The second stage of delithiation (from 0.69 Li to 0), involves simultaneous Li removal from the two lithiated phases, the amorphous iron fluoride and rocksalt-type phases [31]. At full delithiation, the Fe phase fraction as determined by pair distribution function (PDF) is 30% for rocksalt phase with the remaining 70% for amorphous rutile phase. As the amorphous phase disappears at the end of next lithiation cycle, this is an indication that both phases play a role in the lithiation delithiation process.

The reconversion processes associated with transformation from cubic rocksalt to rutile phase requires a structural rearrangement of octahedral  $\text{FeO}_6$  with an expansion of the unit cell [50, 75]. This volume changes upon delithiation leads to strains of the cubic structure, which could be why this transformation is not occurring electrochemically. The formation of the initial crystalline rutile phase from rocksalt phase requires atomic rearrangement and diffusion, and such local atomic rearrangement and phase intermixing with long-range order (crystallization) can be achieved via electron beam irradiation [50, 75]. Figure 3-11 shows the atomic arrangements of rocksalt and rutile structure respectively, where in both structures Fe occupies octahedral interstitial surrounded with 6 anions. On the other hand, the Fe atoms form face-center-cubic and body-center-



tetragonal arrays in rocksalt and rutile structures respectively (Figure 3-11). Furthermore, in the lithiated phase with disordered-rocksalt structure, Li and Fe reside randomly in octahedral sites with an FCC oxygen and fluorine environment. The rutile structure, which is stabilized after atomic rearrangement induced by the electron beam, consists of Fe octahedral ( $\text{Fe}(\text{OF})_6$ ) environment (Chevrier, Hautier et al. 2013). These octahedral rearrangements from rocksalt to rutile structure requires considerable volume change and structural transformation, which causes a unit cell volume change of 8.2%. Thus it is not favorable electrochemically and led to the formation of an amorphous phase with only short-range order.

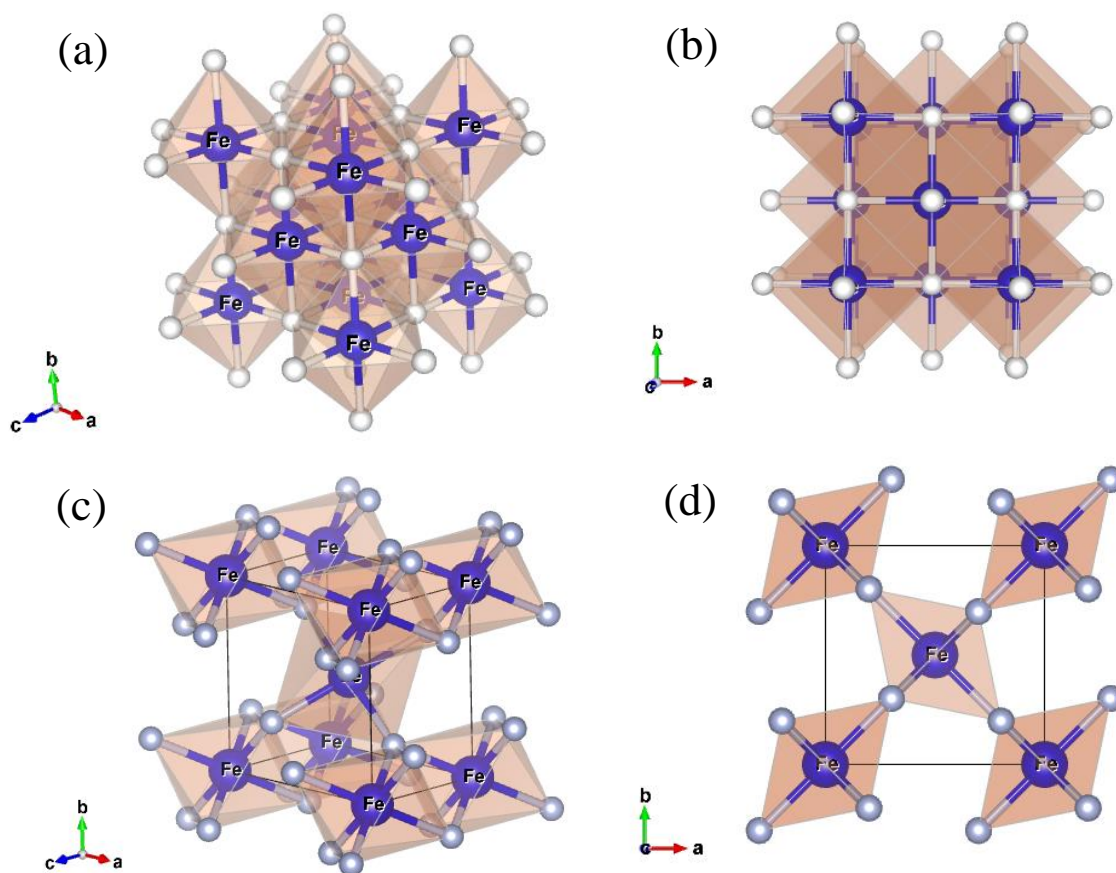


Figure 3-11 (a,b) Rocksalt crystal unit cell and (c,d) Rutile crystal structure, showing the octahedral arrangements ( $\text{Fe}(\text{OF})_6$ ) in rocksalt and rutile unit cells

It is now well established that knock-on displacement of atoms induces density fluctuation and increases atomic mobility, which leads to crystallization of an amorphous phase. The combined atomic displacement and increase local free volume provide the energy for long range ordering at room temperature. Three basic steps are necessary for the occurrence of crystallization [66, 74];

(1) Enhancement in the free energy of an amorphous phase as a result of defect formation (i.e. density fluctuation in the amorphous phase which is similar to vacancy and interstitial formation in crystalline materials), (2) radiation accelerated diffusion and local atomic ordering, and (3) nucleation of crystalline cluster.

Displacement energy ( $E_d$ ) is the minimum amount of energy required to permanently displace atoms from their original lattice sites to the defect positions. The electron beam energy transfers ( $E_E$ ) to atoms should be higher than displacement energy ( $E_d$ ) to enable the electron beam to displace the atoms and create point defects. Displacement energy is based on bonding type and the atomic mass of materials, which is generally about 5 to 50 eV. Several experiments have been done to determine the displacement energy for different materials [28, 57, 76-78].

Although much work has been done to calculate  $E_d$  for different materials,  $E_d$  of FeOF has not been determined yet. It has been elaborated that [28, 57] at 200 KeV, about 9 eV can be transferred to Fe, 33 eV to O, 29 eV to F and 75 eV to Li, although less amount of energy will be transferred to bonded atoms in a crystal such as FeOF. If we assume a minimum displacement energy of approximately 25 eV, hence at 200 KeV

electron beam is unlikely to displace Fe atom, but it is sufficient enough to displace F, O, and Li atoms. Nevertheless, long range diffusion of Fe is not necessary for this type of transformation. If we consider only Fe atoms in the rocksalt and rutile unit cells, Fe forms face center cubic (FCC) and body centered tetragonal BCT sub-lattices respectively. Figure 3-12 shows how the transformation from FCC to BCT can be obtained, without displacing the Fe atoms, which is called Bain transformation [79]. Only some local lattice strain will be required to accommodate a rocksalt to rutile transformation. If Fe nanoparticles are present in the microstructure, the 200 kV electron beam will not have the sufficient energy to displace the Fe atoms and create a new stable microstructure.

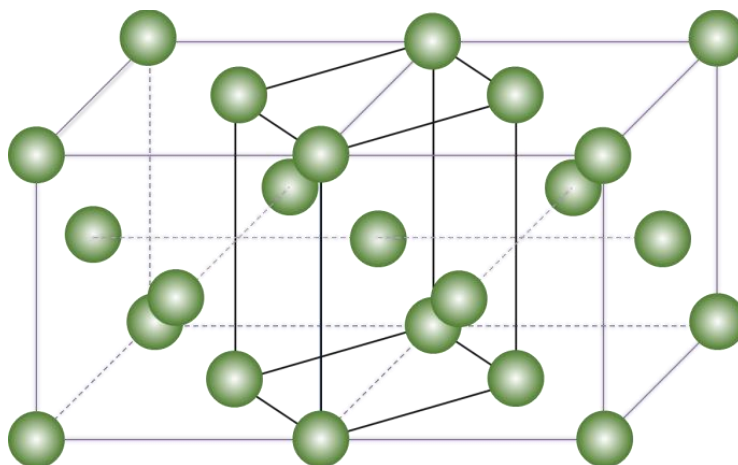


Figure 3-12 Schematic diagram depicting the diffusionless transformation and relation between FCC and BCT structures. Such a transformation can be occurring between rocksalt to rutile as the Fe sub-lattice from the rocksalt and rutile structures form FCC and BCT lattices respectively.

The possibility of transformation from rocksalt/amorphous nanocomposite crystalline rutile Fe-O-F phase is also correlated with the amount of delithiation. As delithiation reactions proceed from 0.44 to 0.18 Li, a lower electron dose is required for

full crystallization as reflections associated with (Li-Fe-O-F) rocksalt phase are still present for 0.44 Li while they have completely disappeared at full delithiation (0.18 Li). As delithiation proceed, from 0.44 to 0.28 Li the energy barrier from amorphous to crystalline rutile phase decreases, consequently requiring less energy to reach full crystallization.

### 3.6. Conclusion:

In this study, we investigated reconversion mechanisms and reversibility of  $\text{FeO}_{0.7}\text{F}_{1.3}/\text{C}$  nanocomposite electrode with the effects of electron irradiation on the structural changes. It was found that the amorphous rutile-type phase starts to form and increase during delithiation. This amorphous rutile-type phase recrystallized to the original rutile structure under low electron dose irradiation, which occurs by enhancing atomic displacement (knock-on effect). The energy difference between amorphous rocksalt phase and crystalline rutile phase is the driving force for the recrystallization. The total dose required for crystallization is dependent on amount of delithiation. As the delithiation reaction proceeds, crystallization occurs at lower electron irradiation dose.

After increasing number of cycles, the reconversion to the amorphous rutile-type phase decreased upon fully delithiation; however, the crystalline residual cubic phases (Fe, LiF, rocksalt-type phase) from the lithiated products appeared and increased. The appearance of the cubic phases (lithiated products) in the fully delithiated cycled samples resulting from the incomplete reconversion process and is associated to capacity loss upon cycling.

#### 4. On the role of cycling rate on phase formation in conversion $\text{FeF}_3/\text{C}$ cathode materials<sup>3</sup>

##### 4.1. Abstract

In this study, the structural transformation of the positive electrode  $\text{FeF}_3/\text{C}$  has been investigated as a function of cycling rate by combined STEM/EELS and electron diffraction (SEAD). The electrode was cycled under various constant current rates of 58.8 mA/g, 23.5mA/g and 8.8 mA/g at 60°C. As the cycling rate increases, the conversion process has been found to occur less uniformly. The SAED patterns taken for the fastest discharged rate of 58.8 mA/g revealed three different structures as a result of inhomogeneous lithiation process. Areas with the lowest lithium content contained a mixture of lithiated trigonal phase, lithiated rutile-type phase as well as LiF. Areas with higher lithium content are composed of a lithiated rutile type phase along with converted phases (LiF and  $\text{Fe}^0$ ). Fully recharged samples, cycled at 58.8 mA/g, reconverted to a mixture of trigonal and lithiated rutile-type structure. For the slowest cycling rate of 8.8 mAh/g complete conversion to Fe and LiF is observed upon discharge. Upon recharge, some regions converted back to the initial trigonal structure, while other regions transformed to a mixture of lithiated rutile-type and trigonal phases, and still other regions showing only rutile-type structure. The formation of these phases is dependent on the amount of remaining Li in the structure, with the initial trigonal (R-3c) phase appearing only in areas, which are completely delithiated.

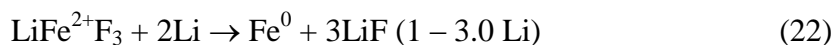
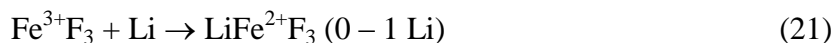
---

<sup>3</sup> M. Sina, N. Pereira, G. G. Amatucci and F. Cosandey, "On the role of cycling rate on phase formation in conversion  $\text{FeF}_3/\text{C}$  cathode materials" in prep (2014)

## 4.2. Introduction

During the last decade, metal fluoride nanocomposites have been studied extensively, as an alternative conversion positive electrode [7, 14, 19, 35, 37, 80, 81] because of their relative high conversion voltage of about 2V as compared to other conversion oxide or nitride materials. Of all metal fluorides, iron fluorides such as  $\text{FeF}_3$  have been of increasing interest due to their high theoretical capacity of 720 mAh/g, low cost, and low toxicity. However, the high ionicity of fluorides leads to poor electronic conductivity and therefore low electrochemical performance. For the first time, Arai et al. [82] have used iron trifluoride ( $\text{FeF}_3$ ) as a positive electrode in Li-ion batteries in 1997 and reported a capacity of 140 mAh/g for discharged  $\text{FeF}_3$  in the voltage range of 4.5 and 2 V. Later on Amatucci's group has reported the use of nanocomposite iron fluoride in a highly conductive carbon matrix in order to improve their electronic conductivity. They reported a high capacity of 540 mAh/g upon cycling between 4.5 and 1.5V [7, 8, 83].

The structural changes of a  $\text{FeF}_3$  cathode upon lithiation-delithiation have been studied by several groups and these studies reveal a two stage process upon discharge consisting of a first Li intercalation stage for 0 to 1 Li corresponding to the first  $\text{Fe}^{3+}$  to  $\text{Fe}^{2+}$  redox reaction followed by a second conversion stage from 1 to 3 Li corresponding to the transformation from  $\text{Fe}^{2+}$  to metallic  $\text{Fe}^0$  [7, 8, 21, 37, 40, 80, 84-86].



Details of the first lithiation cycle have been studied by Badway et al. [7] and Yamakawa et al. [21] using X-ray diffraction, GITT measurements, complementary

XRD, NMR, and PDF techniques. The results of these studies reveal that the lithiation between 0-1 Li is an insertion reaction, which contains two steps. The first stage of lithiation (0-0.58 Li) is a two-phase reaction, in which the initial trigonal  $\text{FeF}_3$  (R-3c) transforms to  $\text{Li}_{0.5}\text{FeF}_3$  (rutile-type) and then in the second stage,  $\text{Li}^+$  intercalates into  $\text{Li}_{0.5}\text{FeF}_3$  (0.58-1 Li) via a single-phase intercalation reaction with to form rutile-type  $\text{LiFeF}_3$ .

The second stage of lithiation (1- 3 Li) is accompanied with a conversion reaction in which  $\text{Fe}^0$ ,  $\text{LiF}$ , and lithium iron fluoride phases are formed. Upon delithiation, the original trigonal (R-3c) structure did not reform instead lithiated rutile-type phase is formed and its valence state increases upon delithiation, resulting in the formation of  $\text{Li}_{0.5}\text{FeF}_3$  (rutile-type structure) after delithiation (4.0 V) [7, 21].

Further experiments by STEM/EELS experiment on lithiated and delithiated  $\text{FeF}_3$  revealed a lower valence state for Fe closer to  $\text{Fe}^{2+}$  with rutile like structure [35]. The amount of possible residual Li was not reported in this study.

The phase evolution upon cycling has been studied theoretically by Doe et al. [40]. They predicted possible Li-Fe-F phases, using first-principal calculations. They reported that upon lithiation, intercalated  $\text{Li}_{1/4}\text{FeF}_3$  (trigonal structure) first formed followed by a transformation to a rutile-type phase and finally to the conversion phase ( $\text{LiF}$  and  $\text{Fe}$ ) upon further lithiation. Also, they predicted the formation of a defective tri-rutile phase with  $\text{Fe}^{3+}$  valence state upon full delithiation,.

Since then, the  $\text{FeF}_3/\text{C}$  conversion system has been studies extensively. The general two stage (intercalation followed by conversion) processes have been observed by different groups, but there is not yet a general consensus on phase formation. A

summary of published results with test conditions and phase formation after discharge and re-charge is presented in Table 1.

Based on TEM analysis, Li et al. [36] have shown that the discharged  $\text{FeF}_3$  at 1.5 V (RT and at 50mA/g cycling rate) contains the conversion phases (LiF and metallic Fe) along with unreacted  $\text{FeF}_2$  upon full lithiation, and defect-trirutile  $\text{FeF}_3$  phase is formed upon full delithiation. In addition, they reported that  $\text{FeF}_3$  loses its specific capacity from 543m mAh/g to 223 mAh/g after 50 cycles because of loss of active material ( $\text{FeF}_3$ ) upon cycling.

Table 4-1 Structural phase evolution after discharge and charge for cycled  $\text{FeF}_3/\text{C}$  obtained from different investigators

Group	Current rate	Temp.	Voltage (v)		Structure		Technique
[8]	7.58 mA/g	70°C	Discharge	1.5	Discharge	Fe + LiF	TEM (SAED-HRTEM)
			Charge	4.5	Charge	Rutile-type	
[21]	7.58 mA/g	25°C	Discharge	1	Discharge	Fe + LiF + Li- $\text{FeF}_2$ (rutile-type)	XRD-NMR-PDF
			Charge	4	Charge	Fe + LiF + Lithiated rutile	
[86]	100 mA/g	25°C	Discharge	0.8	Discharge	LiF + Fe + Li $\text{FeF}_3$ (R-3c)	XRD-XAFS
			Charge	4.5	Charge	Initial $\text{FeF}_3$	
[36]	50 mA/g	25°C	Discharge	1.5	Discharge	Fe + LiF + unreacted $\text{FeF}_2$	TEM (SAED-HRTEM)
			Charge	4.5	Charge	Defect trirutile $\text{FeF}_3$	
[85]	20 mA/g	25°C	Discharge	1.55	Discharge	LiF + Fe + Li $\text{FeF}_3$ (R-3c)	XRD
			Charge	4.5	Charge	Li $\text{FeF}_3$ (R-3c)	
[81]	61.5 mA/g	25°C	Discharge	1.0	Discharge	LiF + Fe	XRD
			Charge	4.5	Charge	$\text{FeF}_3$ (R-3c)	
[37]	100 mA/g	25°C	Discharge	1.0	Discharge	LiF + Fe	XRD
			Charge	4.5	Charge	$\text{FeF}_3$ (R-3c)	



In another study [86] on the evolution of  $\text{FeF}_3$ , which was cycled at 100 mA/g and at room temperature by ex-situ XRD and XAFS, they found that after full lithiation (with 2.78 Li- 0.8 V) the lithiated  $\text{FeF}_3$  phase still remained which is accompanied by the formation of LiF and Fe conversion phases. They showed that  $\text{FeF}_3$  is a reversible conversion material with initial  $\text{FeF}_3$  reformed after full delithiation (0.4 Li, 4.5 V). Also, the structural changes of  $\text{FeF}_3/\text{C}$ , which was cycled at 100 mA/g and 25°C were studied by ex-situ XRD (Li, Li et al. 2010). It was found that  $\text{FeF}_3/\text{C}$  converted into LiF and Fe at 1.0 V, and it reconverted back to  $\text{FeF}_3$  upon fully charged to 4.5 V. It was reported that  $\text{FeF}_3$  has a good cyclability at a very high cycle rates. (500 mA/g, 1000 mA/g, 2000 mA/g) [37]. Liu et. al. [81] reported that  $\text{Li}^+$  is inserted into  $\text{FeF}_3$  via a single-phase reaction up to 2.0 V and then it converted to LiF and Fe upon full discharge to 1.0 V. On the charge process, the electrode reconverted back to the initial  $\text{FeF}_3/\text{C}$  phase. They found that in the voltage range of 1.0 V-4.5 V cycling performance is poor, however, the cycling performance was improved in the voltage range of 2.0 V to 4.5 V when intercalation is the lithiation mechanism. Furthermore, they studied the effect of cycling rate on the capacity retention and found that as the cycling rate increased, the specific capacity decreased [81]. Myung et al. [85] with the use of ex-situ XRD have shown that intercalated  $\text{Li}_x\text{FeF}_3$  (R-3c) phase is formed during lithiation ( $\text{Li} = 0$  to 0.97), and upon further lithiation to 2.18 Li, the conversion phase (LiF and Fe) along with the lithiated phase  $\text{Li}_x\text{FeF}_3$  (R-3c) are formed. Upon charging, the fraction of LiF and Fe phases decreased along with the reduction in the lattice parameter of the lithiated  $\text{Li}_x\text{FeF}_3$  (R-3c) phase indicative of a de-intercalation process. The cycling performance of the electrode studied after different cycle number. It was also observed that the capacity dropped

significantly after 5 cycles which is due to extensive structural changes (from trigonal to cubic structure), as well as formation of LiF which decreased the electronic conductivity of the electrode during cycling [85].

All these experiments that have been done under different cycling conditions (temperature, current rate and initial particle size) revealed  $\text{FeF}_3$  lithiated and delithiated phases are not consistent. This is because of the high LiF molar fraction forming upon conversion, reaction kinetics are slower in  $\text{FeF}_3$  than for  $\text{FeF}_2$  [56] resulting in more inhomogeneous transformation.

In this this paper we studied the structural evolution of lithiated and delithiated  $\text{FeF}_3$  at various cycling rates using combined STEM/EELS and electron diffraction (SAED) techniques. We also presented structural evolution of  $\text{FeF}_3/\text{C}$  nanocomposite as a function of cycling number to gain a better understanding of capacity fading upon cycling.

### **4.3. Experimental**

#### **4.3.1. Nanocomposite synthesis**

The  $\text{FeF}_3/\text{C}$  nanocomposite was fabricated by the high energy milling a mixture of 85 wt%  $\text{FeF}_3$  (R-3c space group) and 15 wt % activated carbon (ASupra, Norit). The mixture of 85%  $\text{FeF}_3$  and 15% Carbon were loaded in a hardened steel milling cell along with hardened steel media and milled in a helium atmosphere for one hour [7, 8].

#### **4.3.2. Electrochemistry**

The positive electrode was prepared by mixing 57% active material and 12% carbon black without using binder (PVDF). Two electrode coin cells were assembled in a

helium glove box using a lithium foil as the anode, glass fiber separators, and a 1 M LiPF<sub>6</sub> in 1:1 ethylene carbonate:dimethyl carbonate (ED/DMC) electrolyte from Ferro. All of the electrochemical experiments were carried out at 60 °C under various currents of 58.8 mA/g, 23.5 mA/g, and 8.8 mA/g using a Maccor cycler [7].

#### **4.3.3. Transmission electron microscopy**

The cycled cells were disassembled in a helium-filled glove box and the positive electrode was rinsed in DMC. The FeF<sub>3</sub>/C electrode powder were then extracted from the electrode and dispersed in DMC followed by drop-casting onto a lacy carbon film supported on a copper grid. The TEM samples were then loaded on a vacuum transfer holder to avoid air exposure during transfer to the TEM. Selected area electron diffraction (SAED) pattern, annular dark field scanning transmission electron microscopy (ADF-STEM), and electron energy loss spectroscopy (EELS) were recorded at 197 KV in a JEOL-2010F microscope equipped with a Gatan imaging filter (GIF) spectrometer. The energy resolution of the EELS spectra measured from the full width at half magnitude (FWHM) of the zero-loss peak (ZLP) was 0.9 eV. Also, a collection angle ( $\beta$ ) of 20 mrad and a convergence angle ( $\alpha$ ) of 10 mrad were used for acquiring the EELS spectra. The Fe valence state was determined using the Fe L<sub>3</sub>/L<sub>2</sub> intensity ratio which was calibrated using FeO<sub>x</sub> and FeF<sub>x</sub> standards [13]. Reported values represent average values taken from 20 different EELS spectra.

Process Diffraction program was utilized for obtaining SAED intensity profiles by taking first rotational averages followed by background [23, 24]. In addition, JEMS software was used for simulating SAED intensity profile of nano-sized particles in the 2-

5 nm range by ab-initio calculation by determining the pair distribution function and then solving the Debye equation [44].

## 4.4. Results

### 4.4.1. Initial $\text{FeF}_3$ microstructure

Figure 4-1 (a) shows the diffraction pattern of the initial material. The pattern shows the existence of  $\text{FeF}_3$  with trigonal R-3c structure. The HRTEM image (Figure 4-1(b)) reveals the presence of  $\text{FeF}_3$  crystalline nano-particles with graphitic carbon. The initial particle size as measured by TEM dark field was 15 nm.

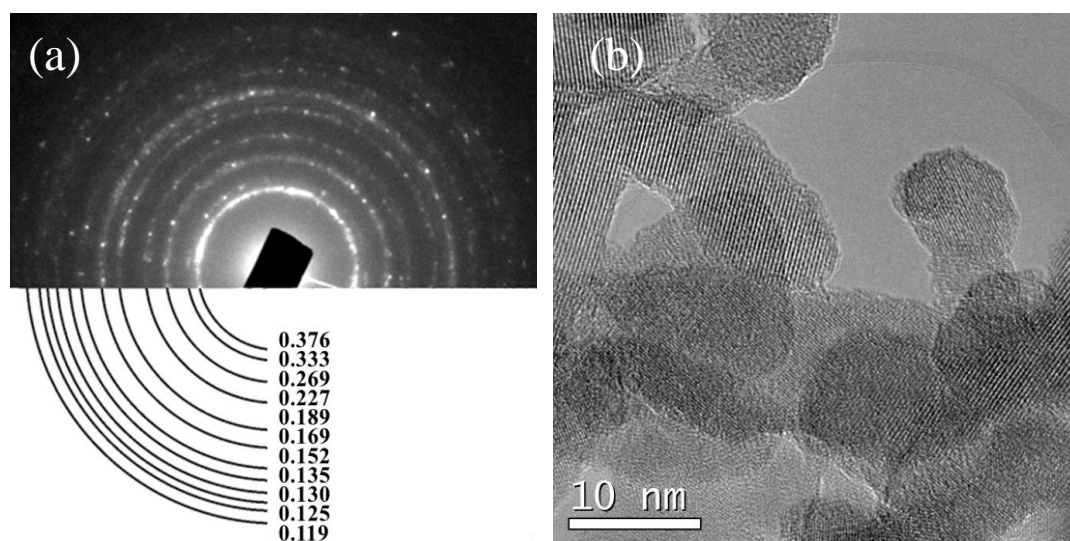


Figure 4-1 Initial  $\text{FeF}_3/\text{C}$  nanocomposite (a) SAED reveal the presence of R-3m  $\text{FeF}_3$  (b) HRTEM image showing the morphology of the crystalline  $\text{FeF}_3$  with average particle size of about 15 nm.

#### 4.4.2. Electrochemistry

The voltage profiles of the  $\text{FeF}_3/\text{C}$  nanocomposite cycled in galvanostatic mode at  $60^\circ\text{C}$  under various current rates (58.8, 23.5 and 8.8 mA/g) are shown in Figure 4-2(a). In the 3.5 to 2 V range, the voltage profiles obtained at various cycle rates have the same trend suggesting that they have similar electrochemical reaction mechanism. The voltage profile at 58.8 mA/g (Figure 4-2(a)) first shows that lithium insertion starts at 3.3 V, which is followed by a plateau-like region with a specific capacity of 100 mAh/g. This plateau region is attributed to a two-phase reaction involving reduction of  $\text{Fe}^{3+}$  to  $\text{Fe}^{2+}$  and formation of a  $\text{Li}_{0.5}\text{FeF}_3$  rutile-type phase. At 2.8 V, from  $\text{Li} = 0.5$  to 1, a solid solution insertion reaction ( $\text{LiFeF}_3$ ) proceeds, with the resulting specific capacity of 210 mAh/g. Upon further lithiation, the conversion reaction in the second region starts with the plateau region from about 2 to 1.5 V, which is accompanied by the formation of LiF and Fe phases [7, 21].

The discharge capacity of  $\text{FeF}_3$  at 1.5V cut off voltage is about 580 mA/g at  $60^\circ\text{C}$  under constant current of 58.8 mA/g and for rates of 23.5 mA/g and 8.8 mA/g the capacity increased to about 620 mAh/g and 660 mAh/g respectively. The corresponding Li content at the rates of 58.8 mA/g, 23.5 mA/g and 8.8 mA/g were 2.44, 2.59 and 2.75 Li respectively. The second redox plateau is observed at about 1.8 V for the sample cycled under 58.8 mA/g and increases to 2V as the cycling rate decreases to 8.8 mA/g.

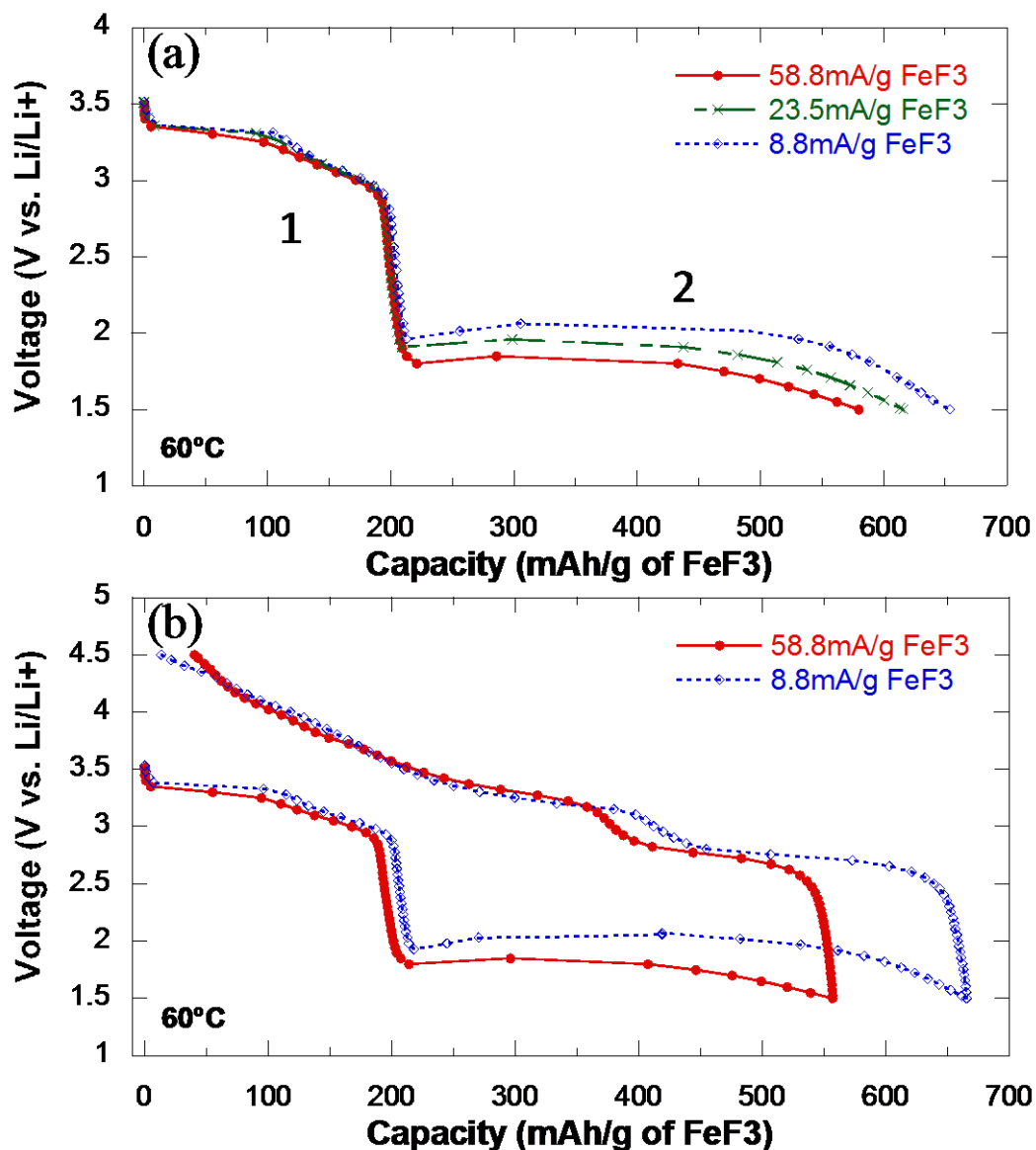


Figure 4-2 (a) Discharge voltage profile curves for the first cycle of the FeF<sub>3</sub>/C nanocomposite electrode under 58.8 mA/g, 23.5 mA/g, and 8.8 mA/g, (b) Voltage profiles for the first discharge-charge cycle under different currents of 58.8 mA/g and 8.8 mA/g.

It is significant to note that the lithiation rate does not affect the intercalation process and specific capacity of the electrode remains constant (about 210 mAh/g) under the various cycling rates (58.8 mA/g, 23.5 mA/g and 8.8 mA/g). However, the specific

capacity decreases as the cycling rate increases (Figure 4-2(a)). Figure 4-2(b) shows discharge-charge voltage profile curves for the samples cycled at rates of 58.8 mA/g and 8.8 mA/g. The delithiation process for both samples which were cycled at 58.8 mA/g and 8.8 mA/g was composed of two plateau regions at 2.7 V and 3.3 V, that corresponds to the oxidation of  $\text{Fe}^0$  to  $\text{Fe}^{2+}$  and  $\text{Fe}^{2+}$  to  $\text{Fe}^{3+}$  respectively [56]. It can be observed that between 1.5 and 2.5 V, which is associated with the reconversion process, the two curves (58.8 and 8.8 mA/g) are different. Also, the reaction hysteresis for  $\text{FeF}_3$  cycled at 58.8 mA/g and 8.8 mA/g measured at a capacity of 290 mAh/g are 1.55 V and 1.2 V respectively. The residual Li content at 4.5 V is also rate dependent which are 0.06 and 0.31 Li for recharge rates of 8.8 and 58.8 mAh/g respectively. We have also performed similar slow (8.8 mA/g) and fast (58.8 mA/g) recharge experiments after the same slow rate of discharge of 8.8 mAh/g and similar residual Li contents of about 0.3 Li have been measured. This results indicates that the residual Li content is dependent only of the recharge rate and not the amount of discharge.

#### **4.4.3. Electron diffraction and STEM/EELS results**

We have analyzed SAED patterns and measured intensity profiles after full lithiation and delithiation of  $\text{FeF}_3/\text{C}$  nanocomposite for 58.8, 23.5 and 8.8 mA/g cycling rates. We also collected the corresponding Fe-M and Li-K edges as well as the O-K, F-K and Fe-L spectra in order to determine the relative Li content and valence state of Fe. For each condition, we have taken twenty SAED and EELS patterns from various areas.

#### 4.4.3.1. Structural changes of the lithiated $\text{FeF}_3/\text{C}$

The SAED patterns shown in Figure 4-4 have been taken from two different areas of lithiated  $\text{FeF}_3/\text{C}$  electrode cycled under constant current of 58.8 mA/g to 1.5V (2.44 Li content). These patterns are typical patterns observed in this study corresponding to (a) rutile-type phase and (b) superposition of Fe and LiF phases. From the 20 diffraction patterns taken, three different diffraction patterns (A, B, C) have been observed suggesting that the lithiation process is not uniform. The corresponding intensity profile along with the simulated intensity profiles of the possible reference phases including Fe, LiF, and tetragonal ( $\text{P4}_2/\text{mmn}$ )  $\text{Li}_{1/4}\text{Fe}_{5/4}\text{Fe}_3$  and  $\text{FeF}_3$  (R-3c) are shown in Figure 4-3. The SAED intensity profiles of the intermediate phases have been compared with all stable phases obtained using first principle calculations [40]. In particular, all possible trirutile-type phases have been simulated and  $\text{Li}_{1/4}\text{Fe}_{5/4}\text{Fe}_3$  was found to be the best fit. A more detailed analysis is provided in the discussion. The intensity profile of area A shows the existence of trigonal (R-3c) and rutile phases, along with converted phases (LiF and Fe). In the SAED profile from area B, the rutile-like tetragonal phase is observed; however, the trigonal (R-3c) phase is no longer visible. The most intense reflections from LiF and Fe, marked in Figure 4-3 as  $I_1$  and  $I_2$ , are overlapped. However, the  $I_1/I_2$  intensity ratio of Fe is three times higher than the intensity ratio of LiF. Additionally, the intensity ratio of the converted phases increased ( $I_1/I_2$ ) compare to the intensity ratio of area A, indicating the precipitation of metallic Fe. The formation of Fe nanoparticles has been observed also by ADF-STEM imaging. The representative SAED pattern and intensity profile of area C reveal only the presence of the converted phases (LiF and Fe).



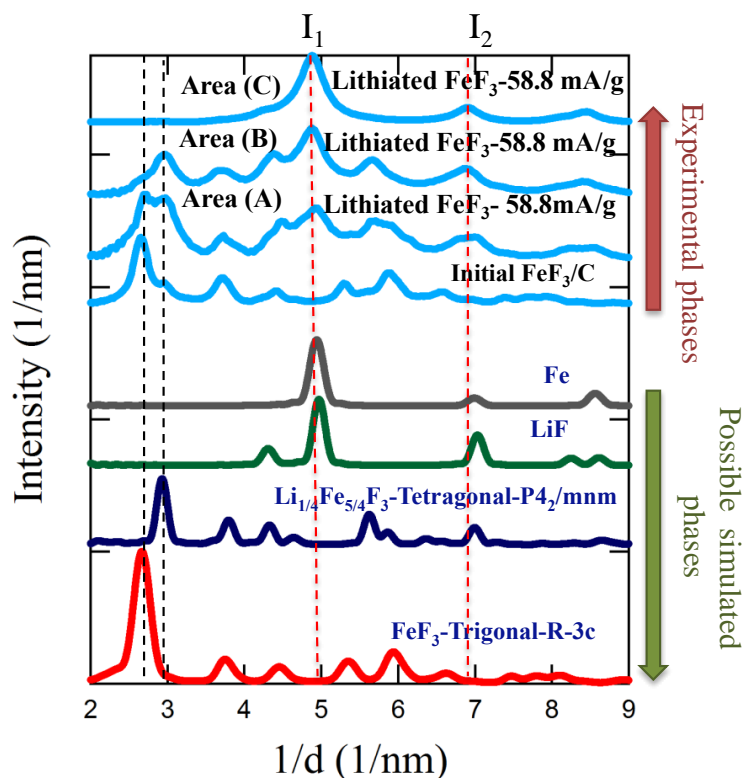


Figure 4-3 SAED intensity profiles of the possible phases (Fe, LiF,  $\text{FeF}_3$ , and tetragonal  $\text{Li}_{1/4}\text{Fe}_{5/4}\text{Fe}_3$  ( $\text{P4}_2/\text{mnm}$ )), lithiated  $\text{FeF}_3/\text{C}$  under a constant current of 58.8 mA/g, from different areas A, area C respectively, and initial  $\text{FeF}_3/\text{C}$ .

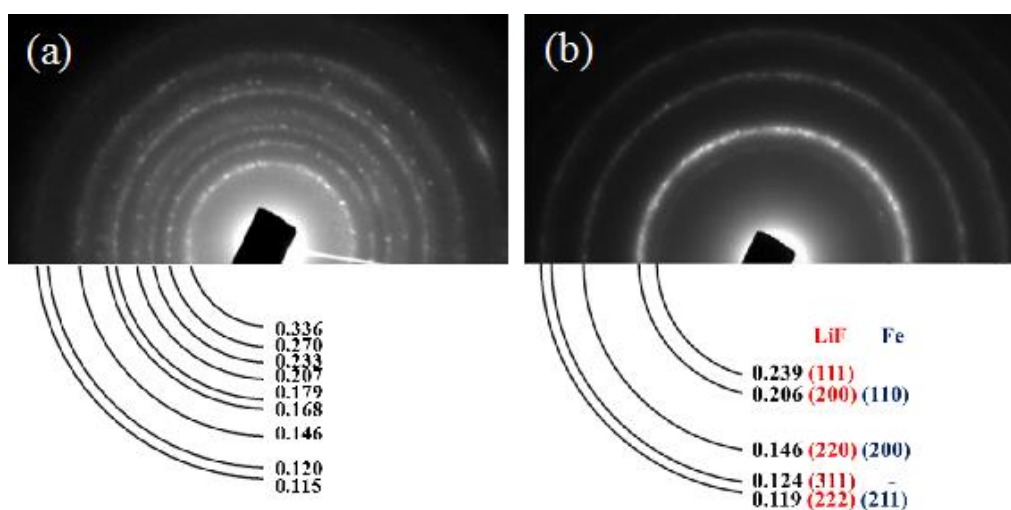


Figure 4-4 SAED patterns of the lithiated  $\text{FeF}_3/\text{C}$  nanocomposite electrode under a constant current of 58.8 mA/g, (a) representing the presence of the  $\text{Li}_{1/4}\text{Fe}_{5/4}\text{Fe}_3$  ( $\text{P4}_2/\text{mnm}$ ) phase, and (b) superposition LiF and Fe phases.

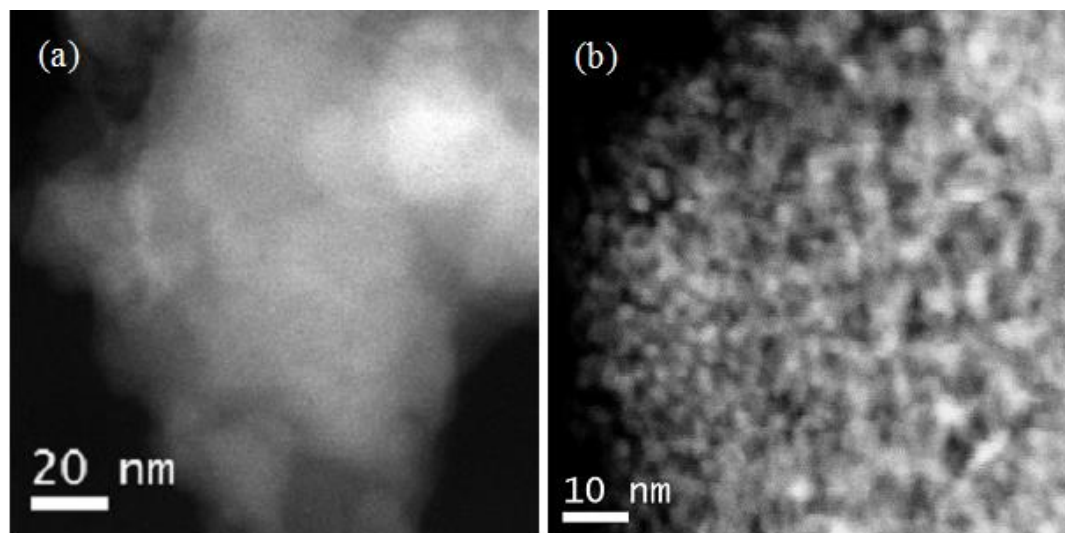


Figure 4-5 Lithiated  $\text{FeF}_3/\text{C}$  nanocomposite electrode under a constant current of 58.8 mA/g (a) ADF-STEM corresponding to area A of the sample, and (b) ADF-STEM corresponding to area B.

ADF-STEM images Figure 4-5 which are z-contrast images, were taken from areas A and B. The ADF-STEM image (Figure 4-5) from area A does not show any contrast, in spite of having  $I_1$  and  $I_2$  reflections in the intensity profile. This confirms that LiF is present but that  $\text{Fe}^0$  metallic has not yet formed in this region. However, the STEM image from area B reveals bright contrast, indicating the existence of metallic Fe with an average particle size of about 3 nm. In addition to diffraction, EELS spectra were acquired to provide more detailed information on Fe valence state and Li content from these different regions.

The results shown in Figure 4-6 reveal an increase in Li-K content from area A to area C. The Li-K edge and the F-K post peak from area C are characteristic of LiF. In addition, the changes in Fe valence from these different areas A, B and C were measured from the Fe  $L_3/L_2$  intensity ratio as described previously. The Fe valence states from areas A and area C have the highest ( $\text{Fe}^{+2.5}$ ) and lowest ( $\text{Fe}^0$ ) Fe valence state

respectively. This valence measurement provide further confirmation that in area C the material is fully converted to metallic Fe while remains unconverted in area A.

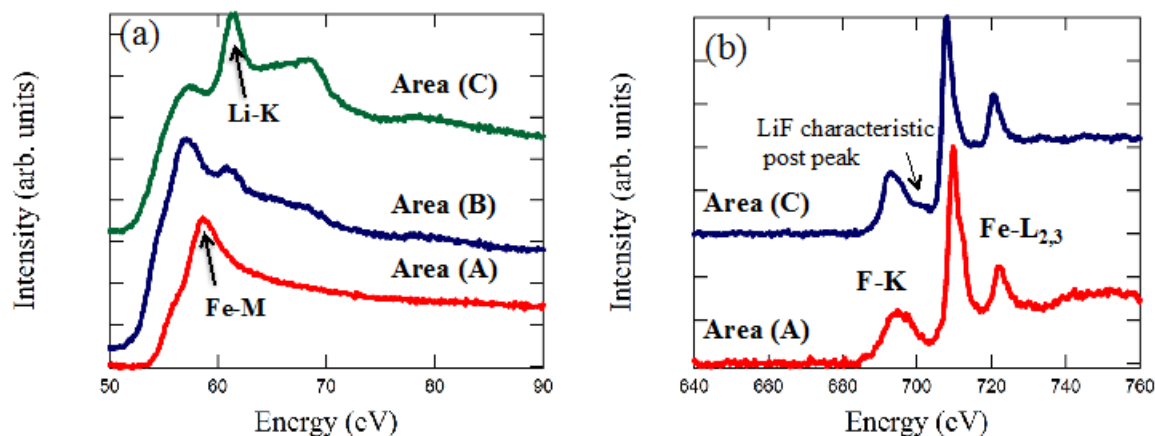


Figure 4-6 STEM-EELS spectra of the lithiated  $\text{FeF}_3/\text{C}$  nanocomposite electrode under a constant current of 58.8 mA/g, (a) Fe-M and Li-K edges (b) Fe- $\text{L}_{2,3}$  and F-K edges.

Figure 4-7 shows the SAED intensity profiles of the lithiated electrode cycled at 23.5 mA/g. At this cycle rate, an average of 2.59 Li is incorporated after discharge to 1.5 V. Two different SAED patterns were observed within the sample (area A and area B). In the SAED intensity profile from area A, a lithiated rutile-type phase along with converted phases (LiF and Fe) are presented. In area B, only converted phases are present. At this cycle rate the lithiated trigonal (R-3c) phase is no longer observed. This sample cycled at 23.5 mA/g, contained more regions with converted phases (LiF and Fe) as compared with those cycled at 58.8 mA/g.

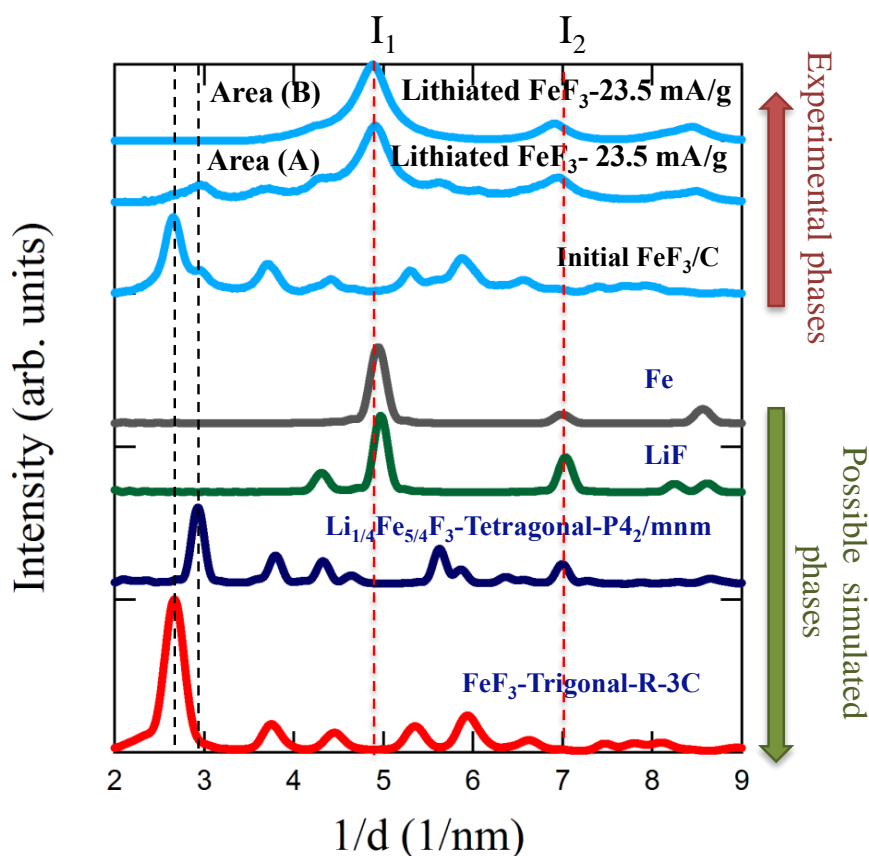


Figure 4-7 SAED intensity profiles of the possible phases (Fe, LiF,  $\text{FeF}_3$ , and tetragonal  $\text{Li}_{1/4}\text{Fe}_{5/4}\text{Fe}_3$  ( $\text{P4}_2/\text{mnm}$ )), and the lithiated  $\text{FeF}_3/\text{C}$  nanocomposite electrode under a constant current of 23.5 mA/g from different areas A, B.

Figure 4-8 shows the SAED intensity profile of the lithiated sample upon discharge to 1.5 V at the slowest rate of 8.8 mA/g. The representative SAED pattern and intensity profile show that this sample is uniformly lithiated and fully converted to LiF and Fe. The corresponding ADF and HRTEM images (Figure 4-9) were also recorded and all the ADF images show contrast, suggesting the presence of the Fe nanoparticles. In addition, the HRTEM image (Figure 4-9(b)) confirms the existence of nanocrystalline iron. Corresponding STEM-EELS spectra were also acquired from the fully lithiated sample at 8.8 mA/g in order to study the chemistry and bonding state. The shape of Li-K

edge with double peaks separated by 7.4 eV (Figure 4-10) is characteristic of LiF [31]. The Fe valence state measured using the Fe-L<sub>3</sub>/L<sub>2</sub> intensity ratio is consistent with Fe valence

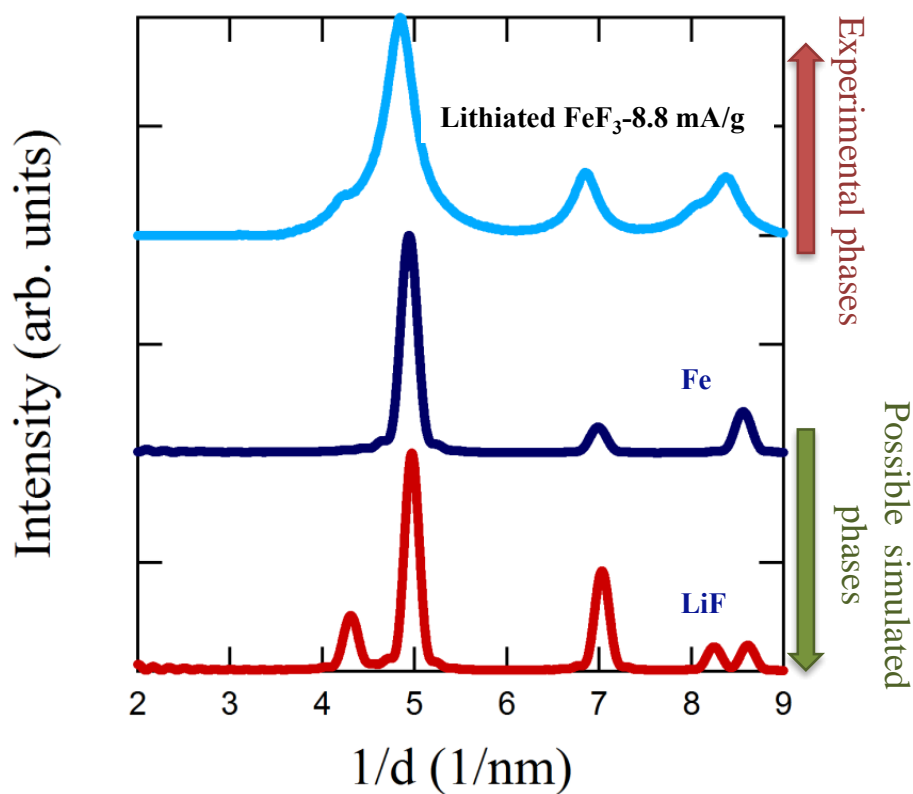


Figure 4-8 SAED intensity profile of the lithiated FeF<sub>3</sub>/C nanocomposite electrode under a constant current of 8.8 mA/g.

state of about zero (Fe<sup>0</sup>), which further confirms the homogenous and complete conversion process at this lowest lithiation rate of 8.8 mA/g.

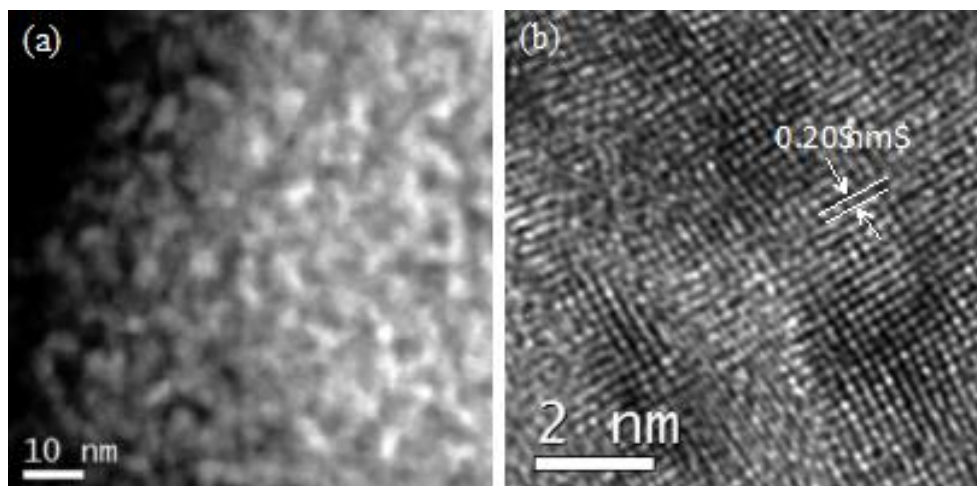


Figure 4-9 Lithiated  $\text{FeF}_3/\text{C}$  nanocomposite electrode lithiated under a constant current of 8.8mA/g, (a) ADF-STEM image, (b) HRTEM image.

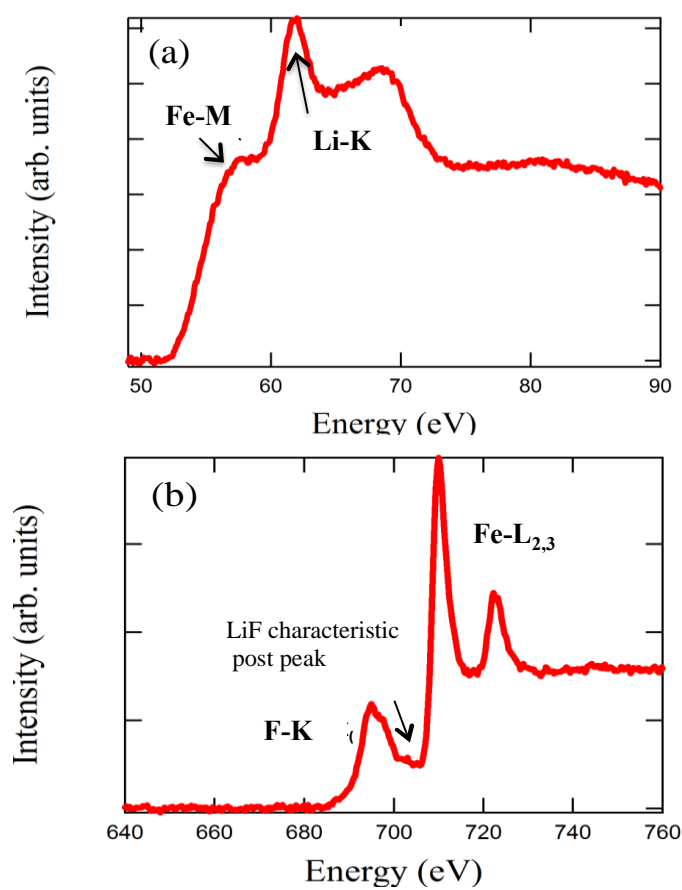


Figure 4-10 STEM-EELS spectra of the lithiated  $\text{FeF}_3/\text{C}$  nanocomposite electrode under 8.8 mA/g, (a) Fe-M and Li-K edges (b) Fe-L<sub>2,3</sub> and F-K edges.

#### 4.4.3.2. Structural changes of the delithiated FeF<sub>3</sub>/C

The SAED intensity profiles (Figure 4-11) of the fully delithiated sample at a constant rate of 58.8 mA/g reveal the existence lithiated rutile type (P4<sub>2</sub>/mmn) and trigonal (R-3c) phases. The presence of remaining lithium upon fully charged can be observed by the presence of Li-K edge in the EELS spectrum. At this stage of delithiation, LiF and metallic Fe reflections are no longer visible.

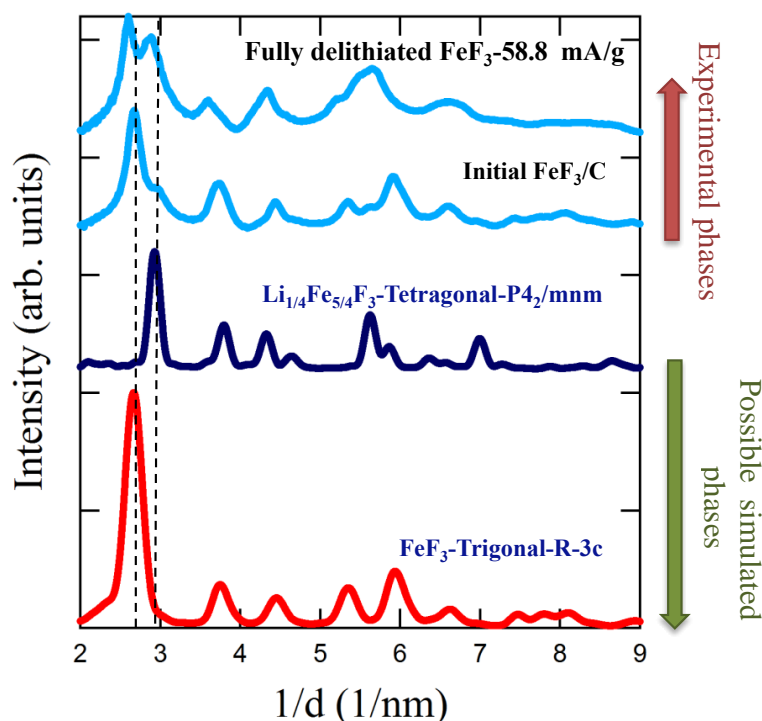


Figure 4-11 SAED intensity profiles of the possible phases (FeF<sub>3</sub>, and tetragonal (P4<sub>2</sub>/mmn) Li<sub>1/4</sub>Fe<sub>5/4</sub>Fe<sub>3</sub>), and delithiated FeF<sub>3</sub>/C at 4.5 V nanocomposite electrode cycled at 58.8 mA/g.

The delithiated sample cycled under the slowest constant current of 8.8 mA/g shows three SAED intensity profiles area A, area B and area C (Figure 4-12). The peaks corresponding to cubic structures (LiF and Fe) are no longer observed. In addition, the

ADF STEM images do not show any contrast confirming the complete reconversion of metallic Fe. The intensity profile of area C contains only rutile-type ( $P4_2/mnm$ ) reflections. However, the SAED intensity profiles (Figure 4-12) of area B show a mixture of lithiated rutile phase as well as a low fraction of trigonal phase. Interestingly, the SAED intensity profile from area A reveal only the existence of the initial trigonal ( $R-3c$ )  $FeF_3$  phase indicative of a full structural reconversion to the initial structure.

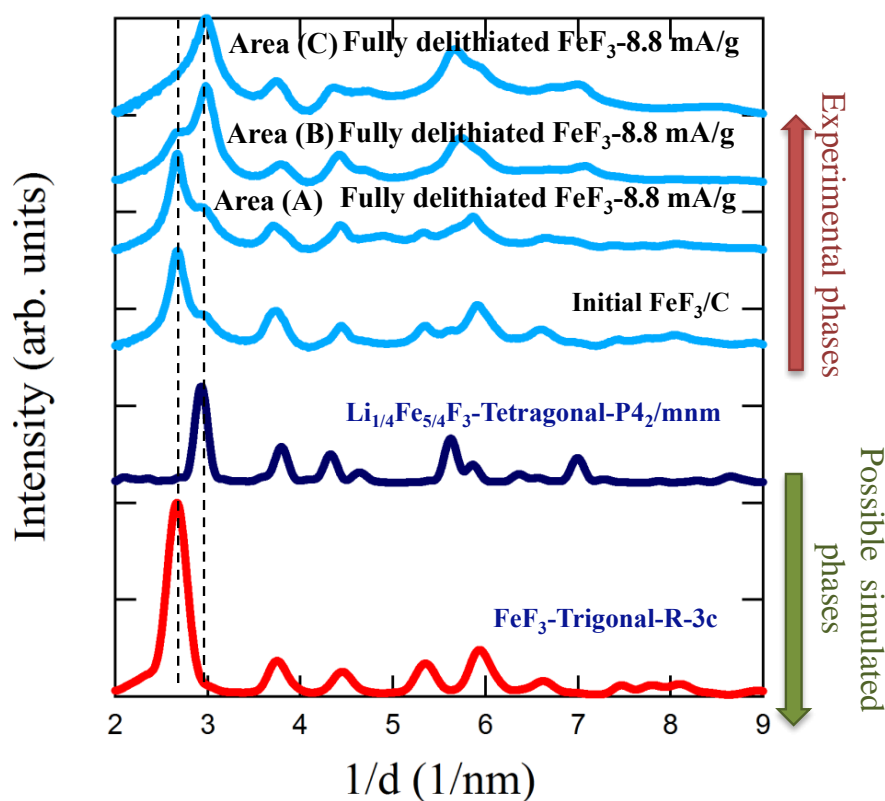


Figure 4-12 SAED intensity patterns of the possible phases ( $FeF_2$ , and tetragonal ( $P4_2/mnm$ )  $Li_{1/4}Fe_{5/4}Fe_3$ ), and delithiated  $FeF_3/C$  nanocomposite electrode under a constant current of 8.8 mA/g, from different areas A, B, and C

We performed STEM-EELS analysis from the corresponding area. The low loss spectrum taken from area A shown in Figure 4-13(a) displays only the presence of Fe-M



edge without any Li-K present. The F-K edge with a pre-peak located at 684.8 eV (c.f. Figure 4-13(b)) is indicative of a  $\text{FeF}_3$  type structure [35]. Moreover, the Fe valence state was determined from the Fe  $L_3/L_2$  intensity ratio and the value of  $\text{Fe}^{+2.7}$ , which corresponds to the Fe valence of the initial material. This results suggests that only when the electrode is fully delithiated that the structure reconverts back to its initial  $\text{FeF}_3$  (R-3c) trigonal structure.

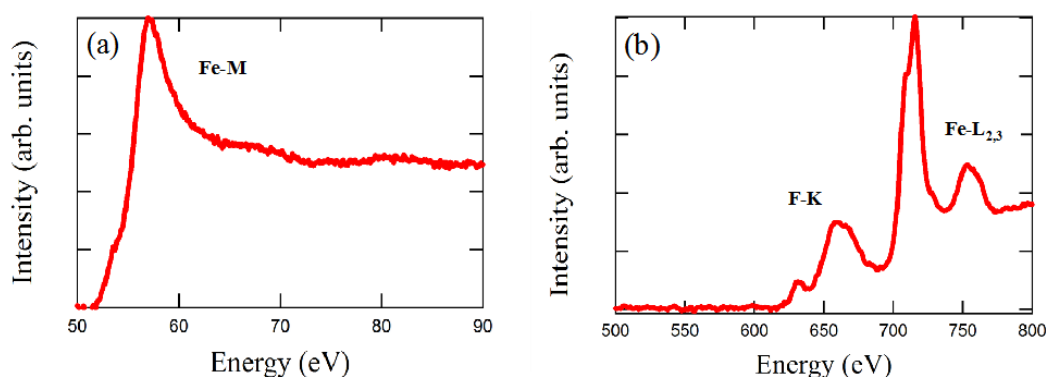


Figure 4-13 STEM-EELS spectra of the delithiated  $\text{FeF}_3/\text{C}$  nanocomposite under constant current of 8.8 mA/g (a) Fe-M and Li-K edges (b) Fe- $L_{2,3}$  and F-K edges.

Other regions from the electrode showing rutile-type ( $\text{P4}_2/\text{mmn}$ ) structure are not fully delithiated and contain some residual Li. In these areas, the Fe valence state was  $\text{Fe}^{+2.3}$ .

The residual Li in the electrode, which is rate dependent, is therefore critical in understanding reconversion structures. As shown in the voltage profile of Figure 4-2(b), the residual Li content at 4.5 V is 0.06 and 0.31 for electrode recharged at rates of 8.8 and 58.8 mA/g respectively.

#### 4.4.3.3. Structural transformations after cycling:

The discharge capacity as a function of cycle number is shown in Figure 4-14. The  $\text{FeF}_3/\text{C}$  structure does not display good capacity retention and its capacity deteriorated from about 540 mAh/g (after 1 cycle) to 100 mAh/g (after 20 cycles).

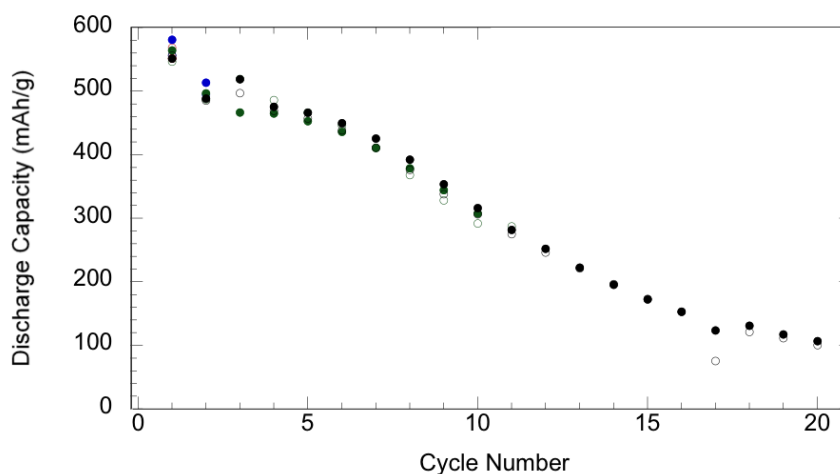


Figure 4-14 Discharge capacity vs. cycle number of the  $\text{FeF}_3/\text{C}$  nanocomposite cycle at 8.8 mAh/g.

The SAED the intensity profile of the lithiated  $\text{FeF}_3/\text{C}$  (at 1.5V) after 1 cycle (Figure 4-15(c)) shows the presence of conversion phases ( $\text{LiF}$  and  $\text{Fe}$ ) ( $I_1, I_2$  reflections corresponding to the most intense cubic reflection of both  $\text{Fe}$  and  $\text{LiF}$ ). However, two different intensity profiles were observed for the lithiated samples after 20 cycles as shown in Figure 4-15. The reflections of the SAED intensity profile from Area A (Figure 4-15) corresponds only to the superposition of  $\text{Fe}$  and  $\text{LiF}$  reflections, while the intensity profile from Area B (Figure 4-15) showing the superposition of  $\text{Fe}$  and  $\text{LiF}$  along with rutile-type reflections.

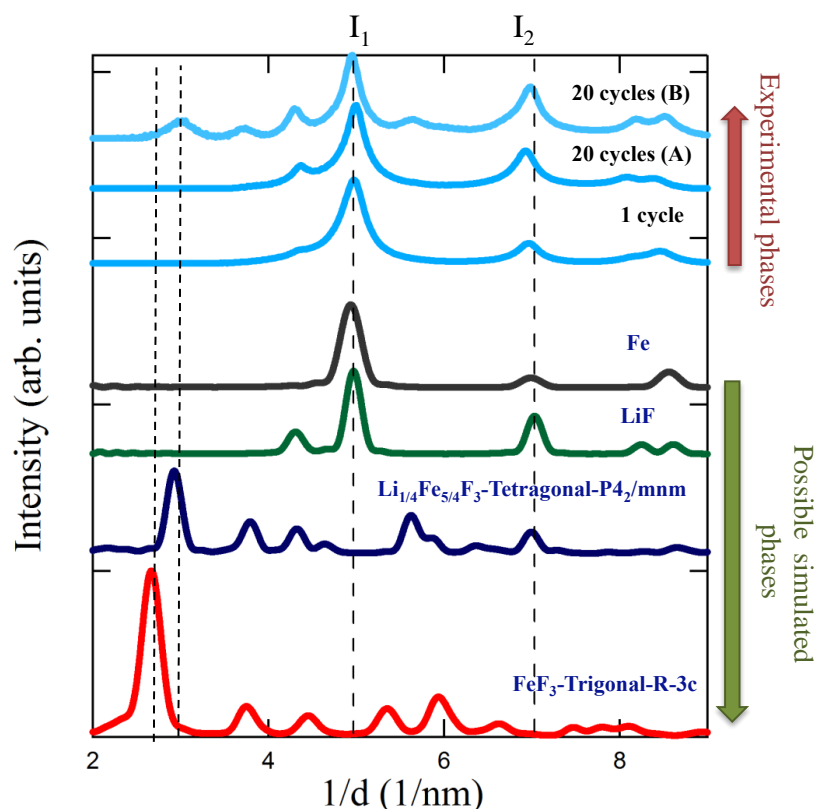


Figure 4-15 SAED intensity profiles of the lithiated  $\text{FeF}_3/\text{C}$  nanocomposite electrode under a constant current of 8.8 mA/g after different cycle number and the possible phases ( $\text{FeF}_3$ ,  $\text{LiF}$ ,  $\text{Fe}$ , and tetragonal ( $\text{P4}_2/\text{mnm}$ )  $\text{Li}_{1/4}\text{Fe}_{5/4}\text{F}_3$ ).

Similarly, The SAED intensity profile of delithiated  $\text{FeF}_3/\text{C}$  (at 4.5V) after 1 cycle (Figure 4-16) show the presence of reconverted rutile-type phase while two different diffraction patterns are observed after 20 cycles, indicating a superposition of rutile-type and  $\text{Fe}$  with  $\text{LiF}$  in area marked A and only  $\text{Fe}$  and  $\text{LiF}$  in area B. This result indicates that the structure from Area B does not revert back to a lithiated-rutile-type structure but remains in the form of  $\text{Fe}$  nanoparticles with crystalline  $\text{LiF}$ . The diffracted intensities from  $\text{LiF}$  appears relatively more intense indicating a higher molar fraction of  $\text{LiF}$  in the untransformed area. Also, the presence of  $\text{Fe}$  nanoparticles is confirmed from ADF-STEM image, which reveals a strong contrast associated with the  $\text{Fe}$  nanoparticles.

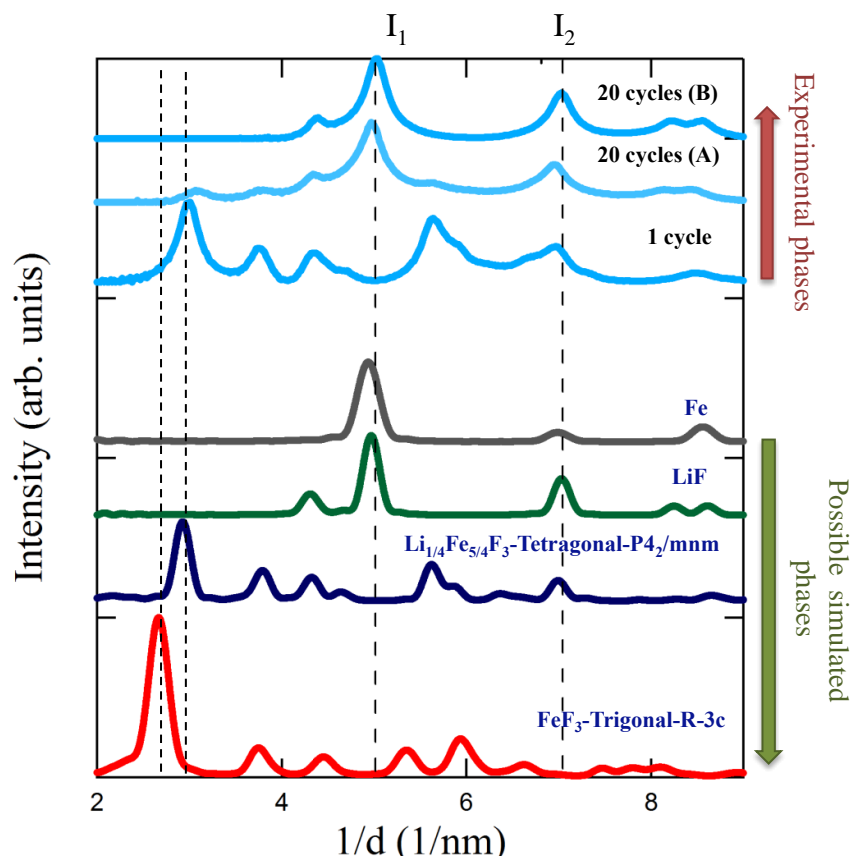


Figure 4-16 SAED intensity profiles of the delithiated  $\text{FeF}_3/\text{C}$  nanocomposite electrode under a constant current of 8.8 mA/g after different cycle number and the possible phases ( $\text{FeF}_3$ ,  $\text{LiF}$ ,  $\text{Fe}$ , and tetragonal ( $\text{P4}_2/\text{mnm}$ )  $\text{Li}_{1/4}\text{Fe}_{5/4}\text{Fe}_3$ ).

#### 4.5. Discussion

In this work we have studied the role of electrochemical cycling rate on the structural changes. It was found that the lithiation rate did not affect the first stage of lithiation (intercalation) but had profound effects on the second stage of lithiation (conversion). The voltage hysteresis  $\Delta V$  increases as the rate of lithiation increases which caused mainly by lowering voltage profile. In addition, the content of Li at 1.5 V increases as cycling rate decreases resulting in a higher capacity. The residual remaining Li at full recharge (to 4.5 V) is also dependent on recharge rate; this residual Li is the

main factor affecting phase formation. Upon lithiation at the lowest rate of 8.8 mA/g with 2.75Li, we have observed a complete conversion reaction of  $\text{FeF}_3/\text{C}$  to LiF and Fe. However, at faster rates of 23.5 and 58.8 mA/g we have observed non-uniform lithiation with the presence of untransformed phases.

In addition, as the discharge rate decreased, more Li is introduced into the discharged electrode at 1.5 V with an increase in the fraction of converted phases (LiF + Fe). This is most likely due to the decrease in the reaction kinetics [84]. It was measured recently that on conversion the effective diffusion coefficient of  $\text{FeF}_3$  is low ( $1.71 \times 10^{-18} \text{ cm}^2/\text{s}$ ) and therefore requires low current rates for the progress of conversion reaction [41]. We also found that at high rates, the Li distribution is highly inhomogeneous resulting in formation of intermediate phases upon fully discharged/charged. Regions with the lowest Li content contains lithiated trigonal phase (R-3c), and lithiated rutile-type phase in addition to the converted phases (LiF without  $\text{Fe}^0$ ). In areas with intermediate lithium content the lithiated trigonal phase is no longer present and both lithiated rutile-type and converted phases (Fe and LiF) are present. However, there is not any intermediate phase (rutile or trigonal) in areas with the highest lithium content and the electrode is fully converted to LiF and  $\text{Fe}^0$ . This shows that the lithiated trigonal phase is an intercalated phase of the initial material and the lithiated trigonal phase transformed to the lithiated rutile structure along with precipitation of  $\text{Fe}^0$  in area B (higher lithium content region). This is in agreement with Badway et al. results [7] who showed that the  $\text{Li}_x\text{FeF}_3$  (rutile-type structure) peaks decreased in intensity and Fe peaks grew in intensity by further lithiation ( $0.92 < \text{Li} < 2.42$ ). The theoretical group [40] suggested that  $\text{Li}^+$  can be inserted into trigonal (R-3c)  $\text{FeF}_3$  (discharging) up to  $\text{Li} = 0.25$

( $\text{Li}_{0.25}\text{FeF}_3$ ), and then from  $\text{Li} = 0.25$  up to  $\text{Li} = 0.5$  is a transformation from trigonal structure to trirutile type structure ( $\text{Li}_{0.5}\text{FeF}_3$ ). Also, they mentioned that further lithiation from 0.25 Li to  $\text{Li} = 0.5$  is also likely to occur through intercalation process, which has been observed in experimental works [21]. This is because the intercalation process only has little higher energy (25 meV/atom) than trirutile structure, and transformation from trigonal to trirutile requires significant atomic rearrangements. They reported that  $\text{Li}_{1/4}\text{Fe}_{5/4}\text{F}_3$  phase (rutile-type structure) is form upon further lithiation. Then at  $\text{Li} > 0.5$ , the trirutile structure converts into LiF and Fe [21, 40].

Upon charge (delithiation), the resulting structures are also dependent on the residual amount of Li. We observed that the regions without Li reconverted back to the initial trigonal (R-3c)  $\text{FeF}_3$  structure. However, in the regions with residual lithium content, a lithiated rutile-type phase is observed. Doe et al. showed that upon complete reconvension process  $\text{FeF}_3$  trirutile type structure may form. They proposed that the reconvension process follows by structural changes from rocksalt (LiF) to spinel, ilmenite and defect trirutile. In addition, this group reported that due to the little energy difference between defect trirutile and trigonal  $\text{FeF}_3$ , it is likely that defect trirutile structure form upon fully delithiation [40]. Doe et al also proposed that the structure of intermediate trirutile phases for  $\text{FeF}_3$  are  $\text{Li}_{1/4}\text{Fe}_{5/4}\text{F}_3$ ,  $\text{Li}_{1/2}\text{FeF}_3$ ,  $\text{LiFe}_{1/2}\text{F}_3$ , and defect trirutile  $\text{FeF}_3$  [40]. The ordered trirutile  $\text{LiFe}_2\text{F}_6$  ( $\text{Li}_{1/2}\text{FeF}_3$ ) with space group  $p4_2/mnm$  is formed from the sequential stacking of edge-shared  $\text{Fe}^{2+}\text{F}_6$ ,  $\text{Fe}^{3+}\text{F}_6$ , and  $\text{LiF}_6$  octahedra along the c direction [87]. Therefore along the c-axis the cell is now 3 time the length in the rutile ( $P4_2/mnm$ )  $\text{FeF}_2$  structure. In the disordered trirutile lattice the cations are now arranged randomly along the c direction giving rise to diffracted intensities very similar to the

(P4<sub>2</sub>/mnm) FeF<sub>2</sub> structure. There is only one reported study on the synthesis of LiFe<sub>2</sub>F<sub>6</sub> trirutile phase but their X-ray Rietveld analysis showed that the structure was a disordered trirutile phase [87]. The results of our study revealed a rutile-type intermediate phase formed after delithiation which is identical to the intermediate phase formed upon lithiation. In order to assess the type of rutile-type that could possibly formed, we performed ab-initio simulations of intensity profiles for all reported trirutile phases taking spherical particles 3 nm in diameter and containing about 7,000 atoms. The results are depicted in Figure 4-17. The intensity profile of the ordered trirutile phases (Li<sub>1/2</sub>FeF<sub>3</sub>, LiFe<sub>1/2</sub>F<sub>3</sub>, and defect trirutile FeF<sub>3</sub>) show a strong first reflection corresponding to the superposition of the (002) and (101) reflections. In the disordered trirutile LiFe<sub>2</sub>F<sub>6</sub>, the intensities of these reflections are effectively zero. In the Li<sub>1/4</sub>Fe<sub>5/4</sub>F<sub>3</sub> trirutile phase, Li and Fe share the 2a atomic site (with half site occupancy each) which in effect breaks the Fe<sup>2+</sup>-Fe<sup>3+</sup>-Li order along the c-axis and leads to a structure with an intensity profile similar to a disordered trirutile phase. This Li<sub>1/4</sub>Fe<sub>5/4</sub>F<sub>3</sub> trirutile phase is present in the ternary phase diagram as a possible equilibrium phase before the formation of either FeF<sub>2</sub> or FeF<sub>3</sub> upon complete delithiation [40]. Of all the possible trirutile phases, the Li<sub>1/4</sub>Fe<sub>5/4</sub>F<sub>3</sub> agrees well with our experimental results.

Based on NMR results [21] and following Doe et.al thermodynamic phase equilibrium, the following charge process has been proposed:



Further removal of Li at higher potential will lead to FeF<sub>3</sub> as FeF<sub>2</sub> does not correspond to the thermodynamic equilibrium phase.

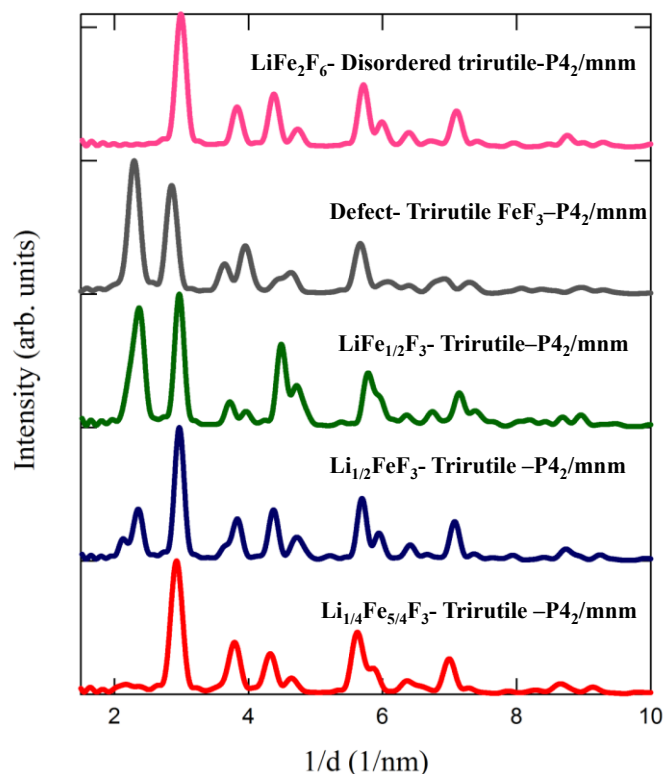


Figure 4-17 Simulated SAED intensity profiles for possible trirutile phases.

#### 4.6. Conclusions

In this article we studied the significance of cycling rate on the structural evolution and electrochemical performance of  $\text{FeF}_3/\text{C}$  nanocomposite during cycling. The results provide strong evidence for the correlation between structural changes and cycling rate. We observed that as the rate increases, the lithiation is less uniform through the electrode. This Li inhomogeneity gives rise to formation of different phases in different regions of the sample. The lithiated samples (1.5V), which are cycled under 58.8 mA/g and 23.5 mA/g did not convert completely to LiF and metallic Fe and contained the lithiated rutile and trigonal phases; however, the sample cycled at 8.8 mA/g was fully converted to LiF and Fe. Interestingly, the lithited rutile and trigonal phases, which are



observed upon lithiation are also formed after reconversion, reflecting the reaction reversibility in  $\text{FeF}_3/\text{C}$ . Furthermore, the structural evolution of the lithiated/delithiated samples after various cycle numbers (1, 20) was studied to determine the causes of capacity fading. We found that as the cycle number increases, the chance of complete reconversion reaction of the lithiated phases are reduced. This is most likely attributed to the formation of the SEI layer (Li, Meng et al. 2012, Gmitter, Halajko et al. 2013).

## 5. Investigation of the SEI Layer Formation in Conversion Iron Fluoride Cathodes by Combined STEM/EELS and XPS <sup>4</sup>

### 5.1. Abstract

Conversion iron difluoride ( $\text{FeF}_2$ ) positive electrode provides in principle high specific capacity in Li-ion batteries. However, important capacity fading is observed upon cycling, often attributed to the continuous growth of a solid electrolyte interphase (SEI) layer at the electrode/electrolyte interface. In this work, transmission electron microscopy (TEM), electron energy loss spectroscopy (EELS), and x-ray photoelectron spectroscopy (XPS) were used in combination to study both the evolution of the  $\text{FeF}_2/\text{C}$  active material and the growth and evolution of the SEI layer upon cycling. Two main sources of capacity loss have been found. Not surprisingly, we found that reconversion is strongly impeded with increasing cycle number, leaving mainly  $\text{LiF}$  and  $\text{Fe}^0$ , which correlates with the irreversible growth of the SEI layer preventing  $\text{Li}^+$  migration. In addition, an increasing amount of  $\text{Fe}^{2+}$  appeared trapped into the SEI with increasing cycle number, thus resulting in the loss of active material.

### 5.2. Introduction

Recently, conversion materials based on metal fluorides have received considerable attention as candidate positive electrode for Li-ion batteries, due to their high capacity [6, 88]. This characteristic is achieved through the incorporation of more than one  $\text{Li}^+$  ion per structural unit cell into the host lattice. In particular, conversion

---

<sup>4</sup> M. Sina, R. Thorpe, S. Rangan, N. Pereira, R. A. Bartynski, G. G. Amatucci and F. Cosandey, "Investigation of the SEI Layer Formation in Conversion Iron Fluoride Cathodes by Combined STEM/EELS and XPS" in prep (2014)

batteries using iron fluorides have been shown to operate at high voltages and high energy densities. However, short cycle life, hysteresis, and poor kinetics have until now restricted their potential for commercialization [6, 88]. Poor cycle life is attributed in part to the growth of a solid-electrolyte interphase (SEI) layer at the surface of the electrodes, as a result of the decomposition of the electrolyte [12, 15, 89-92]. Although it has been shown that the presence of a stable thin SEI can in some instances be beneficial during cycling, as it prevents further reaction of the electrolyte with the electrode material, the situation appears complex in the case of conversion batteries. Unlike intercalation materials, conversion materials undergo considerable structural changes during the lithiation-delithiation process, involving both alteration of the crystal structures and coexistence of separate nanophases. The surface of the electrode is thus constantly modified and in principle offers fresh reactive site leading to the electrolyte decomposition [91]. Consequently, A detailed understanding the SEI formation mechanism at the surface of conversion materials is needed.

Identification and structure of SEI compounds has been addressed for several electrodes/solvents/Li- salts [93, 94]. These studies point to the fact that the SEI composition and the growth mode depend not only on the salts and solvents used in the electrolyte, but also - not surprisingly - on the cathode materials and the cycling parameters (e.g. temperature, cycling rate, and voltages). In the absence of fluorine sources, SEI constituents have been identified as lithium carbonates ( $\text{Li}_2\text{CO}_3$ ), lithium alkyl carbonates ( $\text{R-O-COOLi}$ ) or lithium alkoxides ( $\text{R-CH}_2\text{-COLi}$ ), and are thought as being products of both the electrolyte solvent and salt decomposition at the surface of the electrodes [94, 95](Dedryvere, Laruelle et al. 2004, Tian, Swiatowska et al. 2013). In the

presence of fluorine, especially in the form of lithium salts ( $\text{LiPF}_6$ ), the major decomposition product that has been observed is  $\text{LiF}$ , which has in part been attributed to the following chemical reaction:  $\text{LiPF}_6 \rightarrow \text{LiF} + \text{PF}_5$  [15, 20, 89, 90, 96-98]. In the unavoidable presence of water contamination,  $\text{PF}_5$  is believed to immediately degrade and release  $\text{HF}$  that can dissolve compounds such as  $\text{Li}_2\text{CO}_3$  and lead to further  $\text{LiF}$  formation [98, 99]. Reports also indicate that the SEI is dynamic and that both composition and thickness can vary as a function of cycle life, in a reversible or non-reversible way. Non-reversible behaviors induce a continuous growth of the SEI, leading in most cases to limited  $\text{Li}^+$  mobility and capacity fading [15, 90, 97, 98, 100].

In this work, we study the simultaneous morphological and chemical evolutions of the SEI layer of the promising  $\text{FeF}_2$  cathode material upon cycling. Helium ion microscopy is used to characterize the material external morphology at the  $\mu\text{m}$  scale. Transmission electron microscopy and electron energy loss spectroscopy (TEM/EELS) are used to identify bulk phases and local structure. In addition, a surface sensitive technique, X-ray photoemission spectroscopy (XPS), is used in conjunction with controlled sputter depth profiling to probe both the surface of the SEI and deeper layers of the material. As the chemistry of the SEI layer can be largely affected by exposure to atmosphere, transfer from battery cells to either the TEM or XPS systems were done in a controlled environment. Using a combination of these surface and bulk sensitive techniques, the nature of the decomposition products of the electrolyte and the deterioration of the cathode material are correlated to the cycling performance of  $\text{FeF}_2$ .

### 5.3. Experimental

#### 5.3.1. Material synthesis and electrode fabrication

The iron fluoride nano-powder was synthesized via a solution process involving reacting iron metal with a fluorosilicic acid aqueous solution. After filtering the excess iron metal, drying the solution led to a  $\text{FeSiF}_6 \cdot 6\text{H}_2\text{O}$  precursor. The precursor was then heat-treated under flowing argon at temperature ranging from  $250^\circ\text{C}$  to form 20nm  $\text{FeF}_2$  nanoparticles. The  $\text{FeF}_2/\text{C}$  nano-composites were then prepared by high-energy ball milling with 15 wt% activated carbon black (ASupra, Norit) for 1 hour in a helium atmosphere [14].

#### 5.3.2. Electrochemistry

The plastic electrodes were fabricated using the Bellcore developed process [14] hexafluoropropylene (PVDF-HFP, Kynar 2801, Elf Atochem), carbon black (Super P,MMM), and dibutyl phthalate (Aldrich). After removal of the dibutyl phthalate plasticizer, the resulting electrodes typically consisted of 57% active material and 12% carbon black. The coin cells were assembled in a helium-filled glove box. Lithium foil was used as a counter electrode and a glass-fiber separator (GF/D, Whatman) and a layer of polypropylene separator (Celgard) was saturated with 1M  $\text{LiPF}_6$  in ethylene carbonate: dimethyl carbonate electrolyte (EC:DMC 50:50 in vol %) from BASF. Transformation kinetics, capacity and reversibility of conversion electrodes being dependent on both cycling rate and temperature, all samples were cycled in galvanostatic mode at  $60^\circ\text{C}$  for optimum performances, using a constant current density of  $50 \text{ mA g}^{-1}$  between 1.5 and 4.5 V. Further experimental details can be found elsewhere [14].

### 5.3.3. TEM

The electrochemical cells were disassembled in a helium-filled glove box and the powder extracted from the positive electrode was rinsed in DMC in order to remove most of the  $\text{LiPF}_6$  salt in contact with the SEI layer. The electrode powder was then dispersed in DMC and a few drops placed on a TEM lacy carbon film supported on a copper grid. The TEM samples were loaded on a vacuum transfer holder and transferred to the TEM without exposure to air. Selected area electron diffraction (SAED) pattern, annular dark field scanning transmission electron microscopy (ADF-STEM), and electron energy loss spectroscopy (EELS) were recorded at 197 KV with a JEOL-2010F microscope equipped with a Gatan imaging filter (GIF) spectrometer. The energy resolution of the EELS spectra measured from the full width at half magnitude (FWHM) of the zero-loss peak (ZLP) was 0.9 eV. Also, a collection angle ( $\beta$ ) of 20 mrad and a convergence angle ( $\alpha$ ) of 10 mrad were used for the EELS spectra. The Process Diffraction program [23] was utilized for obtaining SAED intensity profiles by first taking the rotational average followed by background removal. In addition, the JEMS software [44] was used for the simulation of SAED intensity profiles of nano-sized particles in the 2-5 nm range. These were obtained ab-initio by calculating the pair distribution function and solving the Debye equation.

### 5.3.4. Helium Microscopy

Helium ion microscopy was performed using a Zeiss Orion Plus system, using 30 kV acceleration voltages, and a 0.2–0.4 pA beam current. No beam damage was observed

using these parameters. The samples were briefly exposed to air for less than 1 minute upon transfer in the HIM system vacuum.

### 5.3.5. X-ray Photoelectron Spectroscopy (XPS)

XPS measurements were performed with a Thermo ESCALAB 250 Xi using monochromated 1486.6 eV Al K $\alpha$  x-rays. The total instrument resolution was approximately 0.5 eV. During measurements, a flood gun using low-energy electrons and Ar<sup>+</sup> ions was used to compensate for sample charging. The component of the C 1s photoelectron peak at -284.8 eV was used as a binding energy reference. Most core levels were fitted with Voigt profiles after subtracting a Shirley background function. Fe 2p core levels were fitted with spectra taken from high-purity FeF<sub>2</sub> and Fe<sup>0</sup> reference samples. The samples were transported in a nitrogen atmosphere and introduced in to the vacuum system using a nitrogen-filled glove bag. In order to determine the thickness and composition of the SEI layer and the oxidation state of iron in the cycled cathodes, XPS spectra were taken before and after sputtering with 200 eV Ar<sup>+</sup> ions in ultra-high vacuum. Sputter rates were calibrated with Ta<sub>2</sub>O<sub>5</sub> and then adjusted to account for the high carbon content of the cycled FeF<sub>2</sub> samples. A FeF<sub>2</sub> powder reference sample was sputtered using a low ion beam current, and its oxidation state was not observed to change. At higher current, a small amount of reduction occurred due to the preferential removal of fluorine ions from the powder. Conversely, sputtering a prepared mixture of Fe<sup>0</sup> and PVDF powder at low current resulted in the formation of FeF<sub>2</sub>. Consequently, the amount of FeF<sub>2</sub> in these samples is likely overestimated after low-current sputters and underestimated after high-current sputters.

## 5.4. Results and Discussion

### 5.4.1. Electrochemical performance of the FeF<sub>2</sub>/C cathode material and sampling choice

A typical specific capacity curve for the FeF<sub>2</sub>/C positive electrode as a function of cycle number is shown in Figure 5-1. FeF<sub>2</sub> can yield a discharge capacity up to 441 mAh/g nanocomposite in the first cycle, equivalent to 519mAh/g of FeF<sub>2</sub> amounting to 90% of its theoretical capacity. However, the specific capacity curve reveals the material gradually loses 32% of its capacity to reach 300 mA/g after five cycles, after which a considerable capacity fade is observed. The specific capacity drops to 80 mAh/g after 20 cycles. In order to probe the mechanisms causing capacity loss, a set of cells have been prepared and disassembled in their lithiated or delithiated state after 1, 2, 10 and 20 cycles.

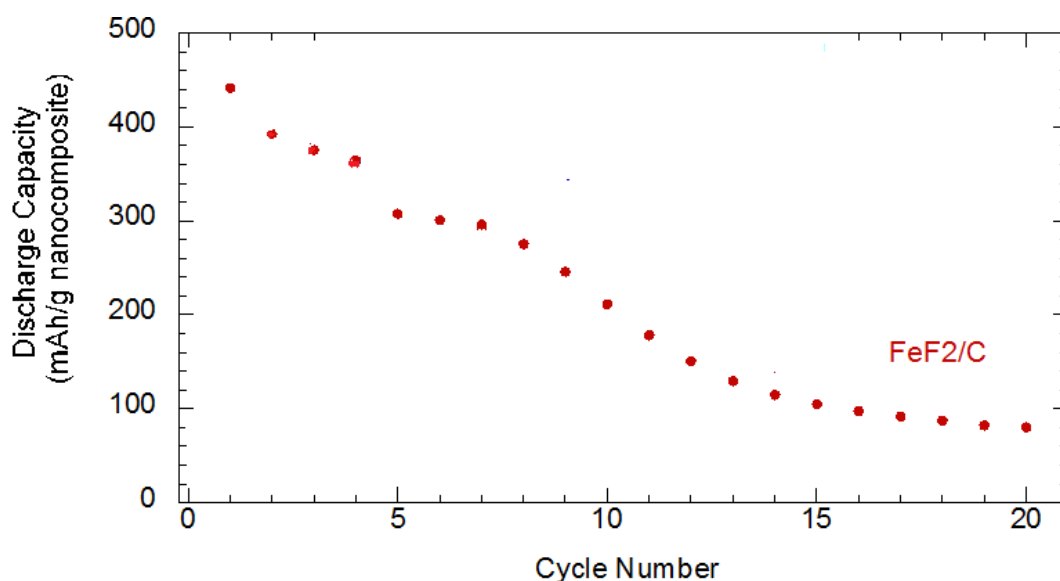


Figure 5-1 Discharge capacity vs. cycle number of the FeF<sub>2</sub>/C nanocomposite electrode cycled at 50 mA/g, at 60°C.



### 5.4.2. Surface Morphology

Large morphological differences were observed for blended  $\text{FeF}_2$  particles exposed to high cycle numbers. As an example, helium ion microscopy pictures of typical surfaces of the lithiated  $\text{FeF}_2$  sample stopped after the first cycle and after the 20<sup>th</sup> cycle, are presented in Figure 5-2(a) and Figure 5-2(b-c), respectively. Whereas the surface of the  $\text{FeF}_2$  containing material appears smooth and presents large flat-regions even after one conversion cycle, the surface of the second sample is characterized by a high degree of roughness. This roughness is interpreted as the physical evidence of the growth of an SEI overlayer, surrounding the  $\text{FeF}_2$ -containing particles. Further analysis from TEM and XPS will help confirm this assignment in the following work.

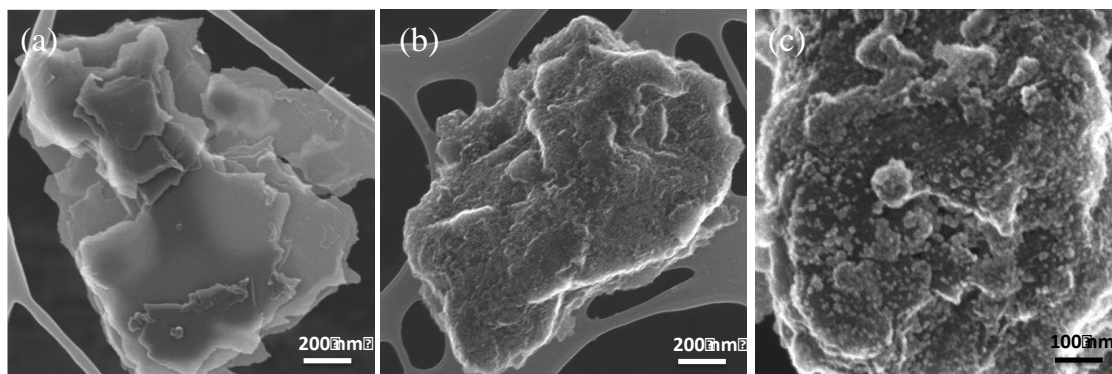


Figure 5-2 Helium ion microscope image of the lithiated  $\text{FeF}_2/\text{C}$  material after 1 (a), and after 20 cycles (b,c).

### 5.4.3. TEM/STEM characterization

Two aspects of the materials evolution upon cycling can be studied in parallel using TEM/STEM analysis: the transformation of the active part of the  $\text{FeF}_2$  cathode material and the appearance evolution of the SEI layer.

(a) *Cathode material evolution upon cycling*

The SAED pattern of the lithiated  $\text{FeF}_2$  sample after 1 cycle shown in Figure 5-3) indicates that the electrode electrochemically reduced to form LiF and metallic Fe. Similar structure was observed for all of the lithiated electrodes.

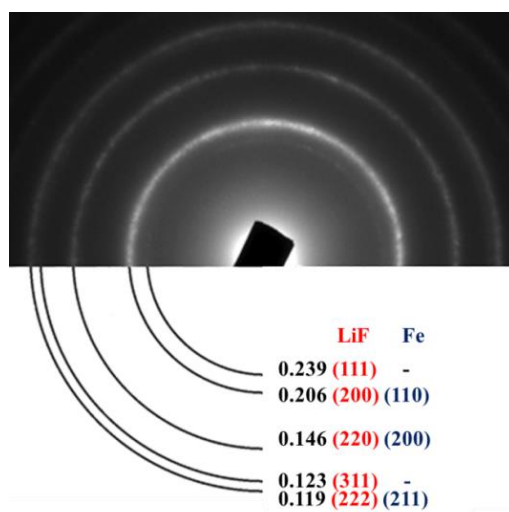


Figure 5-3 SAED pattern and ADF images of the delithiated sample (a,b) after 1 cycle, (c,d) after 20 cycles.

SAED patterns and ADF-STEM images of the fully delithiated samples after 1 cycle and after 20 cycles, are compared in Figure 5-4. The diffraction pattern obtained for the sample cycled once (Figure 5-4(a)) indicates full reconversion toward the expected  $\text{FeF}_2$  retail phase.

Its corresponding ADF-STEM image, shown in Figure 5-4(b) is also compatible with a single homogeneous phase. After 20 cycles however, the diffraction pattern of the cathode material, shown in Figure 5-4(c), indicates the coexistence of both LiF and metallic Fe. This inhomogeneous structure is also evident from the corresponding ADF-STEM image of Figure 5-4(d) indicating phase separation, with the high-Z element Fe, appearing as bright features. Delithiated intermediate samples, after 2 and 10 cycles, displayed coexisting  $\text{Fe}^0$ , LiF and  $\text{FeF}_2$  phases. Reconversion into  $\text{FeF}_2$  is clearly impeded after 20 cycles, in good agreement with the observed capacity loss (Figure 5-1).

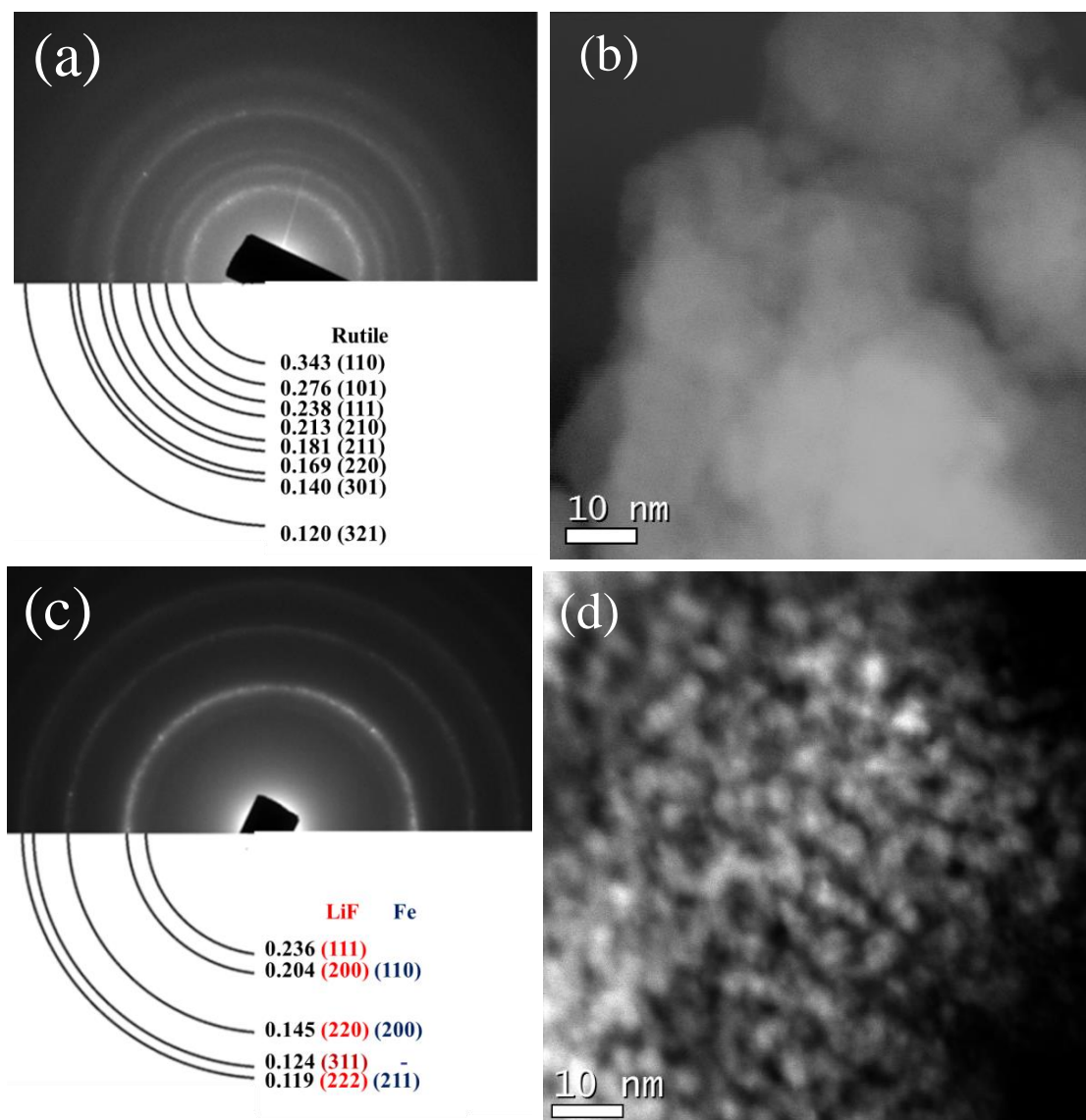


Figure 5-4 SAED pattern and ADF images of the delithiated sample (a,b) after 1 cycle, (c,d) after 20 cycles.

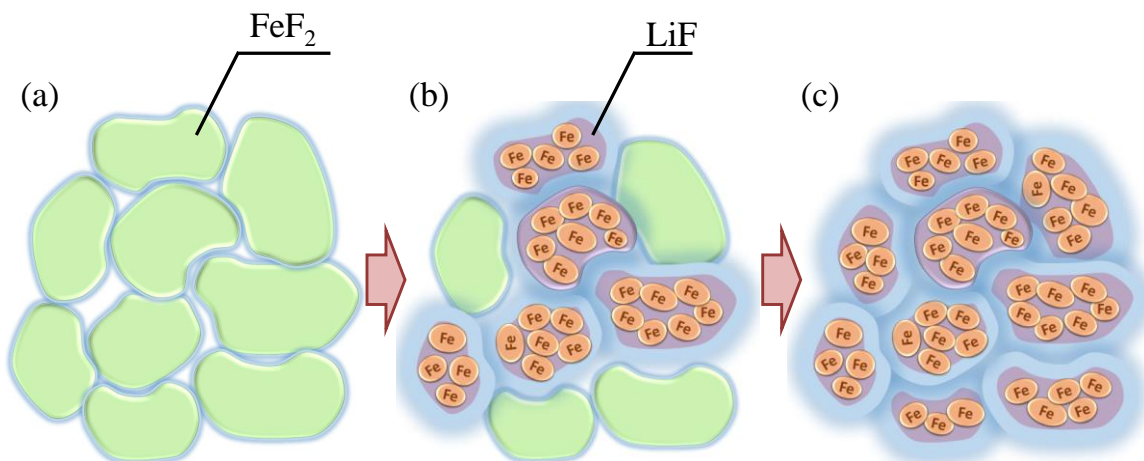


Figure 5-5 Schematic illustration showing the evolution of the fully charged  $\text{FeF}_2$  samples after (a) 1 cycle, (b) 10 cycles, (d) 20 cycles as seen using TEM. The surface SEI (blue) is represented surrounding each  $\text{FeF}_2$  particles.

To further characterize the chemical evolution with increasing cycle number, EELS spectra were acquired on both the lithiated and delithated samples, after 1, 2, 10 and 20 cycles in energy windows comprising the Fe-M and Li-K edges, and the O-K, F-K and Fe- $L_{2,3}$  edges. The EELS spectra measured on the lithiated samples consistently indicated the presence of metallic Fe and LiF. Upon cycling however, a gradual increase of the LiF-related peaks and of the total oxygen content is observed. Figure 5-6 shows the same EELS spectra measured on the delithated samples as a function of cycle number.

Here more drastic changes can be seen, with in particular the addition of a Li-K edge signal at the 10<sup>th</sup> and 20<sup>th</sup> cycle (indicated by the arrows), to the Fe-M edge in Figure 5-6(a). Figure 5-6(b), a gradual increase of the O-K edge signal is observed with increasing cycle number, and a fluorine post-peak (indicated by the arrows) attributed to LiF [31], is visible for the 10<sup>th</sup> and 20<sup>th</sup> cycles. The progressive increase of oxygen after 10 cycles, both visible in the active material region, in the lithiated and delithated states,

has been previously attributed to solvent decomposition. In particular, the cyclic molecule EC has been shown to decompose for high biases, leading to accumulation of  $\text{Li}_2\text{CO}_3$ . In parallel, it is clear that the  $\text{FeF}_2$  reversion is impeded with increasing cycle numbers, resulting in more  $\text{LiF}$  and  $\text{Fe}^0$ , which inhibit  $\text{Li}^+$  diffusion back into the anode up charging. Such a trend is schematically represented in Figure 5-5. Given the fact that the local chemistry of the active material does not seem profoundly altered (i.e.  $\text{FeF}_2$ ,  $\text{LiF}$  or  $\text{Fe}^0$  are still available), a surface passivation mechanism could most likely explain the loss of reversion ability.

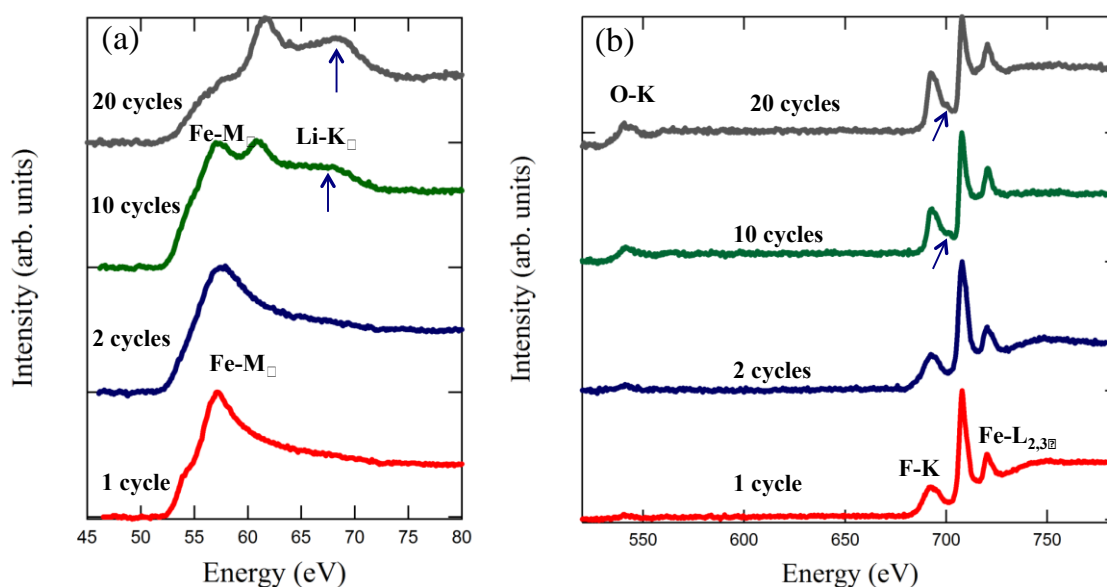


Figure 5-6 EELS spectra of the delithiated sample after various cycle number (a) Li K- and Fe M-edges, (b) O K-, F K-, and Fe L<sub>2,3</sub> edges.

(b) SEI imaging and characterization

Although TEM is a bulk sensitive technique and the SEI is expected only at the surface of the cathode material, it is possible to identify from ADF-STEM and EELS a

novel phase developing with increasing cycle number. Regions typically darker than the cathode material (attributed to the presence of low Z-materials) were often found at the edges of particles on ADF-STEM images, such as the one presented in Figure 5-7(a), measured on a lithiated sample after 20 cycles. Such outer-regions were more prominent and more numerous with increasing cycle number, both in lithiated and delithiated samples. Consequently, they are attributed to the developing SEI. Although the measured thickness was found inhomogeneous locally, it ranged between 15 nm to 100 nm.

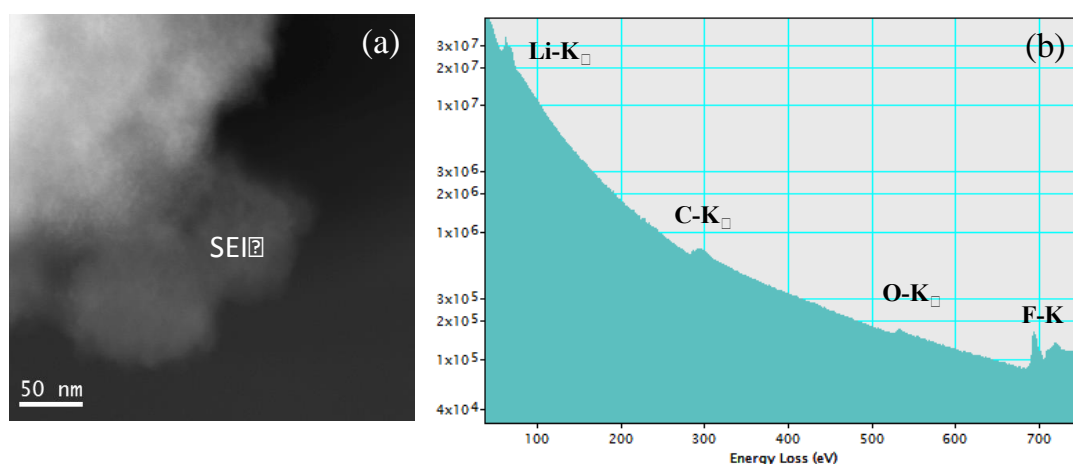


Figure 5-7 (a) ADF-STEM image of the lithiated FeF<sub>2</sub> after 20 cycles, (b) the corresponding spliced EELS spectrum.

Figure 5-7(b) shows the splice EELS spectrum measured on this region, comprising the Li-K, C-K, O-K and F-K edges. From this spectrum, a semi-quantitative atomic composition of the overlayer can be estimated to  $\text{Li}_{0.5}\text{C}_{0.1}\text{O}_{0.1}\text{F}_{0.3}$  by using ionization cross sections based on a Hatree-Slater model. It should be noted that little phosphorus (in the order of 1%) was visible in EELS in the same region. Higher resolution EELS spectra from this region display distinctively different fine structures

compared to the electrode material. Aided from earlier reports of possible compounds resulting from electrolyte decomposition or present in the system, these high resolution spectra are compared to chosen references materials in Figure 5-8. The comparison of the Li-K edges of  $\text{Li}_2\text{CO}_3$ , LiF and the SEI in Figure 5-8(a), indicates that Li in the SEI could be mainly in the form of LiF, and not in the form of  $\text{Li}_2\text{CO}_3$ , as is commonly reported. The comparison of the C-K and O-K edges EELS spectra shown Figure 5-8(b) and Figure 5-8(c), respectively, supports this attribution. Not surprisingly, the F-K edge EELS spectrum of the SEI shown in Figure 5-8(d) includes features associated with LiF as well [13, 31]. However, another peak is present around 710 eV that does not correspond to another F containing compound we could have expected, PVDF. Figure 5-9 is shown the result of the subtraction of the F-K edge LiF reference spectrum from the SEI spectrum. The resulting intensity could correspond to a small Fe- $\text{L}_{2,3}$  edge signature (located at 708 eV and 720.3 eV) with Fe either in the 2+ or 0 oxidation state. Given the absence of contrast in the ADF-STEM image of the SEI (Figure 5-7(a)), the presence of  $\text{Fe}^0$  nanoparticles is unlikely, leaving the possibility for iron to be diluted in the SEI and therefore most likely oxidized. Identification of the carbon and oxygen containing compounds resulting in the EELS spectra of Figure 5-8(b) and Figure 5-8(c) was not conclusive however.



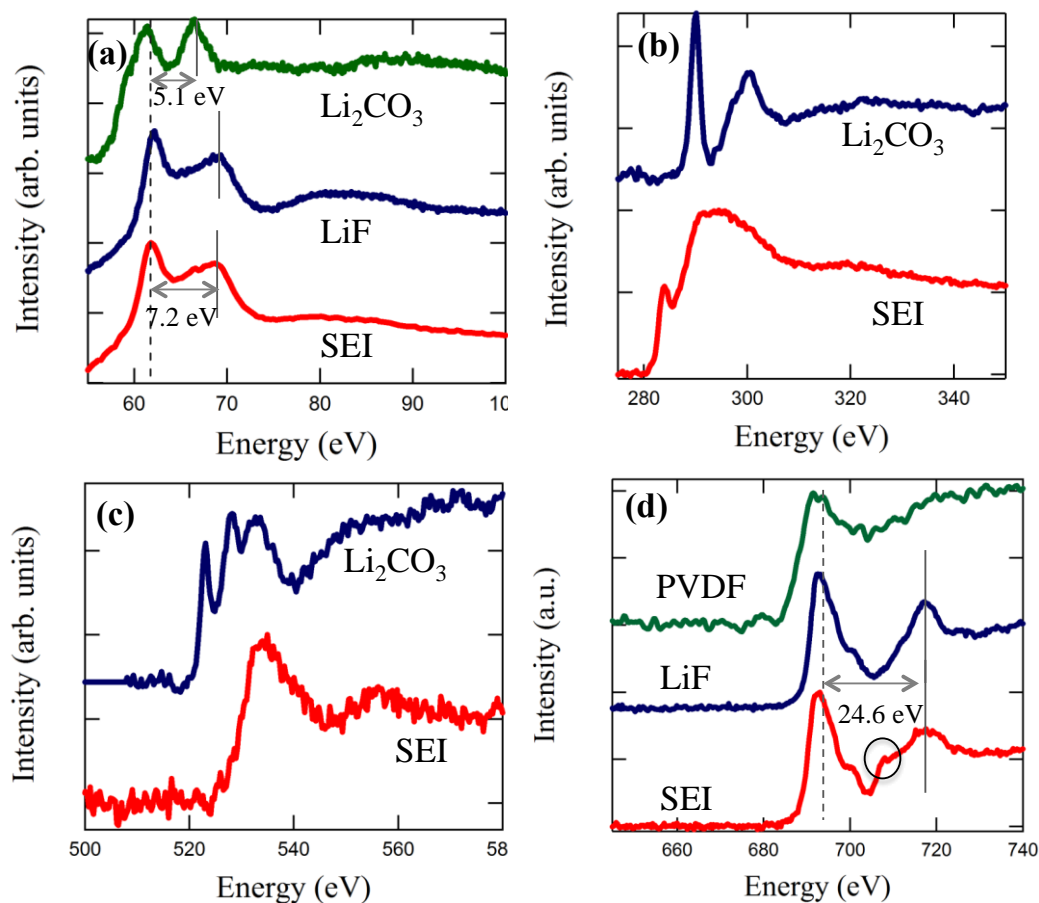


Figure 5-8 The comparison of the lithiated  $\text{FeF}_2$  after 20 cycles SEI layer to the reference compounds ( $\text{LiF}$ ,  $\text{Li}_2\text{CO}_3$ , and PVDF) (a) Li K-edge, (b) C K-edge, (c) O K-edge, (d) F K-edge.

A picture of the SEI can be established from the combined TEM results. The SEI is growing with increasing cycle number (although the local information given by TEM does not allow an evaluation of the thickness), and is mainly composed of LiF, organic compounds and embedded iron. As stated in the introduction, the presence of LiF is typically interpreted as: first a direct product of decomposition of  $\text{LiPF}_6$  and second an indirect product of  $\text{Li}_2\text{CO}_3$  decomposition in contact with HF. This latter argument supports the relative absence of  $\text{Li}_2\text{CO}_3$  in the SEI. In any case, little phosphorus

compounds were observed in TEM, indicating either the removal of all P-containing materials upon rinsing in DMC, the generation of volatile P-containing compounds, or another reaction path for LiF generation. The presence of iron embedded in the SEI is consistent with work done on other metal containing electrodes, indicating metal migration from the surface of the active material [15, 96, 101, 102]. A recent work on the lithiation/delithiation of  $\text{FeF}_2$  [56] indicates that LiF lattice parameters expand upon delithiation as a result of the substitution of  $\text{Li}^+$  ion into the LiF lattice by larger  $\text{Fe}^{2+}$  cations, leading to the formation of a new  $\text{Fe}_x\text{Li}_{2-x}\text{F}_2$  compound. This observation is compatible with our data, as the intensity of the additional Fe  $\text{L}_{2,3}$  peaks superimposed to the F-K edge of the SEI (Figure 5-9) increased with cycle number. Thus part of the active material is trapped into the SEI with increasing cycle number and could contribute to the capacity loss in such systems.

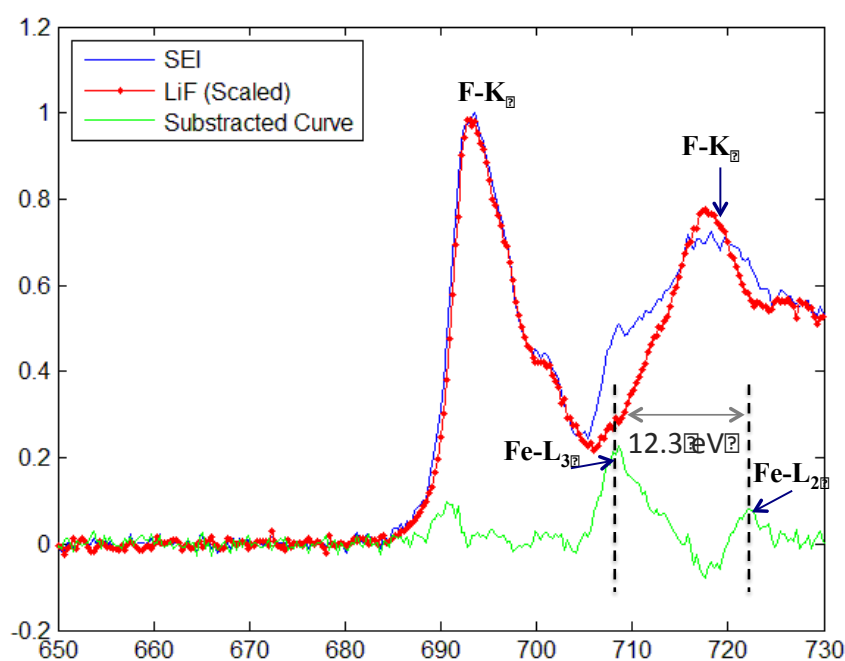


Figure 5-9 Subtracted EELS spectrum of SEI layer from LiF (SEI is from the same area in Figure 5-5). The subtracted spectrum shows the presence of Fe  $\text{L}_{2,3}$  edges.

Finally, although  $\text{Li}_2\text{CO}_3$  has been commonly reported in the literature for similar systems, here EELS spectroscopy does not indicate its presence. It has to be noted that destructing effects due to the high energy electron beam used in TEM cannot be excluded, in particular on organic films and possibly on carbonates. Moreover, the organic component of the SEI is not easily interpreted using TEM. XPS will be better suited to probe the chemical composition of the organic counterpart of the SEI film.

#### 5.4.4. XPS characterization

Figure 5-10 shows a series of XPS core level spectra of a delithiated  $\text{FeF}_2$  electrode after 1 cycle. The length appended to each spectrum corresponds to the estimated sputter depth at which the spectrum was acquired.

Figure 5-10(a) shows the Fe 2p core level at the surface and after sputtering to 1 nm and 10 nm. Before sputtering, a small Fe 2p signal is visible, suggesting most of the Fe in the sample is located in the sub-surface region and its signal is attenuated by the SEI layer. The most intense peaks in this broad spectrum are at about -712 eV and -725 eV, corresponding to the  $2p_{3/2}$  and  $2p_{1/2}$  components of  $\text{Fe}^{2+}$  respectively [103]. After sputtering 1 nm of material, the signature of  $\text{FeF}_2$  is more evident, and the intensity in the region of the Fe 2p core levels can be in part fitted with a  $\text{FeF}_2$  reference spectrum (red), leaving however some intensity around -720 eV. The latter is attributed to a plasmon loss peak from the F 1s core level, since this intensity is located in the Fe  $2p_{3/2}$  region and has no accompanying component in the  $2p_{1/2}$  region. After a high-current sputter of 10 nm,  $\text{Fe}^0$  peaks became visible at -708 eV and -720 eV due to the selective removal of fluorine. However, the relative intensity of the Fe 2p does not increase, suggesting that the  $\text{FeF}_2$  electrode is relatively homogenous below 1 nm, i.e. the SEI layer is 1 nm thick.

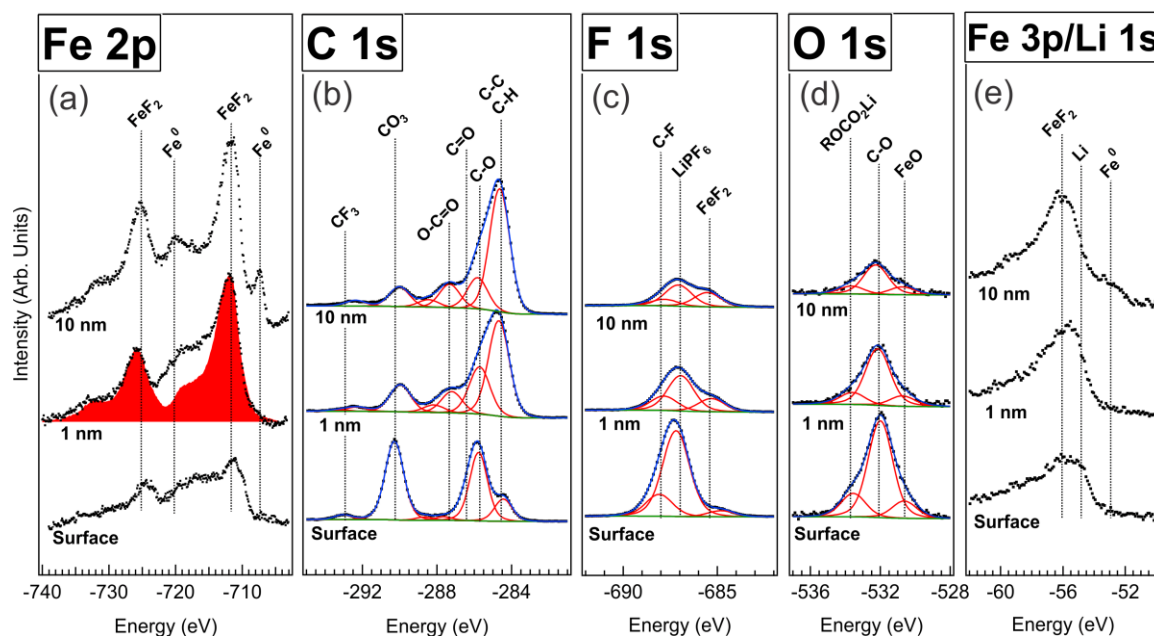


Figure 5-10 XPS spectra of a delithiated  $\text{FeF}_2$  electrode after 1 cycle at different sputter depths. The Fe 2p peak is fit very well by a single  $\text{FeF}_2$  component, indicating that the active cathode material has fully reconverted during delithiation. SEI composition is discussed in the text.

Figure 5-10(b), the C 1s core levels spectra indicate a rich chemistry, evolving with sputter depth. The surface spectrum can be decomposed into several components corresponding to different chemical bonds. The peak at -284.8 eV is attributed to C-C or C-H bonds from the PVDF binder, carbon black, and various hydrocarbons [104]. The peaks at -286.2 eV and -290.5 eV are attributed to C-O and  $\text{CO}_3$  bonds respectively, and are both likely from the EC:DMC electrolyte solvent. The ratio of C-O to  $\text{CO}_3$  in EC:DMC should be 2:1, so the remaining  $\text{CO}_3$  signal could be attributed to the formation of Li-alkyl carbonates ( $\text{ROCO}_2\text{Li}$ ), Li-alkoxides ( $\text{R-CH}_2\text{OLi}$ ), and/or  $\text{Li}_2\text{CO}_3$  [93-95, 105]. The small peak at -293 eV corresponds to  $\text{CF}_2$  bonds in PVDF as confirmed by XPS of PVDF powder. After sputtering, the C 1s intensity from EC:DMC is reduced,

again suggesting that the SEI is mainly confined to top 1 nm of the electrode. The carbon black component increases in intensity and remains constant after 10 nm of sputtering.

The surface F 1s core level spectrum, shown in Figure 5-10(c), has two major peaks at -687 eV and -688 eV, which are commonly attributed to C-F and LiPF<sub>6</sub> respectively (Dedryvere, Leroy et al. 2006). However, the P 2p peak (not shown) represents only 3% of the LiPF<sub>6</sub> signal from the F 1s peak, suggesting that this peak assignment is probably misattributed in most cases. The phosphorus intensity, although weak, was consistently observed in the XPS spectra of the non-sputtered surface for all [48]remaining on the surface was under an oxidized form such as Li<sub>x</sub>PO<sub>y</sub>F<sub>z</sub>. The small F 1s component at -685.5 eV corresponds to FeF<sub>2</sub> [48, 106]. After sputtering to 1 nm depth, the LiPF<sub>6</sub> and PVDF components are reduced in intensity, while the FeF<sub>2</sub> peak grows, in agreement with what was observed for the Fe 2p spectra. Sputtering to 10 nm further decreases the signal from the electrolyte, while the FeF<sub>2</sub> peak remains constant.

The surface O 1s spectrum in Figure 5-10(d) can be decomposed into three peaks. The small peak at -530.6 eV is characteristic of transition metal oxides, and probably corresponds to a small amount of FeO that formed at the surface of the electrode due to a reaction between Fe<sup>0</sup> or FeF<sub>2</sub> with the electrolyte [94]. The amount of FeO is estimated to be 10% of the iron content near the surface of the cathode based on the peak relative intensity. The main O 1s peak at -532 eV is attributed to C-O and CO<sub>3</sub> bonds, corresponding to EC:DMC and Li<sub>2</sub>CO<sub>3</sub>, while the smaller peak at -533.6 eV is attributed to ROCO<sub>2</sub>Li and/or R-CH<sub>2</sub>OLi [93-95, 105]. Each of these components decreases after sputtering, again confirming that the electrolyte and SEI are localized at the outermost 1-

2 nm of the electrode. Furthermore, the decreased FeO intensity after sputtering suggests that the oxidation of Fe/FeF<sub>2</sub> did not penetrate into the bulk of the electrode.

Figure 5-10(e) shows the Fe 3p and Li 1s core levels, whose overlapping intensities preclude definitive peak assignments. The surface Fe 3p/Li 1s spectrum is composed of a combination of Fe<sup>2+</sup> features at -56 eV and Li 1s intensity at about -55 eV. After sputtering, the Fe<sup>2+</sup> intensity increases, and a small Fe<sup>0</sup> feature appears at -53 eV, also in agreement with the Fe 2p spectrum of Figure 5-10(a). The XPS spectra for the delithiated electrode after 2 cycles were very similar, except for a slightly thicker SEI layer of about 5 nm.

Figure 5-11 shows the same set of XPS core levels for a delithiated electrode after 10 cycles, at which point the electrode has lost more than 50% of its initial capacity. The Fe 2p surface spectrum (Figure 5-11(a)) again contains only Fe<sup>2+</sup> components. However, three different components are necessary to fit the sputtered Fe 2p spectra: FeF<sub>2</sub> (shown in red), Fe<sup>0</sup> (gray), and a third component (yellow) derived from XPS spectra of lithiated FeF<sub>2</sub> thin films [106]. Comprising 10% of the Fe 2p intensity, this additional component has peaks at -709 eV and -722 eV and intense satellite features at -715.5 eV and -729.5 eV. Since this component has been observed in similar quantities in XPS studies of lithiated FeF<sub>2</sub> thin films without any sputtering, it is not believed to be caused by ion beam damage. Furthermore, this component was present in all Fe 2p spectra of cycled FeF<sub>2</sub> materials except for the delithiated 1-cycle sample. This component might possibly be attributed to Fe<sup>2+</sup> ions trapped in LiF in the form of Fe<sub>x</sub>Li<sub>2-x</sub>F<sub>2</sub>, as suggested by previous PDF measurements of FeF<sub>2</sub> electrodes [56]. Regardless of the origin of this component, it is clear that FeF<sub>2</sub> is not completely reformed upon delithiation of the

cathode at this stage, leading to some capacity losses. The Fe 2p intensity increases slightly after 10 nm of sputtering and remains constant thereafter, suggesting that the SEI is now 10 nm thick.

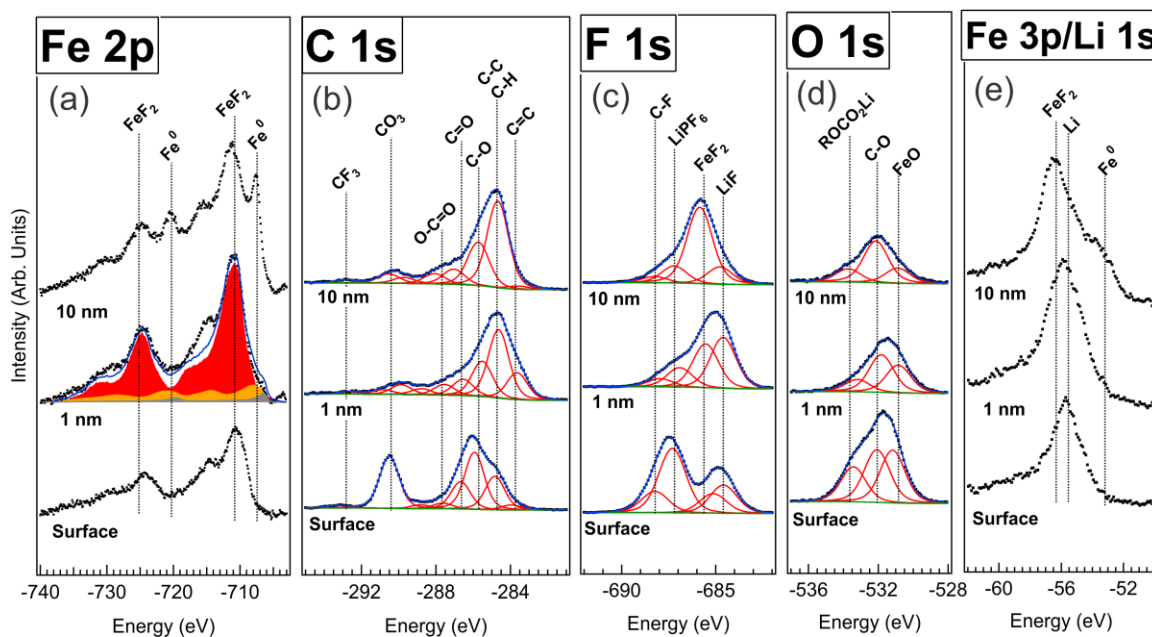


Figure 5-11 XPS sputter depth profile of a delithiated  $\text{FeF}_2$  electrode after 10 cycles. The lineshape of the Fe 2p peak is indicative of  $\text{FeF}_2$ ,  $\text{Fe}^0$ , and a third component (possibly  $\text{Li}_{1-x}\text{Fe}_x\text{F}$ ). The composition of the SEI is consistent with that of the 1 cycle sample, although this SEI is substantially thicker.

The C 1s spectra in Figure 5-11(b) are similar to those of the 1 cycle sample, except for the addition of a peak at -283.7 eV. This peak position is characteristic of C=C bonds and is likely from carbon black (Zhou, Wan et al. 2013). Otherwise, the similarity between the 1 cycle and 10 cycle spectra provide further evidence that the carbonaceous compounds in the SEI are constant from one cycle to the next. In Figure 5-11(c), the F 1s surface spectrum contains a new component at -684.6 eV, which is attributed to LiF. This agrees with the TEM-EELS data, which suggests that LiF is not completely removed

from the cathode upon delithiation and likely inhibits both electronic and ionic transport in the electrochemical cell. LiF is present throughout the 10 nm depth of the SEI.

The O 1s spectra in Figure 5-11(d) again have peaks characteristic of  $\text{ROCO}_2\text{Li}$ , EC:DMC, and FeO, although these peaks are more intense than those in Figure 5-10(d). The amount of FeO is 40% of the total iron content at the surface of the electrode after 10 cycles and 5% of the Fe content at 10 nm and below. Lastly, the Li 1s spectra in Figure 5-11(e) show a greater Li intensity than those of the 1-cycle sample, as evidenced by the large, narrow peak at -56 eV for the surface and 1 nm spectra. This provides further evidence of a thick LiF-rich SEI layer after 10 cycles. The trend of increasing SEI thickness and greater LiF and FeO content at the surface continues in the 20-cycle samples, although these spectra are not shown.

Figure 5-12 contains a similar set of XPS spectra for a lithiated sample after 10 cycles, in order to provide a direct comparison to the delithiated samples. The Fe 2p surface spectrum shown in Figure 5-12(a) has a much lower intensity than the same spectrum from the delithiated sample, suggesting that the SEI layer becomes thicker upon lithiation and decreases upon delithiation. This observation was found constant across the whole set of lithiated/delithiated samples. The relatively small  $\text{Fe}^0$  intensity (gray) with respect to the  $\text{FeF}_2$  signal, visible after sputtering the sample, is probably not representative of the real amount of metallic iron after lithiation, due to the sputter-induced formation of  $\text{FeF}_2$  discovered in this study. Additionally, the lineshape of the Fe 2p core levels was best decomposed by adding a component (orange) similar to the one of Figure 5-11(a). The Fe 2p core levels thus indicate at least three chemical environments for iron. Finally, the total Fe 2p intensity increases as a function of sputter



time until about 50 nm of material have been removed from the surface indicating a 50 nm overlayer thickness.

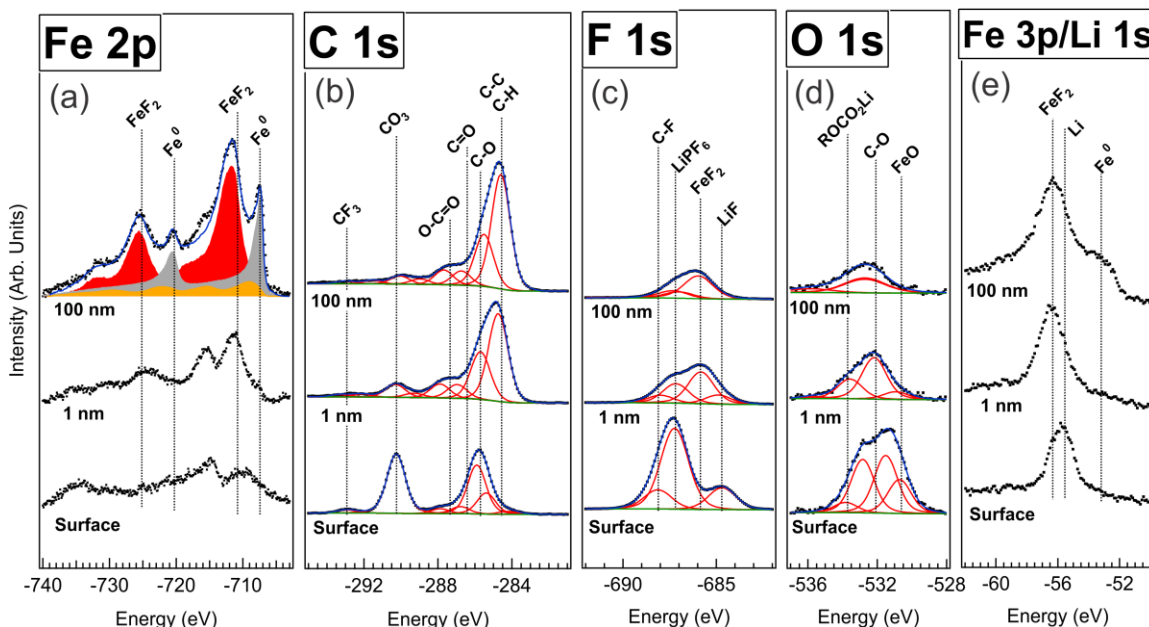


Figure 5-12 XPS sputter depth profile of a lithiated  $\text{FeF}_2$  electrode after 10 cycles.

The C 1s, F 1s, and O 1s spectra in Figure 5-12(b), Figure 5-12(c), and Figure 5-12(d) respectively, contain the same peaks as those of the delithiated samples. This suggests that the chemical composition of the SEI does not change during cycling, although the thickness increases and the relative amount of LiF increases as a function of cycle number. The F 1s surface spectrum does not contain an  $\text{FeF}_2$  component, suggesting that FeO is the only iron compound present at the surface of this electrode. After sputtering, the  $\text{FeF}_2$  peak become visible and the FeO peak in the O 1s spectrum decreases. Finally, as expected, the Li 1s spectra in Figure 5-12(e) show a much greater concentration of lithium in this lithiated sample than in the delithiated samples. Table 1

shows a summary of the XPS results including an estimated SEI thickness based on the intensity of the Fe 2p peak.

Table 5-1 Summary of XPS results for lithiated and delithiated samples: the SEI thickness as estimated by the amount of sputtering necessary to reach a stable Fe 2p intensity and percentage of the total F 1s signal attributed to LiF.

Number of Cycles	SEI Thickness (nm)		LiF at Surface (% of total F 1s Signal)	
	Lithiated	Delithiated	Lithiated	Delithiated
1	10	1	5%	0%
2	50	5	3%	0%
10	>50	20	18%	21%
20	>50	20	36%	13%

## 5.5. Conclusion

The SEI formation and the evolution of a conversion  $\text{FeF}_2/\text{C}$  cathode during cycling, has been investigated using a combination of bulk-sensitive techniques, TEM-EELS and surface sensitive-technique XPS and HIM.

TEM/EELS indicate that reconversion is strongly impeded with increasing cycle number, leaving mainly LiF and  $\text{Fe}^0$  after the 20<sup>th</sup> cycle, explaining the capacity fading observed during cycling.

HIM, TEM/EELS and XPS provide clear evidence of the growth of an SEI layer at the surface of the  $\text{FeF}_2/\text{C}$  material. The thickness of the SEI is greatly increased for discharged samples (from 10 to more than 50 nm) when compared to charged samples (from 1 to 20 nm). Several phases have been identified throughout the SEI layer:

1) An increasingly growing LiF phase thought to be caused by solvent and  $\text{LiPF}_6$  dissociation

- 2) Oxidized lithium salts  $\text{LiO}_x\text{P}_y\text{F}_z$  from  $\text{LiPF}_6$  degradation
- 3) Minor phases of  $\text{Li}_2\text{CO}_3$  or  $\text{ROCOOLi}$  due to solvent decomposition
- 4) An  $\text{FeO}$  phase at the outmost surface due to reaction with the oxygen containing solvent
- 5) An increasing number of  $\text{Fe}^{2+}$  cations possibly trapped in a  $\text{LiF}$  phase

Two main mechanisms have been identified leading to capacity loss. First, the growth of an insulating  $\text{LiF}$ -rich SEI layer can prevent  $\text{Li}^+$  ion diffusion to and from the active material  $\text{FeF}_2/\text{C}$ . Second, degradation of the active material upon cycling leads to trapped  $\text{Fe}^{2+}$  in  $\text{LiF}$  and  $\text{FeO}$  formation. Thus part of the active material cannot participate to the conversion reaction anymore.

Due to the complexity of the problem, additional experiments should be aimed at exploring the phase space of initial components in the system. For example, tests of several electrolytes have been started and proven that cyclic carbonates could contribute to SEI growth [12, 15, 91]. Little work has been devoted to the systematic study of lithium salts in a similar environment. Additionally, the contribution to the cell chemistry resulting from the binder is rarely addressed. Indeed, related work using  $\text{LiPF}_6$  in EC:DMC with  $\text{CoO}$  as a conversion material but without PVDF binder, does not indicate  $\text{LiF}$  but  $\text{Li}_2\text{CO}_3$  growth [95].

## 6. Future work

This work has shown that TEM is a powerful tool in characterizing Li-ion battery materials in order to gain structural, compositional and morphological information with nanoscale spatial resolution. As the conversion materials undergo considerable structural changes upon cycling, and transform to nanophases, they are so sensitive to moisture and air. Thus ex-situ experiments could have some drawbacks in characterizing of these materials. By using In-situ TEM we can track Li transport; also, study the structural and morphological changes of the nanoparticles in real time. In addition, in-situ study is very helpful for the characterization of SEI layer, since SEI layer composition is also so sensitive to moisture and can react with water and decompose into different compounds.

The growth of SEI layer as a result of electrolyte decomposition at the electrode/electrolyte interface after cycling is one of the major causes of capacity loss. EC/DMC which is used in this work, as the electrolyte solvent, is found to be reactive with the electrode upon cycling and led to the decomposition of electrolyte. Further work is required to study different type of electrolyte in order to hinder solvent decomposition and therefore improve the cycling performance..

The evolution of the SEI layer formation at the negative electrode/electrolyte interface upon cycling needs to be studied.

It was found that the formation of nanodomains Fe during lithiation catalysis the reduction of the electrolyte solvent. As the electrode/electrolyte interface has an important role in the cycling performance, we can develop a surface

surface coating technique such as ALD (“artificial SEI”) in order to impede solvent deposition and stabilize the electrode/electrolyte interface. Therefore, if the the surface of the electrode covered by a thin atomic layer can improve the cycling cycling performance.

## 7. Bibliography

1. Goodenough, J.B. and Y. Kim, *Challenges for Rechargeable Li Batteries*. Chem. Mater., 2010. **22**(3): p. 587-603.
2. Poizot, P., et al., *Nano-sized transition-metal oxides as negative-electrode materials for lithium-ion batteries*. Nature, 2000. **407**(6803): p. 496-9.
3. Tarascon, J.M. and M. Armand, *Issues and challenges facing rechargeable lithium batteries*. Nature (London, U. K.), 2001. **414**(6861): p. 359-367.
4. Whittingham, M.S., *Lithium Batteries and Cathode Materials*. Chem. Rev. (Washington, DC, U. S.), 2004. **104**(10): p. 4271-4301.
5. Amatucci, G.G. and N. Pereira, *Fluoride based electrode materials for advanced energy storage devices*. J. Fluorine Chem., 2007. **128**: p. 243-262.
6. Wang, F., et al., *Conversion Reaction Mechanisms in Lithium Ion Batteries: Study of the Binary Metal Fluoride Electrodes*. J. Am. Chem. Soc., 2011. **133**(46): p. 18828-18836.
7. Badway, F., et al., *Carbon Metal Fluoride Nanocomposites*. J. Electrochem. Soc., 2003. **150**(10): p. A1318-A1327.
8. Badway, F., et al., *Carbon-Metal Fluoride Nanocomposites. Structure and electrochemistry of  $\text{FeF}_3$ :C*. J. Electrochem. Soc., 2003. **150**(9): p. A1209-A1218.
9. Plitz, I., et al., *Structure and electrochemistry of carbon-metal fluoride nanocomposites fabricated by solid-state redox conversion reaction*. J. Electrochem. Soc., 2005. **152**(2): p. A307-A315.
10. Yamakawa, N., M. Jiang, and C.P. Grey, *Investigation of the Conversion Reaction Mechanisms for Binary Copper(II) Compounds by Solid-State NMR Spectroscopy and X-ray Diffraction*. Chem. Mater., 2009. **21**(14): p. 3162-3176.
11. Bervas, M., et al., *Bismuth fluoride nanocomposite as a positive electrode material for rechargeable lithium batteries*. Electrochem. Solid-State Lett., 2005. **8**(4): p. A179-A183.
12. Gmitter, A.J., et al., *Formation, dynamics, and implication of solid electrolyte interphase in high voltage reversible conversion fluoride nanocomposites*. J. Mater. Chem., 2010. **20**(20): p. 4149-4161.
13. Cosandey, F., et al., *Fe valence determination and Li elemental distribution in lithiated  $\text{FeO}_{0.7}\text{F}_{1.3}/\text{C}$  nanocomposite battery materials by electron energy loss spectroscopy (EELS)*. Micron, 2012. **43**(1): p. 22-29.
14. Pereira, N., et al., *Iron Oxyfluorides as High Capacity Cathode Materials for Lithium Batteries*. J. Electrochem. Soc., 2009. **156**(6): p. A407-A416.
15. Gmitter, A.J., et al., *Subsurface diffusion of oxide electrolyte decomposition products in metal fluoride nanocomposite electrodes*. Electrochim. Acta, 2013. **88**: p. 735-744.
16. Linden, D., *Hand book of Batteries*. 1995.
17. Nazri, G.A.P., G., *Lithium Batteries: Science and Technology*. 2004.
18. Cabana, J., et al., *Beyond Intercalation-Based Li-Ion Batteries: the State of the Art and Challenges of Electrode Materials Reacting Through Conversion Reactions*. Adv. Mater. (Weinheim, Ger.), 2010. **22**(35): p. E170-E192.

19. Badway, F., et al., *Structure and Electrochemistry of Copper Fluoride Nanocomposites Utilizing Mixed Conducting Matrices*. Chem. Mater., 2007. **19**(17): p. 4129-4141.
20. Wang, F., et al., *Chemical Distribution and Bonding of Lithium in Intercalated Graphite: Identification with Optimized Electron Energy Loss Spectroscopy*. ACS Nano, 2011. **5**(2): p. 1190-1197.
21. Yamakawa, N., et al., *Identifying the Local Structures Formed during Lithiation of the Conversion Material, Iron Fluoride, in a Li Ion Battery: A Solid-State NMR, X-ray Diffraction, and Pair Distribution Function Analysis Study*. Journal of the American Chemical Society, 2009. **131**(30): p. 10525-10536.
22. Labar, J.L., *Consistent indexing of a (set of) SAED pattern(s) with the ProcessDiffraction program*. Ultramicroscopy, 2005. **103**: p. 237-249.
23. Labar, J.L., et al., *Electron Diffraction Based Analysis of Phase Fractions and Texture in Nanocrystalline Thin Films, Part III: Application Examples*. Microsc. Microanal., 2012. **18**(2): p. 406-420.
24. Labar, J.L.A., M.; Barna, B. P.; Czigzny, Z.; Fogarassy, Z.; Horvath, Z. E.; Geszti, O.; Misjak, F.; Morgiel, J.; Radnoczi, G.; Safran, G.; Szekely L.; Szuts, T., *Microscopy and Microanalysis*, 2012. **18**: p. 406-420.
25. Budd, P.M., *Light-Element Analysis in the Transmission Electron Microscope: WEDX and EELS*. Royal Microscopy Society Handbooks, 1988.
26. Egerton, R.F. and Editor, *Electron Energy-Loss Spectroscopy in the Electron Microscope, Second Edition*. 1996: Plenum. 480 pp., (approx.).
27. Tatsumi, K. and S. Muto, *Local electronic structure analysis by site-selective ELNES using electron channeling and first-principles calculations*. J. Phys.: Condens. Matter, 2009. **21**(10): p. 104213/1-104213/14.
28. Williams, D.B.C.B., *Transmission Electron Microscopy*. Second ed. Vol. 1. 2009: Springer. 65-69.
29. Egerton, R.F., *Electron energy-loss spectroscopy in the TEM*. Rep. Prog. Phys., 2009. **72**(1): p. 016502/1-016502/25.
30. Riedl, T., T. Gemming, and K. Wetzig, *Extraction of EELS white-line intensities of manganese compounds: Methods, accuracy, and valence sensitivity*. Ultramicroscopy, 2006. **106**(4-5): p. 284-291.
31. Sina, M., et al., *Structural phase transformation and Fe valence evolution in  $\text{FeO}_x\text{F}_{2-x}/\text{C}$  nanocomposite electrodes during lithiation and de-lithiation processes*. J. Mater. Chem. A, 2013. **1**(38): p. 11629-11640.
32. Ellis, B.L., K.T. Lee, and L.F. Nazar, *Positive Electrode Materials for Li-Ion and Li Batteries*. Chem. Mater., 2010. **22**(3): p. 691-714.
33. Maier, H.L.G.R.J., *Reversible formation and decomposition of LiF clusters using transition metal fluorides as precursors and their application in rechargeable Li batteries*. Advanced Materials. **9**: p. 736-739.
34. Makimura, Y., A. Rougier, and J.-M. Tarascon, *Pulsed laser deposited iron fluoride thin films for lithium-ion batteries*. Appl. Surf. Sci., 2006. **252**(13): p. 4587-4592.

35. Cosandey, F., et al., *EELS spectroscopy of iron fluorides and FeF<sub>x</sub>/C nanocomposite electrodes used in Li-ion batteries*. Microsc. Microanal., 2007. **13**(2): p. 87-95.
36. Li, L., F. Meng, and S. Jin, *High-Capacity Lithium-Ion Battery Conversion Cathodes Based on Iron Fluoride Nanowires and Insights into the Conversion Mechanism*. Nano Lett., 2012. **12**(11): p. 6030-6037.
37. Li, T., et al., *Reversible Three-Electron Redox Behaviors of FeF<sub>3</sub> Nanocrystals as High-Capacity Cathode-Active Materials for Li-Ion Batteries*. J. Phys. Chem. C, 2010. **114**(7): p. 3190-3195.
38. Prakash, R., et al., *A ferrocene-based carbon-iron lithium fluoride nanocomposite as a stable electrode material in lithium batteries*. J. Mater. Chem., 2010. **20**(10): p. 1871-1876.
39. Cui, Y.-H., et al., *The investigation on electrochemical reaction mechanism of CuF<sub>2</sub> thin film with lithium*. Electrochim. Acta, 2010. **56**(5): p. 2328-2335.
40. Doe, R.E., et al., *First-Principles Investigation of the Li-Fe-F Phase Diagram and Equilibrium and Nonequilibrium Conversion Reactions of Iron Fluorides with Lithium*. Chem. Mater., 2008. **20**(16): p. 5274-5283.
41. Wiaderek, K.M., et al., *Comprehensive Insights into the Structural and Chemical Changes in Mixed-Anion FeOF Electrodes by Using Operando PDF and NMR Spectroscopy*. J. Am. Chem. Soc., 2013. **135**(10): p. 4070-4078.
42. Chevrier, V.L., et al., *First-principles study of iron oxyfluorides and lithiation of FeOF*. Phys. Rev. B: Condens. Matter Mater. Phys., 2013. **87**: p. 094118/1-094118/9.
43. Gozdz, A.S., et al., *Polymeric electrolytic cell separator membrane*. 1995, Bell Communications Research, Inc., USA . p. 11 pp. Cont.-in-part of U.S. 5,296,318.
44. Stadelmann, P.,  
["http://cimewww.epfl.ch/people/stadelmann/jemswebsite/jems.html"](http://cimewww.epfl.ch/people/stadelmann/jemswebsite/jems.html).
45. B, R., <http://cars9.uchicago.edu/ifeffit/BruceRavel/Horae>.
46. Brink, F.J., R.L. Withers, and J.G. Thompson, *An Electron Diffraction and Crystal Chemical Investigation of Oxygen/Fluorine Ordering in Rutile-Type Iron Oxyfluoride, FeOF*. J. Solid State Chem., 2000. **155**(2): p. 359-365.
47. Ma, Y.G., S. H. , *Atomistic insights into the conversion reaction in iron fluoride: A dynamically adaptive force field approach*. J. Am. Chem. Soc., 2012. **134**: p. 8205-8211.
48. Rangan, S., et al., *Conversion Reaction of FeF<sub>2</sub> Thin Films upon Exposure to Atomic Lithium*. J. Phys. Chem. C, 2012. **116**(19): p. 10498-10503.
49. Chen, G.S., C.B. Boothroyd, and C.J. Humphreys, *Electron-beam induced crystallization transition in self-developing amorphous AlF<sub>3</sub> resists*. Appl. Phys. Lett., 1996. **69**: p. 170-172.
50. Saifullah, M.S.M., et al., *Electron energy loss spectroscopy studies of the amorphous to crystalline transition in FeF<sub>3</sub>*. J. Appl. Phys., 1999. **86**: p. 2499-2504.
51. Colliex, C., T. Manoubi, and C. Ortiz, *Electron-energy-loss-spectroscopy near-edge fine structures in the iron-oxygen system*. Phys. Rev. B: Condens. Matter, 1991. **44**(20): p. 11402-11.



52. van Aken, P.A., B. Liebscher, and V.J. Styrskja, *Quantitative determination of iron oxidation states in minerals using Fe L<sub>2,3</sub>-edge electron energy-loss near-edge structure spectroscopy*. Phys. Chem. Miner., 1998. **25**(5): p. 323-327.
53. Graetz, J., et al., *An Electron Energy-Loss Spectrometry Study of Charge Compensation in LiNi<sub>0.8</sub>Co<sub>0.2</sub>O<sub>2</sub>*. J. Phys. Chem. B, 2003. **107**(13): p. 2887-2891.
54. Nakai, S., et al., *Core-exciton absorption in the fluorine K absorption spectra of 3d transition-metal fluorides*. Phys. Rev. B: Condens. Matter, 1988. **37**(18): p. 10895-7.
55. Mitome, M., et al., *Transmission electron microscopy and electron diffraction study of the short-range ordering structure of  $\alpha$ -LiFeO<sub>2</sub>*. Acta Crystallogr., Sect. B: Struct. Sci., 2004. **B60**(6): p. 698-704.
56. Ko, J.K., et al., *Transport, Phase Reactions, and Hysteresis of Iron Fluoride and Oxyfluoride Conversion Electrode Materials for Lithium Batteries*. ACS Appl. Mater. Interfaces, 2014: p. Ahead of Print.
57. Egerton, R.F., P. Li, and M. Malac, *Radiation damage in the TEM and SEM*. Micron, 2004. **35**: p. 399-409.
58. Libera, M., *Local amorphous thin-film crystallization induced by focused electron-beam irradiation*. Appl. Phys. Lett., 1996. **68**: p. 331-3.
59. Nagase, T. and Y. Umakoshi, *Electron irradiation induced crystallization of the amorphous phase in Zr-Cu based metallic glasses with various thermal stability*. Mater. Trans., 2004. **45**: p. 13-23.
60. Fujita, J., et al., *Sub-10 nm lithography and development properties of inorganic resist by scanning electron beams*. J. Vac. Sci. Technol., B, 1995. **13**: p. 2757-61.
61. Watanabe, H., et al., *Self-developing properties of an inorganic electron beam resist and nanometer-scale patterning using a scanning electron beam*. Jpn. J. Appl. Phys., Part 1, 1995. **34**: p. 6950-5.
62. Langheinrich, W., B. Spangenberg, and H. Beneking, *Nanostructure fabrication using lithium fluoride films as an electron beam resist*. J. Vac. Sci. Technol., B, 1992. **10**: p. 2868-72.
63. Kratschmer, E. and M. Isaacson, *Progress in self-developing metal fluoride resists*. J. Vac. Sci. Technol., B, 1987. **5**: p. 369-73.
64. Liu, X.J., et al., *Atomistic mechanism for nanocrystallization of metallic glasses*. Acta Mater., 2008. **56**: p. 2760-2769.
65. Nino, A., T. Nagase, and Y. Umakoshi, *Electron irradiation induced crystallization and amorphization in Fe<sub>77</sub>Nd<sub>4.5</sub>B<sub>18.5</sub> metallic glass*. Mater. Sci. Eng., A, 2007. **A449-A451**: p. 1115-1118.
66. Qin, W., J.A. Szpunar, and Y. Umakoshi, *Electron or ion irradiation-induced phase-change mechanism between amorphous and crystalline state*. Acta Mater., 2011. **59**: p. 2221-2228.
67. Lu, K., *Nanocrystalline metals crystallized from amorphous solids. Nanocrystallization, structure, and properties*. Mater. Sci. Eng., R, 1996. **R16**: p. 161-221 pp.
68. Motta, A.T., *Amorphization of intermetallic compounds under irradiation - A review*. J. Nucl. Mater., 1997. **244**: p. 227-250.

69. Nagase, T., T. Hosokawa, and Y. Umakoshi, *Electron irradiation-induced phase transition of an amorphous phase and face-centered cubic solid solutions in Zr<sub>66.7</sub>Pd<sub>33.3</sub> metallic glass*. Metall. Mater. Trans. A, 2007. **38A**: p. 223-235.
70. Nagase, T. and Y. Umakoshi, *Effect of irradiation temperature on the electron irradiation induced nanocrystallization behavior in Fe<sub>88.0</sub>Zr<sub>9.0</sub>B<sub>3.0</sub> amorphous alloy*. Mater. Sci. Eng., A, 2003. **A347**: p. 136-144.
71. Nagase, T. and Y. Umakoshi, *Electron irradiation induced crystallization behavior in Zr<sub>66.7</sub>Cu<sub>33.3</sub> and Zr<sub>65.0</sub>Al<sub>7.5</sub>Cu<sub>27.5</sub> amorphous alloys*. Mater. Sci. Eng., A, 2003. **A352**: p. 251-260.
72. Roddatis, V.V., et al., *Temperature- and electron-beam-induced crystallization of zirconia thin films deposited from an aqueous medium: a transmission electron microscopy study*. Philosophical Magazine a-Physics of Condensed Matter Structure Defects and Mechanical Properties, 2002. **82**(15): p. 2825-2839.
73. Ning, Y. and C. Li, *STRUCTURAL INHOMOGENEITY AND CRYSTALLIZATION BEHAVIOR OF AEROSOL-REACTED MGAL<sub>2</sub>O<sub>4</sub> POWDERS*. Materials Letters, 1992. **15**(1-2): p. 84-88.
74. Nagase, T., et al., *MeV electron irradiation induced crystallization in metallic glasses: Atomic structure, crystallization mechanism and stability of an amorphous phase under the irradiation*. J. Non-Cryst. Solids, 2012. **358**: p. 502-518.
75. Vijayakumar, M., et al., *Effect of Chemical Lithium Insertion into Rutile TiO<sub>2</sub> Nanorods*. J. Phys. Chem. C, 2009. **113**: p. 14567-14574.
76. Kim, H.-M., M.-H. Lee, and K.-B. Kim, *Theoretical and experimental study of nanopore drilling by a focused electron beam in transmission electron microscopy*. Nanotechnology, 2011. **22**(27).
77. Kinoshita, S.J.Z.a.C., *Defect production in ceramics*. Journal of Nuclear Materials Letters, 1997. **251**: p. 200.
78. Yu, N., K.E. Sickafus, and M. Nastasi, *Electron irradiation induced crystallization of amorphous MgAl<sub>2</sub>O<sub>4</sub>*. Mater. Chem. Phys., 1996. **46**: p. 161-165.
79. Roldan Cuenya, B., et al., *Observation of the fcc.-to-bcc. Bain transformation in epitaxial Fe ultrathin films on Cu<sub>3</sub>Au(001)*. Surf. Sci., 2001. **493**(1-3): p. 338-360.
80. Kim, S.-W., et al., *Fabrication of FeF<sub>3</sub> Nanoflowers on CNT Branches and Their Application to High Power Lithium Rechargeable Batteries*. Adv. Mater. (Weinheim, Ger.), 2010. **22**(46): p. 5260-5264.
81. Liu, L., et al., *A comparison among FeF<sub>3</sub>·3H<sub>2</sub>O, FeF<sub>3</sub>·0.33H<sub>2</sub>O and FeF<sub>3</sub> cathode materials for lithium ion batteries: Structural, electrochemical, and mechanism studies*. J. Power Sources, 2013. **238**: p. 501-515.
82. Arai, H., et al., *Cathode performance and voltage estimation of metal trihalides*. J. Power Sources, 1997. **68**(2): p. 716-719.
83. Badway, F., et al., *Reversible conversion metal fluoride nanocomposites: new options for next generation high energy lithium batteries*. Proc. Power Sources Conf., 2006. **42nd**: p. 277-280.

84. Liu, P., et al., *Thermodynamics and Kinetics of the Li/FeF<sub>3</sub> Reaction by Electrochemical Analysis*. J. Phys. Chem. C, 2012. **116**(10): p. 6467-6473.
85. Myung, S.-T., et al., *Iron trifluoride synthesized via evaporation method and its application to rechargeable lithium batteries*. J. Power Sources, 2013. **223**: p. 1-8.
86. Zhang, W., et al., *In Situ Electrochemical XAFS Studies on an Iron Fluoride High-Capacity Cathode Material for Rechargeable Lithium Batteries*. J. Phys. Chem. C, 2013. **117**(22): p. 11498-11505.
87. Liao, P., J. Li, and J.R. Dahn, *Lithium Intercalation in LiFe<sub>2</sub>F<sub>6</sub> and LiMgFeF<sub>6</sub> Disordered Trirutile-Type Phases*. J. Electrochem. Soc., 2010. **157**(3): p. A355-A361.
88. Amatucci, G.G., et al., *Formation of lithium fluoride/metal nanocomposites for energy storage through solid state reduction of metal fluorides*. J. Fluorine Chem., 2011. **132**(12): p. 1086-1094.
89. Cherkashinin, G., et al., *The stability of the SEI layer, surface composition and the oxidation state of transition metals at the electrolyte-cathode interface impacted by the electrochemical cycling: X-ray photoelectron spectroscopy investigation*. Phys. Chem. Chem. Phys., 2012. **14**(35): p. 12321-12331.
90. Cuisinier, M., et al., *Quantitative MAS NMR characterization of the LiMn<sub>1/2</sub>Ni<sub>1/2</sub>O<sub>2</sub> electrode/electrolyte interphase*. Solid State Nucl. Magn. Reson., 2012. **42**: p. 51-61.
91. Gmitter, A.J., J. Gural, and G.G. Amatucci, *Electrolyte development for improved cycling performance of bismuth fluoride nanocomposite positive electrodes*. J. Power Sources, 2012. **217**: p. 21-28.
92. Marino, C., et al., *Study of the Electrode/Electrolyte Interface on Cycling of a Conversion Type Electrode Material in Li Batteries*. J. Phys. Chem. C, 2013. **117**(38): p. 19302-19313.
93. Swiatowska-Mrowiecka, J., et al., *XPS study of Li ion intercalation in V<sub>2</sub>O<sub>5</sub> thin films prepared by thermal oxidation of vanadium metal*. Electrochim. Acta, 2007. **52**(18): p. 5644-5653.
94. Tian, B., et al., *Combined Surface and Electrochemical Study of the Lithiation/De-lithiation Mechanism of the Iron Oxide Thin-Film Anode for Lithium-Ion Batteries*. J. Phys. Chem. C, 2013. **117**(42): p. 21651-21661.
95. Dedryvere, R., et al., *Contribution of X-ray Photoelectron Spectroscopy to the Study of the Electrochemical Reactivity of CoO toward Lithium*. Chem. Mater., 2004. **16**(6): p. 1056-1061.
96. Balasubramanian, M., et al., *Formation of SEI on cycled lithium-ion battery cathodes. Soft x-ray absorption study*. Electrochem. Solid-State Lett., 2002. **5**(1): p. A22-A25.
97. Bryngelsson, H., et al., *How dynamic is the SEI?* J. Power Sources, 2007. **174**(2): p. 970-975.
98. Dedryvere, R., et al., *XPS identification of the organic and inorganic components of the electrode/electrolyte interface formed on a metallic cathode*. J. Electrochem. Soc., 2005. **152**(4): p. A689-A696.

99. Plakhotnyk, A.V., L. Ernst, and R. Schmutzler, *Hydrolysis in the system  $\text{LiPF}_6$ —propylene carbonate—dimethyl carbonate— $\text{H}_2\text{O}$* . Journal of Fluorine Chemistry, 2005. **126**(1): p. 27-31.
100. Aurbach, D., et al., *Recent studies on the correlation between surface chemistry, morphology, three-dimensional structures and performance of Li and Li-C intercalation anodes in several important electrolyte systems*. J. Power Sources, 1997. **68**(1): p. 91-98.
101. Amine, K., et al., *Mechanism of capacity fade of MCMB- $\text{Li}_{1.1}[\text{Ni}_{1/3}\text{Mn}_{1/3}\text{Co}_{1/3}]\text{O}_2$  cell at elevated temperature and additives to improve its cycle life*. J. Mater. Chem., 2011. **21**(44): p. 17754-17759.
102. Song, B., et al., *Structural evolution and the capacity fade mechanism upon long-term cycling in Li-rich cathode material*. Phys. Chem. Chem. Phys., 2012. **14**(37): p. 12875-12883.
103. Grosvenor, A.P., et al., *Investigation of multiplet splitting of Fe 2p XPS spectra and bonding in iron compounds*. Surf. Interface Anal., 2004. **36**(12): p. 1564-1574.
104. Dedryvere, R., et al., *XPS Valence Characterization of Lithium Salts as a Tool to Study Electrode/Electrolyte Interfaces of Li-Ion Batteries*. J. Phys. Chem. B, 2006. **110**(26): p. 12986-12992.
105. Swiatowska-Mrowiecka, J., et al., *Li-ion intercalation in thermal oxide thin films of  $\text{MoO}_3$  as studied by XPS, RBS, and NRA*. J. Phys. Chem. C, 2008. **112**(29): p. 11050-11058.
106. Thorpe, R., et al., *Conversion Reaction of CoO Polycrystalline Thin Films Exposed to Atomic Lithium*. J. Phys. Chem. C, 2013. **117**(28): p. 14518-14525.